HOKKAIDO UNIVERSITY

Title	Study on External Field-induced Photophysical Properties of Chiral Lanthanide Complexes
Author(s)	和田, 智志
Degree Grantor	北海道大学
Degree Name	博士(工学)
Dissertation Number	甲第13693号
Issue Date	2019-03-25
DOI	https://doi.org/10.14943/doctoral.k13693
Doc URL	https://hdl.handle.net/2115/91464
Type	doctoral thesis
File Information	Satoshi_Wada.pdf

Study on External Field-induced Photophysical Properties of Chiral Lanthanide Complexes

キラル希土類錯体の外場に誘起された光物性に関する研究

Satoshi Wada

Graduate School of Chemical Sciences and Engineering

Hokkaido University

Chapter 5

Summary

5.1   Summary and outlook

Chapter 1

General introduction

1.1   Lanthanides

Lanthanides (Ln) have attracted attention for their unique chemical and physical properties. They have been applied for various functional materials in the field of optics, magneto-optics, electronics, and magnetics.[1–7]

Lanthanide series consist of 15 elements from La (atomic number: 57) to Lu (atomic number: 71) in the periodic table (**Figure 1-1**). The 4f electrons in lanthanides generate unique physical properties compared with those of organic molecules or transition metal. Lanthanides are commonly stable in trivalent state. The lanthanide electronic configurations in atomic and trivalent ionic (Ln(III)) states are shown in **Table 1-1**. The electronic [Xe]4f^n configurations (n =0 - 14) generate a rich variety of electronic levels, the number (N) of which is given by Equation (1.1),

$$N = \frac{14!}{n! \cdot (14 - n)!}.$$ (1.1)

For example, the number of electronic level for Eu(III) ion is 3,003 (n = 6). The energies

Figure 1-1. Lanthanides in the periodic table.

Table 1-1. Electronic configurations of lanthanides.

Atomic number	Element	Configuration	
		Atom	Trivalent ion
57	La	$[Xe]5d^16s^2$	$[Xe]$
58	Ce	$[Xe]4f^15d^16s^2$	$[Xe]4f^1$
59	Pr	$[Xe]4f^36s^2$	$[Xe]4f^2$
60	Nd	$[Xe]4f^46s^2$	$[Xe]4f^3$
61	Pm	$[Xe]4f^56s^2$	$[Xe]4f^4$
62	Sm	$[Xe]4f^66s^2$	$[Xe]4f^5$
63	Eu	$[Xe]4f^76s^2$	$[Xe]4f^6$
64	Gd	$[Xe]4f^75d^16s^2$	$[Xe]4f^7$
65	Tb	$[Xe]4f^96s^2$	$[Xe]4f^8$
66	Dy	$[Xe]4f^{10}6s^2$	$[Xe]4f^9$
67	Ho	$[Xe]4f^{11}6s^2$	$[Xe]4f^{10}$
68	Er	$[Xe]4f^{12}6s^2$	$[Xe]4f^{11}$
69	Tm	$[Xe]4f^{13}6s^2$	$[Xe]4f^{12}$
70	Yb	$[Xe]4f^{14}6s^2$	$[Xe]4f^{13}$
71	Lu	$[Xe]4f^{14}5d^16s^2$	$[Xe]4f^{14}$

of these levels are well defined due to the shielding of the 4f orbitals by the outer 5s and 5p electrons. The energy levels of Ln(III) ions are shown in the Dieke diagram (**Figure 1-2**),[8,9] which are represented by Russell-Saunders term symbols: $^{2S+1}L_J$. The numbers of S, L, and J denote total spin quantum number, total orbital quantum number, and total

angular quantum number, respectively. The letter symbol L = S, P, D, F, G, H, I, … stands for L = 0, 1, 2, 3, 4, 5, 6, …, for example.

Some of the lanthanides also form stable compounds in divalent or tetravalent oxidation states.[3] Eu and Yb are likely to take a divalent state by forming the same electronic configurations as Gd and Lu, respectively. Ce and Tb oxidize to a tetravalent state by taking the electronic configurations of La and Gd, respectively.

Figure 1-2. Dieke diagram related to energy levels of Ln(III) ions reprinted from ref [9].

4

1.2   Photophysical properties of lanthanide compounds

1.2.1   Lanthanide compounds with organic molecules

An incorporation of lanthanide with designed organic molecules is a useful method to control physical properties of Ln(III) ions.[2,10–12] Lanthanide compounds with organic molecules include mono- or poly-nuclear Ln(III) complexes,[13,14] Ln(III) coordination polymers,[15] and Ln(III) clusters,[16] for example (**Figure 1-3**). Ln(III) complexes are composed of one Ln(III) ion or several Ln(III) ions coordinated with organic ligands in a single molecule. The coordination number in one Ln(III) ion depends on the ionic radii rather than inner 4f electrons of Ln(III) ions. Since the effective ionic radii of Ln(III) ions are relatively large compared with those of other metal ions (**Table 1-2**),[17] the coordination number of Ln(III) ions is usually more than six and can vary according to the steric hindrance of organic ligands. Typical Ln(III) complex forms an eight- (or nine-) coordinated structure. Organic ligands possess electronegative group such as O atoms (e.g. β-diketonate, carboxylate, and phosphine oxide) and/or N atoms (e.g. amine, imine, and pyridine). Ln(III) coordination polymers are polynuclear complexes with polymer structure.[11] They are achieved by bridging ligands between Ln(III) ions. The polymer structure form assembled 1D chains, 2D sheets, and 3D

Table 1-2. Ionic radii of eight-coordinate Ln(III) ions.[17]

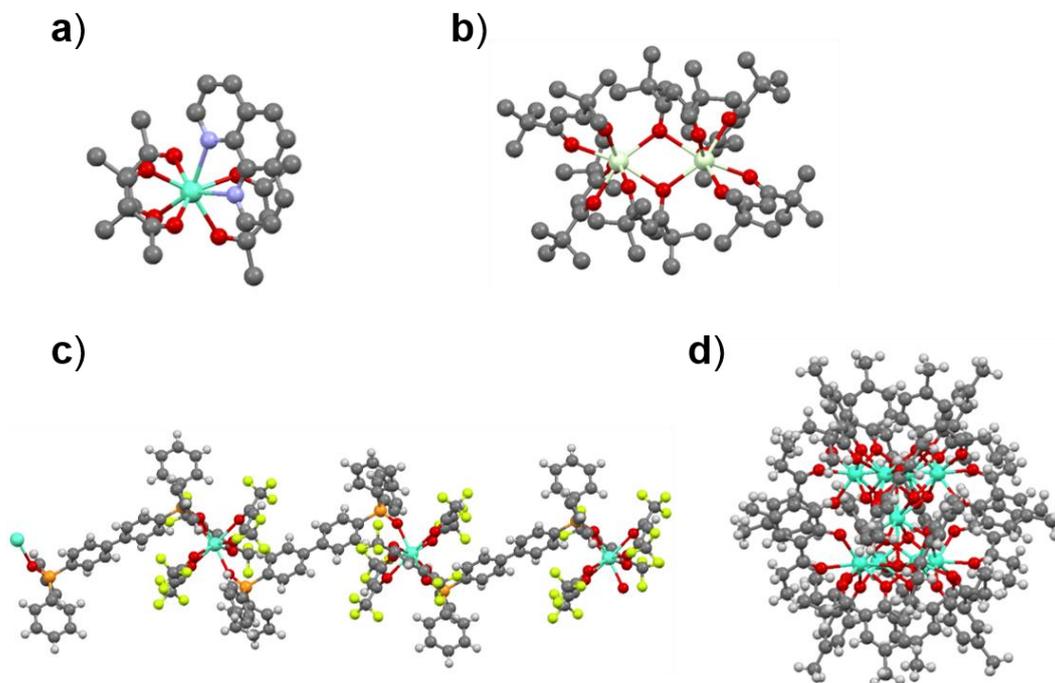|	La	Ce	Pr	Nd	Pm	Sm	Eu	Gd	Tb	Dy	Ho	Er	Tm	Yb	Lu
Ionic radius [pm]	116	114	113	111	109	108	107	105	104	103	102	100	99	99	98

Figure 1-3. Examples of (**a**) mononuclear Ln(III) complex,[13] (**b**) polynuclear Ln(III) complex,[14] (**c**) Ln(III) coordination polymer,[15] and (**d**) Ln(III) cluster.[16]

networks depending on the ligands.[12] Ln(III) clusters are polynuclear complexes with inorganic-like Ln(III) rich core coordinated by multiple ligands.[12,16,18,19] The Ln(III) rich core is often bridged by μ-OH ions. They are often made by controlling the hydrolysis of Ln(III) salts in the presence of supporting ligands.

Since the inner 4f orbitals have little contribution to chemical bonding with organic ligands, the energies of Ln(III) ions are not directly affected by the surrounding ligands. Nevertheless, the physical properties of Ln(III) ions are affected indirectly by surrounding ligands around Ln(III) ions or other external environments such as magnetic field. The following subsections mainly focus on photophysical properties in the photo-luminescence and photo-absorption based on 4f electrons of Ln(III) complexes.

1.2.2　Luminescence of lanthanide compounds

Ln(III) complexes exhibit characteristic luminescence properties deriving from the 4f electrons. They have attracted attention for molecular probes for biomedical imaging, electroluminescent devices, telecommunications, and security inks.[20,21] Since no 4f orbitals contribute to chemical bonding by the shielding effect, the vibrational coupling between Ln(III) ion and the ligand is small. The little interaction also suppresses the structure change between the ground and excited states of Ln(III) ion, resulting in the similar shape and position of potential energy curves in these states. Typical potential curve shifts and emission phenomena of Ln(III) ions and organic molecules are shown in **Figure 1-4a**. The small offset of Ln(III) ion causes the intrinsic sharp emission bands in the region from visible to near-infrared (NIR) depending on Ln(III) ions (**Figure 1-4b**).[20] Ln(III) complexes exhibit discrete emission bands between levels based on Russell-Saunders terms, for example, $^5D_0 \rightarrow {}^7F_2$ transition of Eu(III) complexes with red emission, $^5D_4 \rightarrow {}^7F_5$ transition of Tb(III) complexes with green emission, and $^2F_{5/2} \rightarrow {}^2F_{7/2}$ transition of Yb(III) complexes with NIR emission. Important roles of organic ligands in luminescent Ln(III) complexes are (i) photosensitization through ligands and (ii) control of 4f electronic configurations.
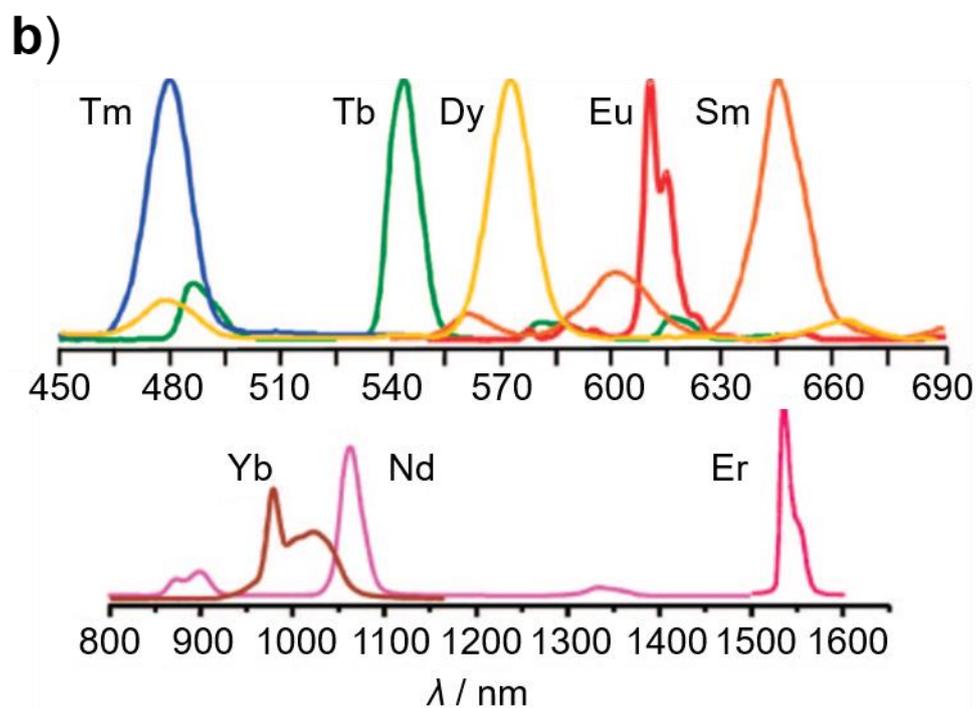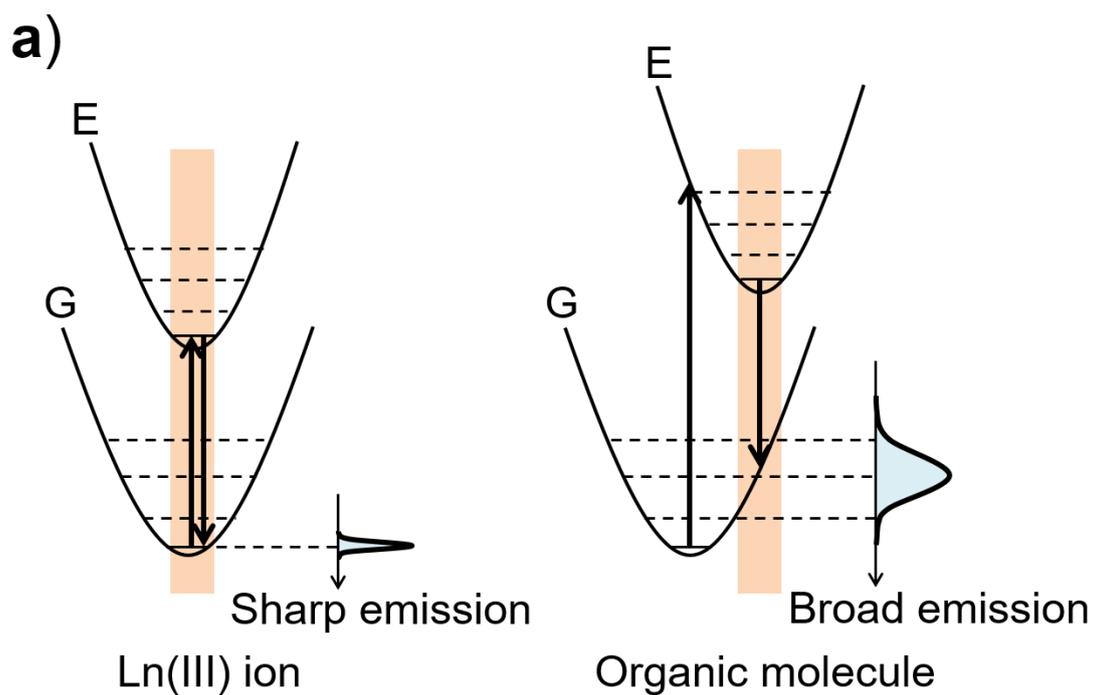
Figure 1-4. (**a**) Potential curve shifts and emission phenomena of Ln(III) ions and organic molecules. (**b**) The emission spectra of some Ln(III) complexes reprinted from ref [19].

Photosensitization effect of the ligand promotes Ln(III) ions to be excited state. Since the 4f-4f transitions of Ln(III) ion are electric dipole (ED) forbidden in terms of Laporte's parity selection rule, the absorption coefficient of Ln(III) ion is small (1 - 10 M^{-1} cm^{-1}).[10] Instead of Ln(III) ions, in 1942, Weissman discovered that light emission in Ln(III) complexes can be promoted when excitation is performed into the electronic levels of the coordinated organic ligands.[10] Organic ligands with a large absorption coefficient in ππ* transition ($10^4 – 10^5$ M^{-1} cm^{-1}) absorb the energy as an "antenna", and the energy is transferred to the Ln(III) ion. Typical schematic luminescence pathway of Ln(III) complexes is shown in **Figures 1-5a** and **1-5b**. Irradiated by ultraviolet radiation, the organic ligand in the Ln(III) complex is excited from the ground state (S_0) to the lowest singlet state (S_1). The S_1 can be deactivated by nonradiative intersystem crossing (ISC) from the S_1 to the triplet state (T_1) owing to the heavy atom effect of Ln(III) ion. The energy transfer (EnT) occurs from the T_1 to the excited states of Ln(III) ion and, finally, the Ln(III) ion undergo metal-centered luminescence.
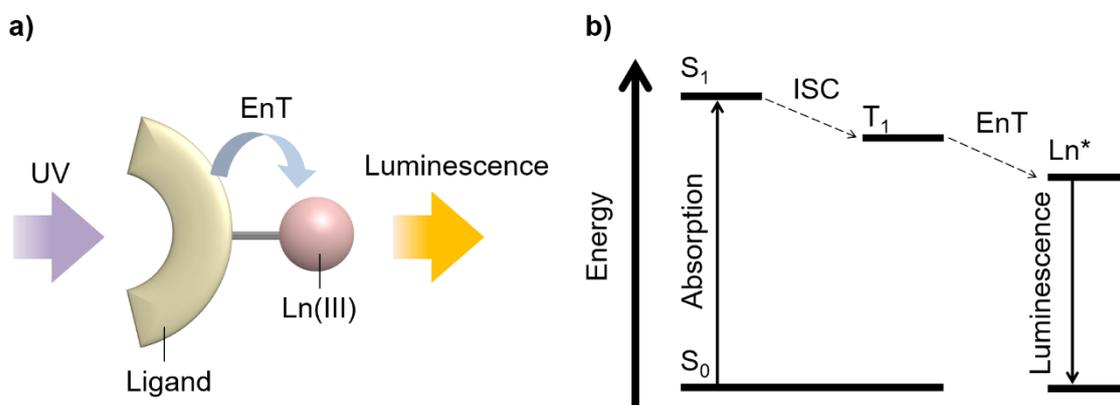

Figure 1-5. (**a**) Schematic image of photosensitization effect and (**b**) luminescence pathway of Ln(III) complex.

The ligand also plays a role in enhancing the electronic transition probability of Ln(III) ion by controlling the 4f electronic configurations under the influence of the crystal field. The crystal field causes mixing of some electronic configurations or levels related to Russell-Saunders term symbols in Ln(III) ion. In general, the electronic transition probability is described by dipole strength (D) in Equation (1.2),

$$D = |\vec{\mu}|^2 + |\vec{m}|^2 \,, \tag{1.2}$$

where $\vec{\mu}$ and $\vec{m}$ denote transition electric and transition magnetic dipole moments, respectively. The intraconfigurational 4f-4f transition of Ln(III) ion is ED forbidden and magnetic dipole (MD) allowed due to the same parity in the transition, meaning that the emission intensity in the 4f-4f transition of Ln(III) ion is weak.[10] In order to enhance the emission intensity, admixture of some electronic configurations with opposite parity into the pure 4f wave functions is required. In 1962, two authors, Judd and Ofelt, independently described a similar model for the induced ED transitions of lanthanides by the electronic configuration mixing, that is the Judd-Ofelt theory.[22,23] In the theory, crystal field of the ligand allow the mixing of electronic configurations with opposite parity (wave function: $|\varphi_{nl}\rangle$) such as 4f^{N-1}5d^1 configurations into the pure 4f^N wave functions ($|f^N J M_J\rangle$). A new wave function $|B\rangle$ is shown in Equation (1.3),

$$|B\rangle = |f^N J M_J\rangle + \sum_{\varphi_{nl}} \frac{\langle f^N J M_J |V| \varphi_{nl}\rangle}{E(f^N J M_J) - E(\varphi_{nl})} |\varphi_{nl}\rangle \,, \tag{1.3}$$

where V is the crystal field interaction operator, and $E(f^N J M_J) - E(\varphi_{nl})$ is the energy difference between the 4f^N configuration and the other electronic configurations with opposite parity. The $\vec{\mu}$ in the 4f-4f transition becomes partly allowed owing to the electronic configuration mixing induced by the crystal field. The mechanism of mixing between electronic configurations can be also applied to some levels, which is called *J*-mixing. For example, the electronic transition in $^5D_0 \rightarrow {}^7F_0$ of Eu(III) ion is partially allowed

by J-mixing between $^7F_0$ and other levels such as $^7F_2$ level. The crystal field also contributes to the splitting of $2J+1$ degenerate J sublevels, that is the Stark splitting. The splitting is also dependent on the site symmetry around Ln(III) ion and the intensity of the crystal field.

The intrinsic emission quantum yield (Φ_{Ln}) in the 4f-4f transition of Ln(III) complexes is defined by Equation (1.4),

$$\Phi_{Ln} = \frac{k_r}{k_r + k_{nr}}. \tag{1.4}$$

Here, k_r and k_{nr} are radiative and non-radiative constant, respectively. The k_r depends on an oscillator strength of the electronic transition, which is largely influenced by site symmetry around Ln(III) ion based on the surrounding ligands. The k_{nr} reflects the vibrational relaxation and the energy transfer quenching, i.e. back energy transfer (BEnT), from the excited state of Ln(III) ion to other excited states. The BEnT process is promoted when the excited state energy of Ln(III) ion is close to other excited state such as T_1 of the ligand, ligand-to-metal charge transfer (LMCT) state, and intraligand charge transfer (ILCT) state.[10,20] The schematic image of rate constants (k_r and k_{nr}) is shown in **Figure 1-6**. Overall emission quantum yield (Φ_L) of Ln(III) complexes excited at the coordinated ligands is given by Equation (1.5),

$$\Phi_L = \eta_{sens} \cdot \Phi_{Ln}. \tag{1.5}$$

Here, η_{sens} is the overall sensitization efficiency. The η depends on the efficiencies of ISC and EnT based on the combination of Ln(III) ions and ligands. As mentioned above, the photophysical properties of Ln(III) complexes are strongly influenced by the external environment based on the surrounding ligands.
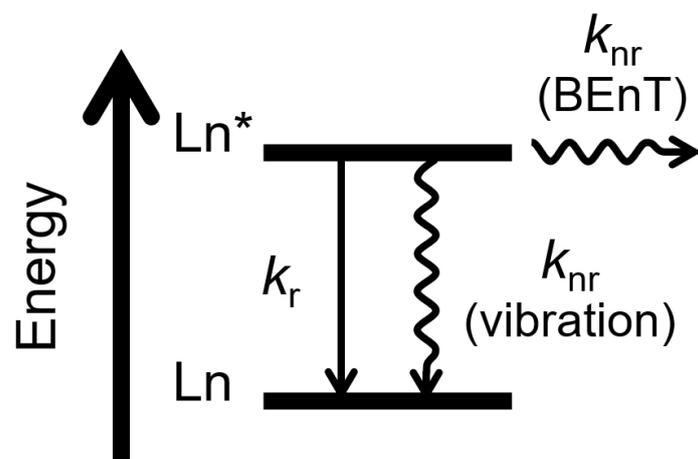
Figure 1-6. Schematic image of rate constants, k_r and k_{nr}. Ln* denotes the emitting level of Ln(III) ion.

1.3   Optical activities of chiral lanthanide compounds

Among the organic-inorganic hybrid lanthanide compounds, Ln(III) compounds coordinated with chiral organic molecules have attracted attention for their characteristic (natural) optical activities. Chiral molecules exhibit selective electronic transitions of left- and right-handed circularly polarized light with absorption (circular dichroism: CD) or emission (circularly polarized luminescence: CPL) according to the molecular chirality.[24] The schematic images of CD and CPL are shown in **Figure 1-7**. The magnitude of optical activities is defined by a dissymmetry factor (g) as Equation (1.6),[24]

$$g = \frac{2(T_L - T_R)}{T_L + T_R}. \tag{1.6}$$

T_L and T_R represent absorption coefficients (for CD) or emission intensities (for CPL) of left- or right-handed circularly polarized light, respectively. It is apparent that the g value is within $-2 \leq g \leq 2$.

The chirality of metal complexes is evaluated by coordination structures of the organic ligands around the metal ion induced by chiral environment. The chirality is classified to Λ-type or Δ-type for counterclockwise or clockwise helical structure,
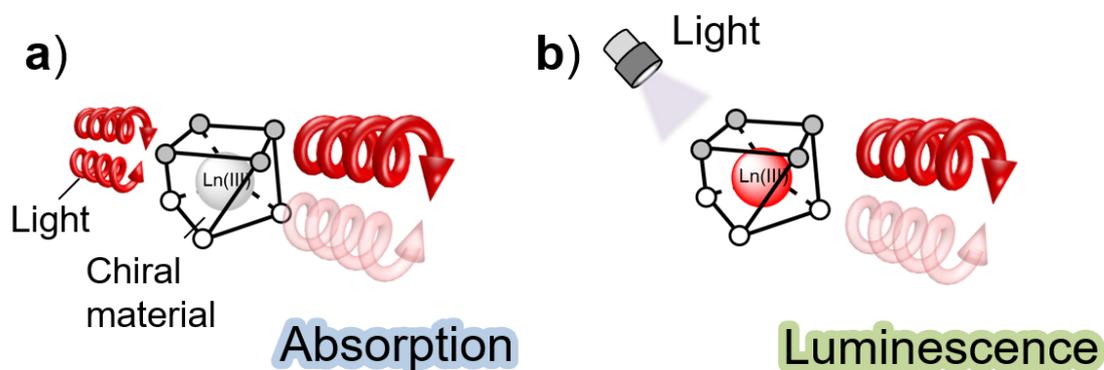

Figure 1-7. Schematic images of (**a**) CD and (**b**) CPL.

respectively, as viewed from the rotation axis.[25] For example, the Λ-type and Δ-type coordination structure of Ln(III) complex with eight-coordinate square-antiprism (SAP) is shown in **Figure 1-8**.
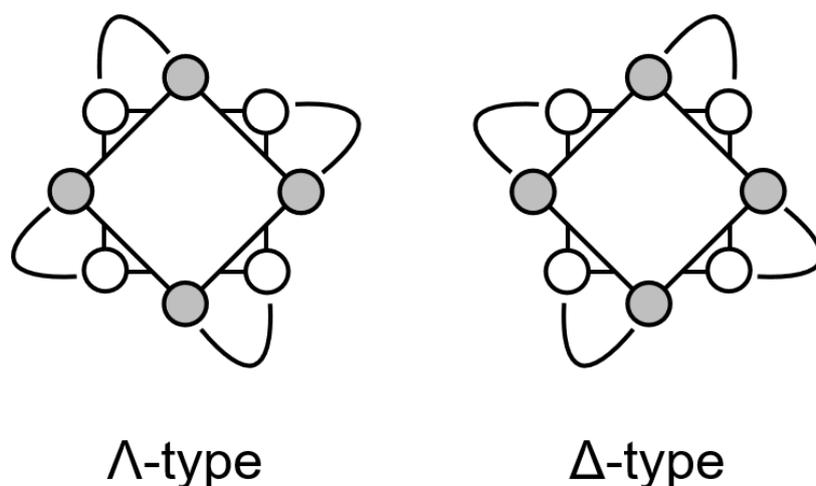

Λ-type   Δ-type

Figure 1-8. Chiral Λ- and Δ-type coordination structure of Ln(III) complex with SAP symmetry.

Luminescent lanthanide complexes with chiral ligands exhibit large CPL in the 4f-4f transitions.[26] Since Luk and Richardson reported the CPL of the Ln(III) complexes in 1974,[27] CPL of Ln(III) complexes has been studied extensively. The CPL properties of chiral Ln(III) complexes are dependent on the chiral and achiral organic ligands.[21,28–35] Some of Ln(III) complexes with chiral organic ligands are shown in **Figure 1-9**. The chiral ligands contain typical organic units, namely, 1,4,7,10-tetraazacyclododecane-1,4,7,10-tetraacetic acid (DOTA),[28,36] pyridine-2,6-bisoxazoline (Pybox),[32] 2,2'-bis(diphenylphosphino)-1,1'-binaphthyl (BINAP),[35] and camphor.[29,30] In solution, even
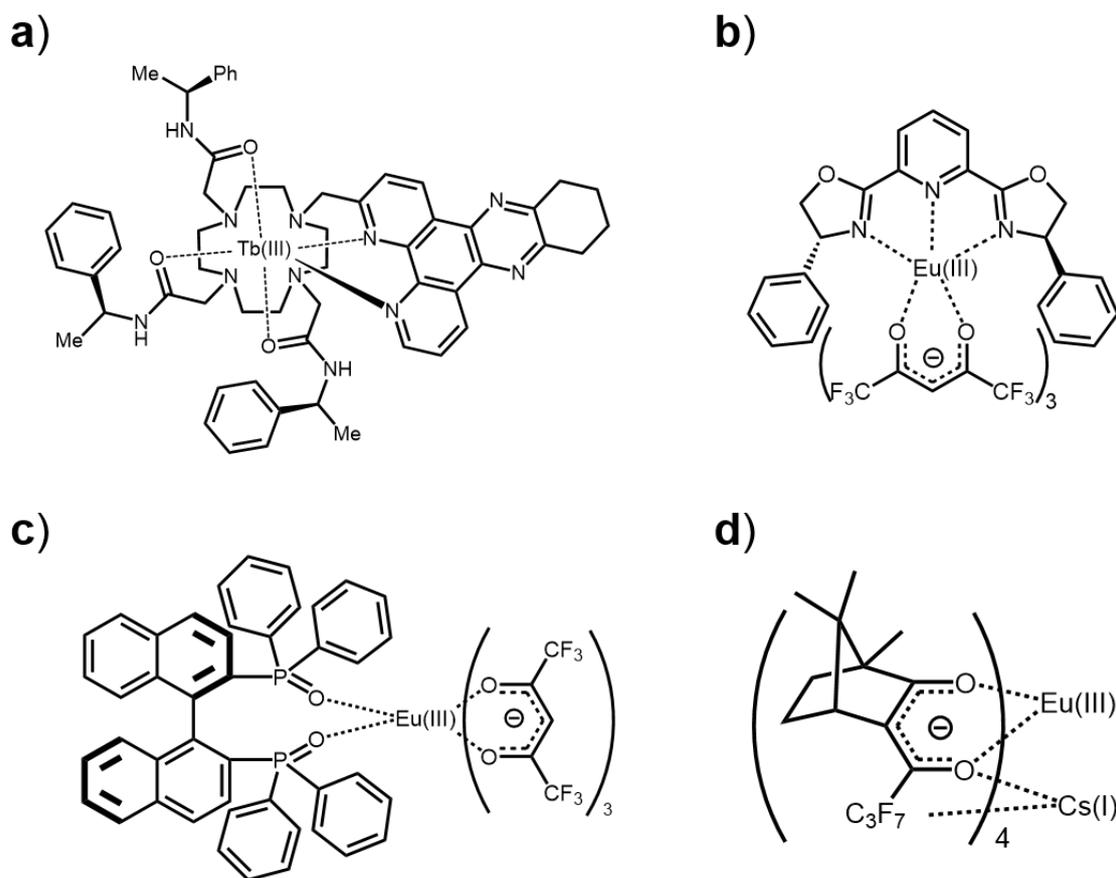
14

a)

b)

c)

d)

Figure 1-9. Examples of chiral Ln(III) complexes with (**a**) DOTA,[36] (**b**) pybox,[32] (**c**) BINAP,[35] and (**d**) camphor ligands.[29]

initially achiral Ln(III) complexes attain the chirality in the presence of external chiral environment, applying to a sensor of chiral molecules such as chiral amino acids and helical DNA.[34,37] The chiral environment also induces the chirality to Ln(III) core of polynuclear Ln(III) clusters and nanoparticles.[38–40] For example, CPL of a trinuclear Eu(III) array with chiral bipyridine-carboxylate ligands,[38] and the changeable CPL intensity of polynuclear Eu(III) clusters depending on the self-assembly structures[39] have been reported (**Figure 1-10**). The dissymmetry factor for CPL (g_{CPL}) of chiral Ln(III)
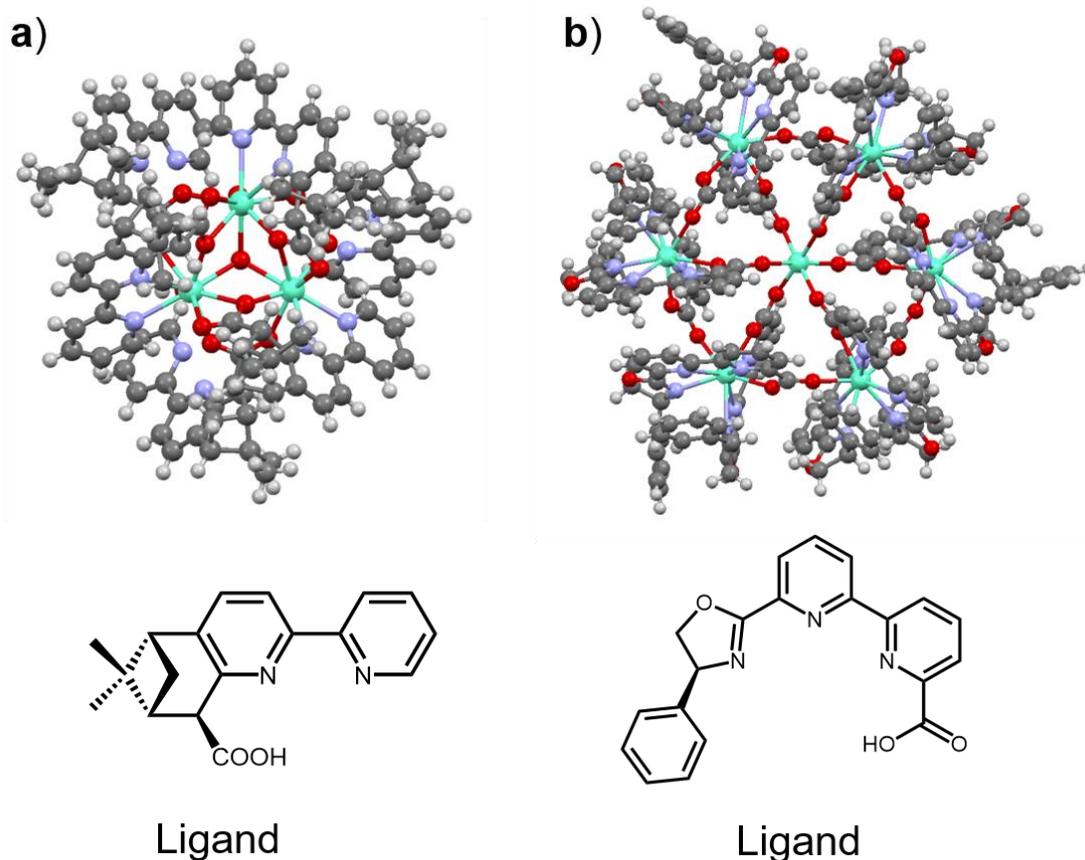
Figure 1-10. Examples of chiral Ln(III) clusters with (**a**) trinuclear[38] and (**b**) heptanuclear[39] structures and their chiral ligands.

complex depends on the combination of Ln(III) ion and organic ligands. Generally, chiral Ln(III) compound displays the g_{CPL} of 0.01 − 1, which is several hundred times as large as g_{CPL} value of typical chiral organic molecules or transition metal complexes.[26] The largest g_{CPL} value ever reported for Ln(III) complexes is 1.45 of Eu(III) complex with camphor derivative ligands.[30] The large g_{CPL} of Ln(III) compound has been attracted attention for various field such as bioimaging, 3D display, security tag, and data storage.

The large optical activity of Ln(III) ion can be understood in terms of the electric

and magnetic dipole components at the electronic transitions. In an isotropic system, the magnitude and sign of the optical activity are defined by rotatory strength (R) as Equation (1.7),[24,26]

$$R = \vec{\mu} \cdot \vec{m}.$$ (1.7)

In case of achiral molecules, R equals zero because an angle between $\vec{\mu}$ and $\vec{m}$ is 90 degrees. Chiral molecules without symmetry center break the orthogonality between $\vec{\mu}$ and $\vec{m}$, giving rise to the optical activity. The sign of R inverts according to the direction of $\vec{m}$ between enantiomers. The dissymmetry factor g of absorption/luminescence in Equation (1.8) is rewritten by D and R in Equation (1.7),

$$g = \frac{4R}{D^2} = \frac{4\vec{\mu} \cdot \vec{m}}{|\vec{\mu}|^2 + |\vec{m}|^2}.$$ (1.8)

Equation (1.7) indicates that the g value is governed by the ratio and direction of $\vec{\mu}$ and $\vec{m}$. The maximum g value is obtained when $\vec{\mu} = \vec{m}$. In a system of organic molecules, the g value is usually small due to larger contribution of electric field than magnetic field to the electronic transition in electromagnetic field ($|\vec{\mu}| \gg |\vec{m}|$).

The magnitudes of $\vec{\mu}$ and $\vec{m}$ for Ln(III) ions depend on a selection rule based on angular momentum quantum numbers (ΔS, ΔL, and ΔJ) at the transition. Richardson theoretically summarized the qualitative intensity of optical activity at the 4f-4f transitions corresponding to ΔJ of Ln(III) ion.[26] Among the 4f-4f transitions, large g_{CPL} value is observed in the magnetic allowed transition with $\Delta J = \pm 1$. Large g_{CPL} values which exceed more than unity ($g_{CPL} > 1$) are achieved at the $^5D_0 \rightarrow {}^7F_1$ transition of Eu(III) complexes and the $^4G_{5/2} \rightarrow {}^6H_{7/2}$ transition of Sm(III) complexes.[21,29–31,41,42]

1.4   Magneto-optical activities of lanthanide compounds

Polarization response such as optical activity in the electronic transition is not limited to the chiral compounds. Lanthanides also exhibit high performance for magneto-optical activities deriving from the 4f electrons by applying external magnetic field. The Faraday rotation and magnetic circular dichroism (MCD) are representatives of magneto-optical activities. Unlike optical activities of chiral compounds, magneto-optical activities are observed for compounds even without chiral structure. Thus, the origin is different from that of the optical activities.[43,44] Schematic images of the magneto-optical activities are shown in **Figures 1-11a** and **11b**. In 1845, Faraday discovered the first phenomenon of the interaction between light and magnetic field.[43] He demonstrated that the plane of polarization of linearly polarized light is rotated after passing through a material placed in a magnetic field parallel to the direction of the light. The rotation originates from the difference in refractive indices for left- and right-handed circularly polarized light. In the region of light absorption, the absorption coefficients for left- and right-handed circularly
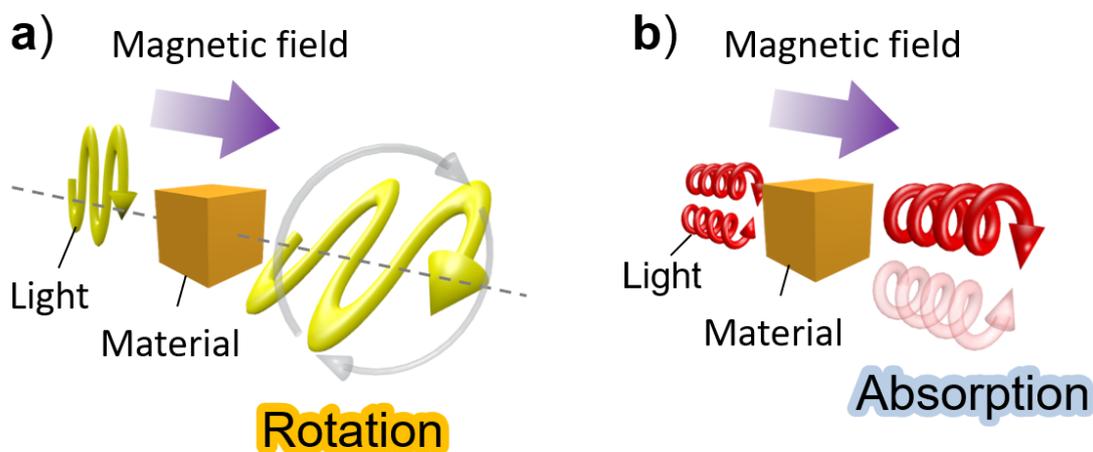

Figure 1-11. Schematic images of (**a**) the Faraday rotation and (**b**) MCD.

polarized light also vary individually in the presence of a magnetic field, bringing about MCD. The magnitude of MCD is represented by the ellipticity of the transmitted light according to the differential absorption coefficient. These magneto-optical activities originate from the Zeeman splitting of electronic states under the magnetic field.

Lanthanide compounds exhibit the large Faraday rotation in the 4f-5d transitions due to large angular momentum of the 4f electrons. In contrast to the 4f-4f transition, the 4f-5d transition is electric dipole-allowed, showing a large and broad spectrum during absorption (and luminescence). The Faraday effect has been applied to optical isolators employed in optical communication systems. Inorganic lanthanide compounds such as Tb(III)-doped borosilicate glass and Tb(III) garnet ceramics are representatives of the materials with the large magneto-optical activity in visible region (**Figure 1-12a**).[6,45–47] Among the Tb(III) garnet ceramics, terbium gallium garnet single crystals ($Tb_3Ga_5O_{13}$) are the most widely used commercial magneto-optical materials.[48] Lanthanide nanoparticles with 4f-5d transition have also been studied for promising candidates for an effective optical isolator. The Faraday rotational angles of EuS nanoparticles are dependent on the external environment induced by transition metals or organic ligands around the nanoparticles (**Figure 1-12b**).[49–52]

Ln(III) ions in solution have also been reported to exhibit the Faraday rotation attributed to 4f-5d transition in visible region. Watarai reported the magnitude of the Faraday effect of Tb(III) ion in aqueous solution was the largest among the Ln(III) ions, which suggested that the magnetic moment and the excited $4f^{N-1}5d^1$ states were involved.[53] In recent years, organic-inorganic hybrid lanthanide compounds have been investigated for controlling the Faraday effect by the modification of surrounding organic ligands around Ln(III) ions.[18,52] Nonanuclear Tb(III) clusters coordinated by salicylate

19

ligands, for example, were reported to exhibit the large Faraday rotation in the transition of the Tb(III) ion depending on the coordinated ligands around the Tb(III) ions (**Figure 1-12c**).[18] Lanthanide compounds with designed organic molecules are expected as new magneto-optical materials that control their polarization response by the external organic molecules.

Ln(III) complexes also exhibit large magneto-optical activities in the 4f-4f transitions. MCD in the 4f-4f transition is utilized for evaluating the electronic states of substances. Especially, the electronic states and coordination geometries of Eu(III) complexes have been investigated using MCD measurement.[54,55] The non-degenerate ground state ($^7F_0$) and the presence of excited states with a small total angular momentum J ($^5D_1$ and $^5D_2$) of Eu(III) ion enable to interpret the MCD spectrum. In case of eight-coordinate Eu(III) complexes, for example, MCD sign in the $^5D_2 \leftarrow {}^7F_0$ transition corresponds to the coordination geometry around Eu(III) ion.[54] Recently, the relationship between crystal field and MCD intensity is investigated, where small crystal field induces
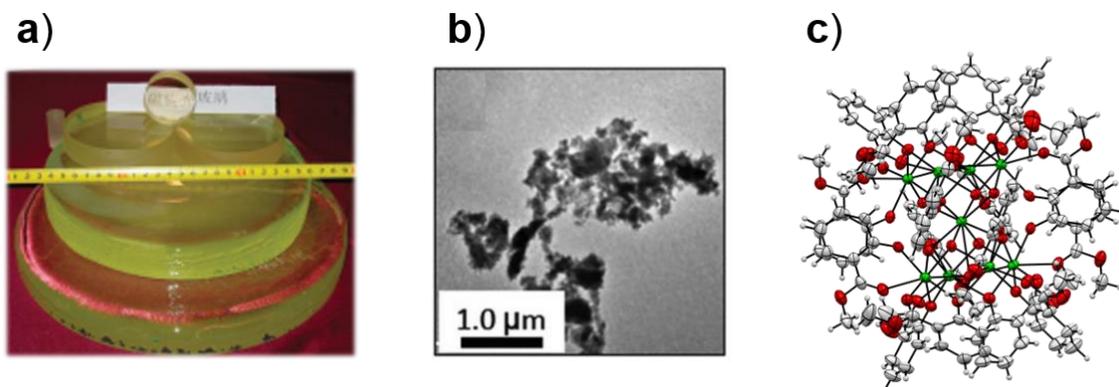
a)

b)

c)

1.0 μm

Figure 1-12. The Faraday effect materials. (**a**) Tb(III)-doped borosilicate glass,[45] (**b**) EuS nanoparticle with organic molecules,[56] and (**c**) nonanuclear Tb(III) cluster.[18]

a large MCD intensity.[57]

Generally, the Faraday effect is expressed by the complex magnetic rotation $\widehat{\Phi}$ as Equation (1.9),[43]

$$\widehat{\Phi} = \phi - i\theta \ . \qquad (1.9)$$

Here, ϕ represents the rotation related to the Faraday rotation, and θ represents the ellipticity for MCD. The ϕ and θ are related by Kramers-Kronig transforms, then, one quantity (ϕ or θ) is enough to determine the Faraday effect of the substance. Focusing on the ellipticity θ, the intensity of MCD is formulated by Equation (1.10),[43,58]

$$\theta \propto f_1 A + f_2 \left(B + \frac{C}{k_{\mathrm{B}} T} \right). \qquad (1.10)$$

Here, f_1 and f_2 are functions related to the shapes of the MCD bands associated with the *A* and with the *B* and *C* parameters, respectively. k_B is the Boltzmann constant. The three terms of an isolated transition $a \rightarrow j$ are expressed by Equations (1.11 – 1.13),

$$A = \frac{1}{2d_a} \sum (\langle j|\boldsymbol{m}|j\rangle - \langle a|\boldsymbol{m}|a\rangle) \cdot \mathrm{Im}(\langle a|\boldsymbol{\mu}|j\rangle \times \langle j|\boldsymbol{\mu}|a\rangle) \ , \qquad (1.11)$$

$$B = \frac{1}{d_a} \sum \mathrm{Im}(\sum_{k \neq j} \frac{\langle j|\boldsymbol{m}|k\rangle}{\Delta E_{kj}} \cdot \langle a|\boldsymbol{\mu}|j\rangle \times \langle k|\boldsymbol{\mu}|a\rangle + \sum_{k \neq a} \frac{\langle k|\boldsymbol{m}|a\rangle}{\Delta E_{ka}} \cdot \langle a|\boldsymbol{\mu}|j\rangle \times \langle j|\boldsymbol{\mu}|k\rangle) \ , \qquad (1.12)$$

$$C = \frac{1}{2d_a} \sum \langle a|\boldsymbol{m}|a\rangle \mathrm{Im}(\langle a|\boldsymbol{\mu}|j\rangle \times \langle j|\boldsymbol{\mu}|a\rangle) \ , \qquad (1.13)$$

where d_a is the degeneracy of *a*, $\boldsymbol{\mu}$ and $\boldsymbol{m}$ are the electric and magnetic dipole operators, respectively, and *k* is excited states except for the state *j*. The Faraday *A* and *C* terms primarily reflect the degeneracy of the excited and ground states, respectively, whereas the Faraday *B* term is related to the mixing of the ground and two or more excited states by the magnetic field. The shape of magneto-optical activity depends on the contributions of these terms. The schematic images of the Faraday terms are shown in **Figure 1-13**.
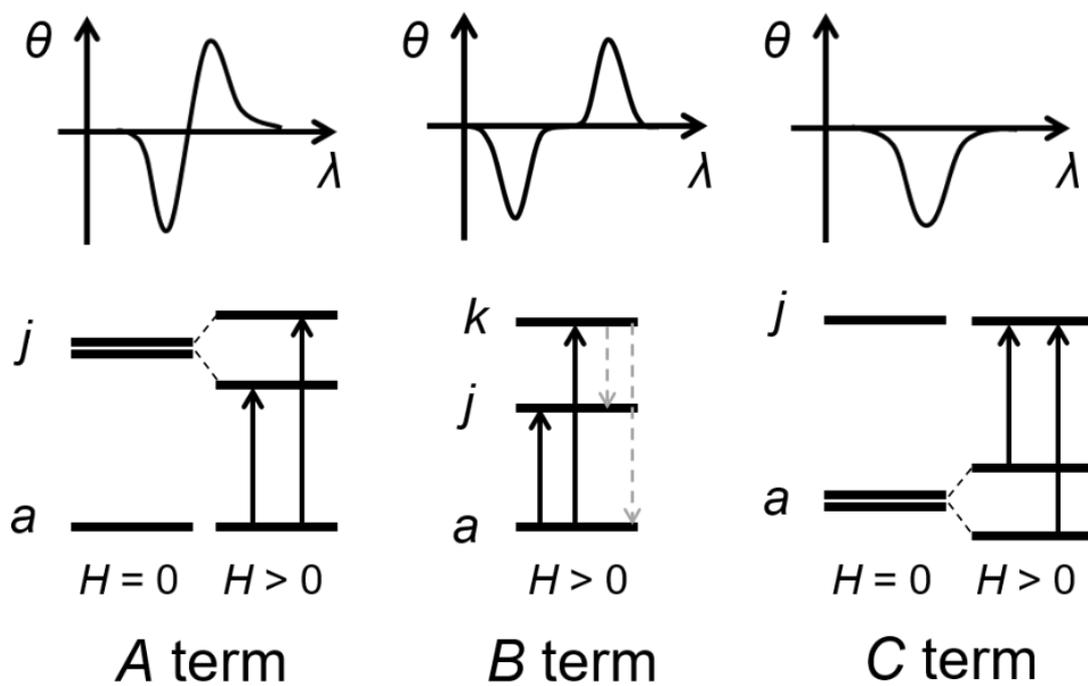
Figure 1-13. Schematic images of the Faraday *A*, *B*, and *C* terms.

1.5   Challenges of chiral lanthanide compounds

In contrast to the implementation to telecommunication system of the lanthanides' Faraday rotation, CPL application to optical materials with chiral Ln(III) complexes has not been fulfilled yet. One of challenges for developing CPL-active materials is to create a transparent emitter with large g_{CPL} and high emission efficiency (Φ_L). Transparent CPL materials are preferable to suppress the loss of polarization response by light scattering. For the dinuclear Cs(I)-Eu(III) complex with the largest g_{CPL} value (1.45), the Φ_L is small in transparent solution (1%)[30] and even in non-transparent solid state (3%).[42] Another difficulty in creating CPL materials is insufficient CPL mechanism of chiral Ln(III) complexes depending on external environment. Although various g_{CPL} values have been reported by the combination of chiral and achiral ligands,[21,28–30,34,59,60] detailed molecular design and mechanism for enhancing the optical activity of chiral Ln(III) complex are still unclear. Revealing the detail CPL mechanism depending on external environment should be a key to create a chiral Ln(III) complex with large CPL performance.

Since optical- and magneto-optical activities were discovered, many researchers had investigated the relationship between the two phenomena. The chirality is related to magneto-optical activity from the theoretical background.[43] However, no relationship has been observed for organic molecules with low optical activity.[61] Focused on high optical activity performance, chiral Ln(III) complexes have potential to clarify the interaction between optical- and magneto-optical activities. Clarifying the relationship between magneto-optical activity and molecular chirality is expected to develop a new field of chiral science.

1.6   Objective and Outline

The objective of this study is to develop chiral Ln(III) complexes for applying to CPL materials and clarifying the mechanism of optical- and magneto-optical activities depending on external environment. Optical- and magneto-optical activities of chiral Ln(III) complexes originate from the electronic transition of 4f electrons. As described above, the photophysical properties of Ln(III) complexes are strongly affected by the electronic state of Ln(III) ion, where mixing of wavefunctions by configuration- and/or *J*-mixing is occurred based on the external environments such as electric (crystal) field of coordinated ligands and/or external magnetic field (**Figure 1-13**). The optical- and magneto-optical activities of chiral Ln(III) complexes should be affected by the external environment. Clarifying the effect of electronic state (or configuration) mixing under external environments on optical activities of chiral Ln(III) complexes is required for controlling the optical- and magneto-optical activities and developing photo-functional chiral Ln(III) complexes.
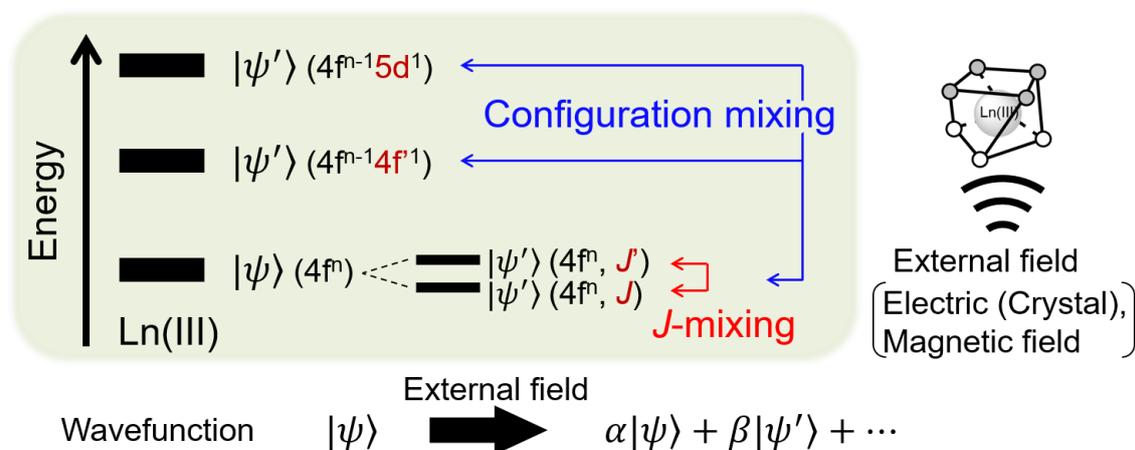

Figure 1-13. Mixing of wavefunctions of Ln(III) ion by external field.

In this research, the effect of the electronic state (or configuration) mixing to polarized light response, i.e. optical- and magneto-optical activities, of chiral Ln(III) complexes is focused on. Several kinds of chiral Ln(III) complexes are synthesized and the optical- and magneto-optical activities are investigated. The schematic image of this research is described in **Figure 1-14**.

In Chapter 1, photophysical properties and polarization response of Ln(III) compounds depending on external environment are overviewed. The objective of this research is described in relation to the electronic state and chirality of Ln(III) complexes under surrounding environment.

In Chapter 2, a chiral Eu(III) complex with large g_{CPL} value in film state is explored for the application to transparent materials with CPL property. The coordination structure and electronic state of a Eu(III) complex with camphor derivative ligands are controlled by an achiral phosphine oxide molecule. The emission and CPL properties of the Eu(III) complex in film state are investigated. An application model of the film as a CPL material is discussed.

In Chapter 3, the detail CPL mechanism of chiral Ln(III) complexes is evaluated by measuring CPL of Eu(III) complexes in solution, where the effect of electronic state mixing is discussed. Previously reported chiral Eu(III) complexes with camphor derivative ligands and phosphine oxide ligands are synthesized. The enhancement of CPL intensity depending on external achiral molecules around the Eu(III) ion is investigated from the viewpoint of the electronic state mixing.

In Chapter 4, electronic state mixing of chiral Ln(III) complex is applied to magneto-optical activity, in an attempt to develop a new field of polarization response induced by chirality and magnetic field. CPL properties and the Faraday effect of novel

nonanuclear Tb(III) clusters with chiral salicylate ligands are investigated. The relationship between magneto-optical activity and molecular chirality are discussed.

In Chapter 5, finally, summary and outlook of the research are described.

Chapter 1
Photophysical properties of chiral Ln(III) complex

Chapter 2
Novel Eu(III) complex for CPL application

Chapter 3
CPL mechanism of chiral Eu(III) complex

Chapter 4
Faraday rotation under chiral environment

Chapter 5
Summary and outlook

Achiral molecule

Magnetic field

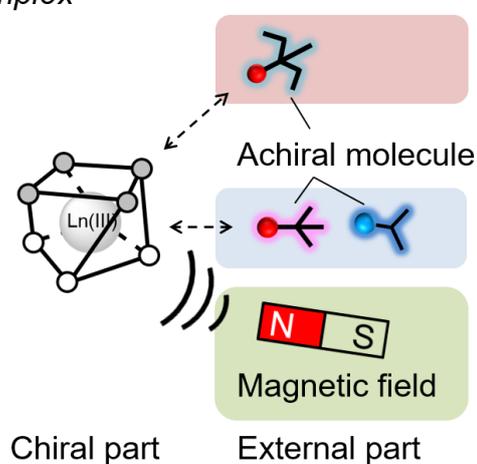Chiral part   External part

Figure 1-14. Schematic image of this research.

1.7   References

[1]   J. C. G. Bünzli, C. Piguet, *Chem. Soc. Rev.* **2005**, *34*, 1048–1077.

[2]   S. V Eliseeva, J.-C. G. Bünzli, *Chem. Soc. Rev.* **2010**, *39*, 189–227.

[3]   P. Dorenbos, *J. Mater. Chem.* **2012**, *22*, 22344–22349.

[4]   R. Sessoli, A. K. Powell, *Coord. Chem. Rev.* **2009**, *253*, 2328–2341.

[5]   K. Binnemans, *Chem. Rev.* **2009**, *109*, 4283–4374.

[6]   E. G. Villora, P. Molina, M. Nakamura, K. Shimamura, T. Hatanaka, A. Funaki, K. Naoe, *Appl. Phys. Lett.* **2011**, *99*, 1–4.

[7]   L. Armelao, S. Quici, F. Barigelletti, G. Accorsi, G. Bottaro, M. Cavazzini, E. Tondello, *Coord. Chem. Rev.* **2010**, *254*, 487–505.

[8]   G. H. Dieke, H. M. Crosswhite, *Appl. Opt.* **1963**, *2*, 675–686.

[9]   J.-C. G. Bünzli, S. V Eliseeva, in *Springer Ser. Fluoresc.*, **2010**, 1–45.

[10]   J.-C. G. Bünzli, *Coord. Chem. Rev.* **2015**, *293–294*, 19–47.

[11]   Y. Hasegawa, T. Nakanishi, *RSC Adv.* **2015**, *5*, 338–353.

[12]   J. C. G. Bünzli, C. Piguet, *Chem. Rev.* **2002**, *102*, 1897–1928.

[13]   W. H. Watson, R. J. Williams, N. R. Stemple, *J. Inorg. Nucl. Chem.* **1972**, *34*, 501–508.

[14]   C. S. Erasmus, J. C. A. Boeyens, *Acta Crystallogr. Sect. B Struct. Crystallogr. Cryst. Chem.* **1970**, *26*, 1843–1854.

[15]   K. Miyata, T. Ohba, A. Kobayashi, M. Kato, T. Nakanishi, K. Fushimi, Y. Hasegawa, *Chempluschem* **2012**, *77*, 277–280.

[16]   M. A. Singh-Wilmot, R. A. Sinclair, M. Andrews, C. Rowland, C. L. Cahill, M. Murugesu, *Polyhedron* **2013**, *53*, 187–192.

[17]   R. D. Shannon, *Acta Cryst.* **1976**, *A32*, 751.

[18]   T. Nakanishi, Y. Suzuki, Y. Doi, T. Seki, H. Koizumi, K. Fushimi, K. Fujita, Y. Hinatsu, H. Ito, K. Tanaka, Y. Hasegawa, *Inorg. Chem.* **2014**, *53*, 7635–41.

[19]   D. T. Thielemann, A. T. Wagner, E. Rösch, D. K. Kölmel, J. G. Heck, B. Rudat, M. Neumaier, C. Feldmann, U. Schepers, S. Bräse, P. W. Roesky, *J. Am. Chem. Soc.* **2013**, *135*, 7454–7457.

[20]   J. C. G. Bünzli, *Chem. Rev.* **2010**, *110*, 2729–2755.

[21]   F. Zinna, L. Di Bari, *Chirality* **2015**, *27*, 1–13.

[22]   B. R. Judd, *Phys. Rev.* **1962**, *127*, 750–761.

[23]   H. L. Alamos, **2013**, *136*, 221–239.

[24]   S. F. Mason, *Molecular Optical Activity and the Chiral Discriminations*, Cambridge University Press, **1982**.

[25]   L. Di Bari, P. Salvadori, *ChemPhysChem* **2011**, *12*, 1490–1497.

[26]   F. Richardson, *Inorg. Chem.* **1980**, *19*, 2806–2812.

[27]   W. R. G. Baeyens, *Luminescence Techniques in Chemical and Biochemical Analysis*, CRC Press, **1990**.

[28]   R. Carr, N. H. Evans, D. Parker, *Chem. Soc. Rev.* **2012**, *41*, 7673–7686.

[29]   J. L. Lunkley, D. Shirotani, K. Yamanari, S. Kaizaki, G. Muller, *Inorg. Chem.* **2011**, *50*, 12724–12732.

[30]   J. Kumar, B. Marydasan, T. Nakashima, T. Kawai, J. Yuasa, *Chem. Commun.* **2016**, *52*, 9885–9888.

[31]   T. Harada, H. Tsumatori, K. Nishiyama, J. Yuasa, Y. Hasegawa, T. Kawai, *Inorg. Chem.* **2012**, *51*, 6476–6485.

[32]   J. Yuasa, T. Ohno, K. Miyata, H. Tsumatori, Y. Hasegawa, T. Kawai, *J. Am. Chem. Soc.* **2011**, *133*, 9892–9902.

[33]   R. Carr, L. Di Bari, S. Lo Piano, D. Parker, R. D. Peacock, J. M. Sanderson, *Dalton Trans.* **2012**, *41*, 13154.

[34]   T. Uchida, K. Nozaki, M. Iwamura, *Chem. Asian J.* **2016**, *11*, 2415–2422.

[35]   T. Harada, Y. Nakano, M. Fujiki, M. Naito, T. Kawai, Y. Hasegawa, *Inorg. Chem.* **2009**, *48*, 11242–11250.

[36]   C. P. Montgomery, B. S. Murray, E. J. New, R. Pal, D. Parker, *Acc. Chem. Res.* **2009**, *42*, 925–937.

[37]   G. Muller, J. P. Riehl, *J. Fluoresc.* **2005**, *15*, 553–558.

[38]   O. Mamula, M. Lama, S. G. Telfer, A. Nakamura, R. Kuroda, H. Stoeckli-Evans, R. Scopelitti, *Angew. Chem. Int. Ed. Engl.* **2005**, *44*, 2527–31.

[39]   G. Bozoklu, C. Gateau, D. Imbert, J. Pécaut, K. Robeyns, Y. Filinchuk, F. Memon, G. Muller, M. Mazzanti, *J. Am. Chem. Soc.* **2012**, *134*, 8372–8375.

[40]   M. Lama, O. Mamula, G. S. Kottas, F. Rizzo, L. De Cola, A. Nakamura, R. Kuroda, H. Stoeckli-Evans, *Chem. Eur. J.* **2007**, *13*, 7358–7373.

[41]   J. Yuasa, H. Ueno, T. Kawai, *Chem. Eur. J.* **2014**, *20*, 8621–8627.

[42]   F. Zinna, U. Giovanella, L. Di Bari, *Adv. Mater.* **2015**, *27*, 1791–1795.

[43]   P. N. Schatz, A. J. McCaffery, *J. Quart. Rev.* **1969**, *23*, 552–584.

[44]   J. A. Schellman, *Acc. Chem. Res.* **1968**, *1*, 144–151.

[45]   W. Li, K. Zou, M. Lu, B. Peng, W. Zhao, *Int. J. Appl. Ceram. Technol.* **2010**, *7*, 369–374.

[46]   H. Lin, S. Zhou, H. Teng, *Opt. Mater.* **2011**, *33*, 1833–1836.

[47]   H. Yoshida, K. Tsubakimoto, Y. Fujimoto, K. Mikami, H. Fujita, N. Miyanaga, H. Nozawa, H. Yagi, T. Yanagitani, Y. Nagata, H. Kinoshita, *Opt. Express* **2011**, *19*, 15181.

[48]   H. Yin, Y. Gao, Y. Gong, R. Buchanan, J. Song, M. Li, *Ceram. Int.* **2018**, *44*, 10929–10933.

[49]   Y. Hasegawa, M. Maeda, T. Nakanishi, Y. Doi, Y. Hinatsu, K. Fujita, K. Tanaka, H. Koizumi, K. Fushimi, *J. Am. Chem. Soc.* **2013**, *135*, 2659–2666.

[50]   A. Kawashima, T. Nakanishi, T. Shibayama, S. Watanabe, K. Fujita, K. Tanaka, H. Koizumi, K. Fushimi, Y. Hasegawa, *Chem. Eur. J.* **2013**, *19*, 14438–14445.

[51]   A. Kawashima, T. Nakanishi, Y. Kitagawa, K. Fushimi, Y. Hasegawa, *Phys. Status Solidi Appl. Mater. Sci.* **2016**, *213*, 178–182.

[52]   A. Kawashima, T. Nakanishi, K. Fushimi, Y. Hasegawa, *Mol. Cryst. Liq. Cryst.* **2013**, *579*, 69–76.

[53]   K. Miyamoto, K. Isai, M. Suwa, H. Watarai, *J. Am. Chem. Soc.* **2009**, *131*, 6328–6329.

[54]   K. Binnemans, *Coord. Chem. Rev.* **2015**, *295*, 1–45.

[55]   L. V. Fluyt, *J. Alloys Compd.* **1994**, *208*, 51–54.

[56]   A. Kawashima, T. Nakanishi, K. Fushimi, Y. Hasegawa, *Mol. Cryst. Liq. Cryst.* **2013**, *579*, 69–76.

[57]   Y. Kitagawa, S. Wada, K. Yanagisawa, T. Nakanishi, K. Fushimi, Y. Hasegawa, *ChemPhysChem* **2016**, *17*, 845–849.

[58]   C. Djerassi, C. Djerassi, E. Bunnenberg, E. Bunnenberg, D. L. Elder, D. L. Elder, *Pure Appl. Chem.* **1971**, *25*, 57–90.

[59]   S. Petoud, G. Muller, E. G. Moore, J. Xu, J. Sokolnicki, J. P. Riehl, U. N. Le, S. M. Cohen, K. N. Raymond, *J. Am. Chem. Soc.* **2007**, *129*, 77–83.

[60]   L. Armelao, D. B. Dell'Amico, L. Bellucci, G. Bottaro, L. Di Bari, L. Labella, F. Marchetti, S. Samaritani, F. Zinna, *Inorg. Chem.* **2017**, *56*, 7010–7018.

[61]   L. D. Barron, *Nat. Mater.* **2008**, *7*, 691–692.

Chapter 2

Extra-large CPL performance and high emission efficiency of chiral Eu(III) complex in film state

2.1　Introduction

　　Luminescent Ln(III) complexes with chiral ligands exhibit large CPL intensity in the 4f-4f transitions compared with that of chiral organic molecules. Among chiral lanthanide complexes, chiral Eu(III) complexes with camphor derivative ligands have been attracted attention for luminescent materials with large CPL performance.[1–7] As camphor derivative molecules, (+/-)-3-(trifluoroacetyl)camphor (+/-tfc) and 3-(perfluorobutyryl)-(+/−)-camphor (+/-pfc) are the famous ligands with β-diketonate group (**Figure 2-1a**). The Eu(III) complexes with camphor derivative ligands exhibit large g_{CPL} values more than unity ($g_{CPL} > 1$) in the magnetic dipole-allowed $^5D_0 \rightarrow {}^7F_1$ transitions, the value of which cannot be achieved for any Eu(III) complexes without camphor ligands. The maximum $|g_{CPL}|$ value (1.45) has been observed for a dinuclear Cs(I)-Eu(III) complex with four +/-pfc ligands (**Figure 2-1b**).[3] The extra-large g_{CPL} value of the dinuclear Cs(I)-Eu(III) complex in solution lead to naked eye visualization of CPL using circularly polarized filter. Bari and coworker have applied the Cs(I)-Eu(III) complex as a transparent circularly polarized electroluminescence material by mixing with polymer-based device.[7] In spite of the high CPL performance of the camphor Eu(III) complexes, CPL application to optical materials has not been fulfilled yet due to the low emission efficiency (Φ_L). For the dinuclear Cs(I)-Eu(III) complex, the Φ_L is small in transparent solution (1%)[3] and even in non-transparent solid state (3%).[7] The Φ_L values of Eu(III) complexes with chiral +tfc ligands are increased by the introduction of achiral phosphine oxide ligands.[8] Hasegawa revealed that the Φ_L values of mononuclear Eu(III) complex, Eu(+tfc)$_3$(tppo)$_2$ (tppo: triphenylphosphine oxide), and Eu(III) coordination polymer, [Eu(+tfc)$_3$(dpbp)]$_n$ (dpbp: 4,4'-bis(diphenylphosphoryl)biphenyl), were 5% and 30% in solid, respectively (**Figures 2-1c** and **2-1d**).[8] However, the camphor Eu(III) complexes were non-
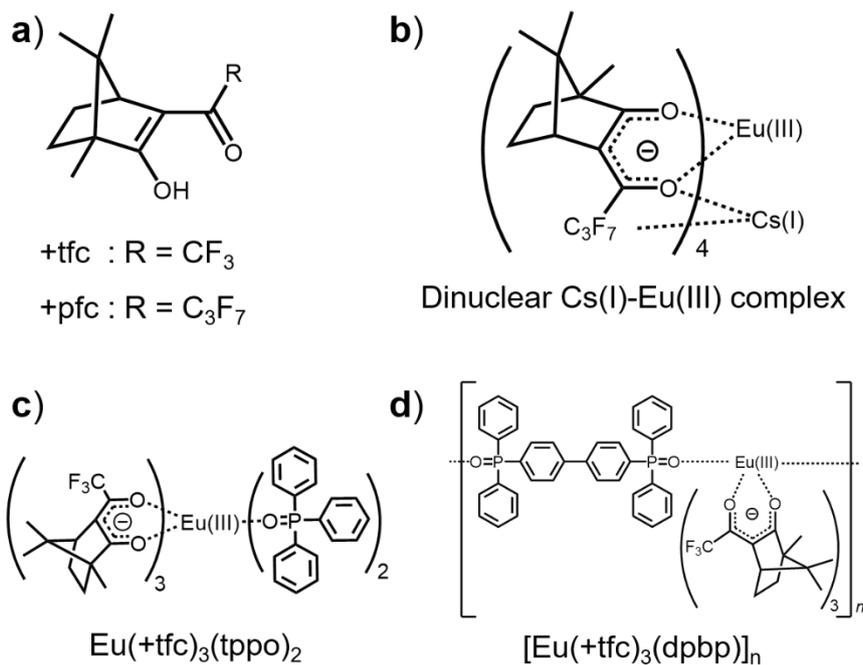
Figure 2-1. Structures of (**a**) camphor derivative ligands, (**b**) dinuclear Cs(I)-Eu(III) complex,[3] (**c**) Eu(+tfc)$_3$(tppo)$_2$,[8] and (**d**) [Eu(+tfc)$_3$(dpbp)]$_n$.[8]

transparent for their high crystallinity, and the g_{CPL} values were small; g_{CPL} = +0.09 for Eu(+tfc)$_3$(tppo)$_2$, and +0.17 for [Eu(+tfc)$_3$(dpbp)]$_n$. The coordination structure and photophysical properties of camphor Eu(III) complexes were dependent on the external achiral molecules, which is expected to develop a novel transparent camphor Eu(III) complex with large g_{CPL} and Φ_L values by controlling external achiral molecules.

To achieve the transparent Eu(III) complex, the author focused on binary co-amorphous system. In the co-amorphous system, mixture of two or more small molecules instead of polymers prevents from crystallization, leading to an amorphous state by non-covalent interaction between these molecules.[9–11] The system has been studied especially in the field of pharmaceutics, which has been achieved by the
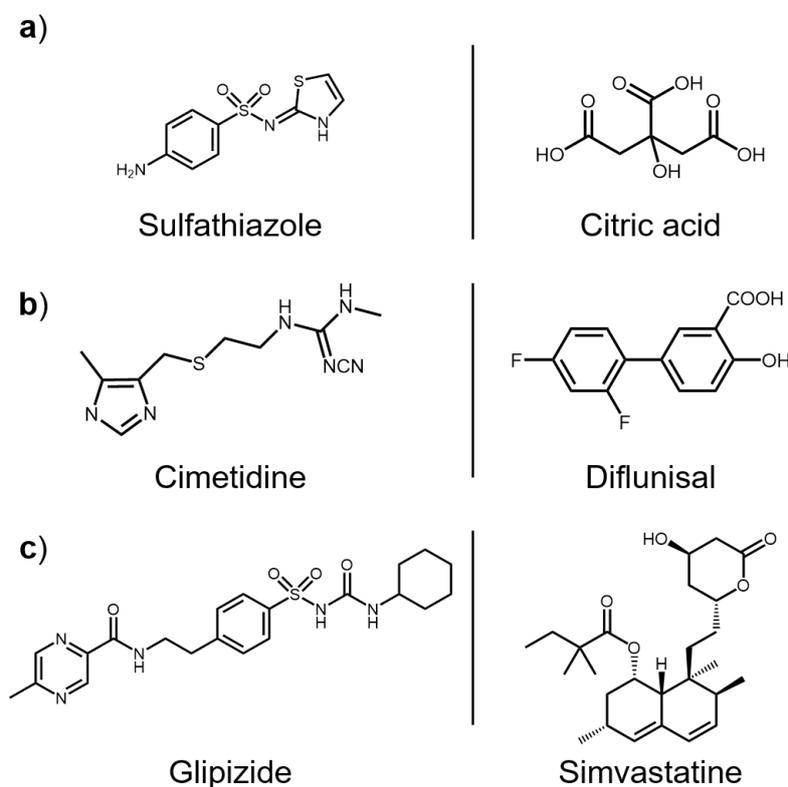
a)

Sulfathiazole   Citric acid

b)

Cimetidine   Diflunisal

c)

Glipizide   Simvastatine

Figure 2-2. Structures of co-amorphous compounds. (**a**) sulfathiazole/acyclovir,[12] (**b**) cimetidine/diflunisal,[13] and (**c**) glipizide/simvastatin.[14]

combination of sulfathiazole/citric acid,[12] cimetidine/diflunisal,[13] glipizide/simvastatin,[14] for example (**Figure 2-2**). Eu(III) complexes also form amorphous state by the combination of ligands.[15–17] Bazan reported amorphous Eu(III) complex by introducing bulky ligands with alkoxy groups to prevent crystallization (**Figure 2-3**).[15] Some kinds of co-amorphous compounds can be prepared by co-grinding method without any solvent as well as general synthesis in solution. The structure change of mixed compounds by grinding is also reported in mechanochemical synthesis of crystalline metal complexes.[18–21] The solvent-free synthesis is desirable for application in industry in terms of the simple procedure and safety aspect.
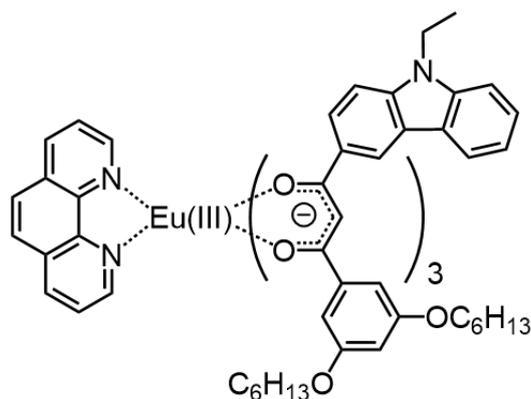
Figure 2-3. Structure of amorphous Eu(III) complex.[15]

In this chapter, a non-crystalline novel chiral Eu(III) complex by the combination of a camphor Eu(III) complex and an external achiral ligand is reported, which is prepared by mechanochemical synthesis and solution synthesis. As starting compounds, camphor Eu(III) complex [Eu(+tfc)$_3$(H$_2$O)$_2$] and tris(2,6-dimethoxyphenyl)phosphine oxide (tdmpo) are chosen as the chiral Eu(III) complex and the external achiral molecule, respectively (**Figure 2-4**). The bulky methoxy groups close to P=O group in the tdmpo molecule are expected to generate several conformers of the Eu(III) complex by non-covalent interaction with the camphor Eu(III) complex. Non-crystalline luminescent Eu(III) complexes were obtained by grinding of Eu(+tfc)$_3$(H$_2$O)$_2$ and several equivalents of tdmpo molecules. Furthermore, transparent films of the Eu(III) complex were obtained by evaporating mixture of Eu(+tfc)$_3$(H$_2$O)$_2$ and tdmpo in solution. The coordination structure and photophysical properties of the Eu(III) complex were characterized by XRD, DSC, emission, emission lifetime, and emission quantum yield measurements. The optical activity of the transparent film was evaluated by CPL measurement. A simple

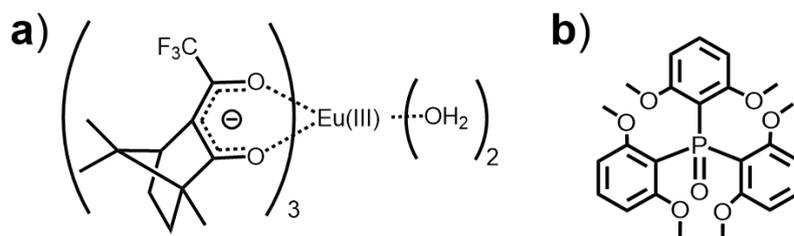model of CPL security ink of the film was also investigated.

Figure 2-4. Structure of (**a**) Eu(+tfc)$_3$(H$_2$O)$_2$ and (**b**) tdmpo.

2.2   Methods

Materials

      Europium(III) acetate *n*-hydrate, acetone-d_6 (99.9%) and 28% ammonia solution were purchased from Wako Pure Chemical Industries Ltd. (+)-3-(trifluoroacetyl)camphor and (-)-3-(trifluoroacetyl)camphor were purchased from Sigma-Aldrich Co. Triphenyl phosphine oxide and tris(2,6-dimethoxyphenyl)phosphine was purchased from Tokyo Chemical Industry Co., Ltd. All other chemicals and solvents were of reagent grade and were used without further purification.

Apparatus

      Electrospray ionization mass spectra were measured by using a Thermo Scientific Exactive instrument. Elemental analyses were performed on an Exeter Analytical CE440. XRD patterns were characterized by a RIGAKU X-ray diffractometer RINT 2200. Differential scanning calorimetry spectrum was measured using a EXSTAR DSC 7020 analyzer. Emission spectra and emission lifetimes were measured using a Horiba/Jobin-Yvon FluoroLog-3 spectrofluorometer. CPL spectra were measured using a JASCO CPL-200 spectrofluoropolarimeter.

Synthesis of Tris(2,6-dimethoxyphenyl)phosphine oxide (tdmpo)

      Tris(2,6-dimethoxyphenyl)phosphine (8.84 g, 0.02 mmol) was dissolved in dichloromethane (30 mL) in a 100 mL flask. The solution was cooled in an ice bath and H_2O_2 solution (5 mL) was added slowly to the solution. The mixture was stirred for 3 h. The product was extracted with dichloromethane and saturated NaCl aqueous solution. The organic layer was dried with anhydrous $MgSO_4$, and the solvent was evaporated.

The obtained oil was precipitated with acetone and hexane. The precipitate was filtered and washed with acetone to afford white powder.

[tdmpo]. Yield: 3.95 g (41%). δ/ppm = 7.23 (t, 3H, J = 8 Hz, Ar), 6.48 (dd, 6H, J = 8 and 4.8 Hz, Ar), 3.51 (s, 18H, CH$_3$). ESI-MS (m/z): [M+H]$^+$ calculated for C$_{24}$H$_{28}$O$_7$P, 459.15; found, 459.16. Elemental analysis: Calculated for C$_{24}$H$_{27}$O$_7$P: C, 62.88%, H, 5.94%. Found: C, 62.55%, H, 5.88%.
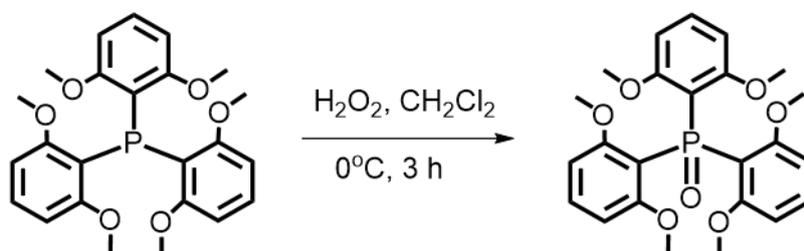
Scheme 2-1. Synthesis of tris(2,6-dimethoxyphenyl)phosphine oxide.

Synthesis of Tris(3-trifluoroacetyl-(+)-camphorato)europium(III) hydrate ([Eu(+tfc)$_3$(H$_2$O)$_2$])

Europium(III) acetate *n*-hydrate (0.36 g) was dissolved in distilled water (150 mL) and a few drops of 28% ammonia solution were added. (+)-3-triflouroacetyl camphor (+tfc, 0.50 g, 2.0 mmol) in methanol (20 mL) was added to the solution and the mixture was stirred for 3 h at room temperature. The obtained powder was washed with distilled water to afford yellow powder.

[Eu(+tfc)$_3$(H$_2$O)$_2$]. Yield: 0.42 g (68%). Elemental analysis: Calculated for C$_{36}$H$_{46}$EuF$_9$O$_8$: C, 46.51%, H, 4.99%. Found: C, 46.45%, H, 4.91%.
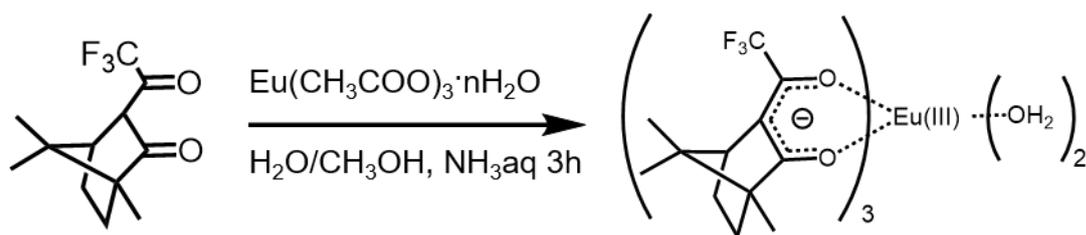
Scheme 2-2. Synthesis of Eu(+tfc)$_3$(H$_2$O)$_2$.

Synthesis of Tris(3-trifluoroacetyl-(-)-camphorato)europium(III) dihydrate ([Eu(-tfc)$_3$(H$_2$O)$_2$])

[Eu(-tfc)$_3$(H$_2$O)$_2$] was prepared using the same method for [Eu(+tfc)$_3$(H$_2$O)$_2$], starting from (-)-3-triflouroacetyl camphor, yielding yellow powder.

Yield: 0.55 g (89%). Elemental analysis [M-H$_2$O]: Calculated for C$_{36}$H$_{44}$EuF$_9$O$_7$: C, 47.43%, H, 4.86%. Found: C, 47.98%, H, 4.83%.

Mechanochemical preparation of Eu(III) complexes with phosphine oxide

Eu(+tfc)$_3$(H$_2$O)$_2$ and *n* equivalents of phosphine oxide (tdmpo or tppo; *n* = 0, 1, 2, or 3) were mixed so that total amount of the mixture was 20 mg. The mixture (20 mg) was manually ground using a mortar and pestle for 15 minutes.

Preparation of films of Eu(III) complexes

Eu(+/-tfc)$_3$(H$_2$O)$_2$ (3 mg, 0.003 mmol) and *n* equivalents of tdmpo (1.5 mg, 3.0 mg, or 4.5 mg for *n* = 1, 2, or 3, respectively) was dissolved in dichloromethane (0.1 mL). The solution was casted to a glass substrate and slowly evaporated, yielding transparent film of the Eu(III) complex.

Optical setup of CPL measurement for naked eye determination

A LED light (λ_{ex} = 365 nm), a sample of Eu(III) complex, a bandpass filter (TECHSPEC, 594 nm), a λ/4 plate (THORLABS) with a motorized precision rotation stage and controller (THORLABS), and a linear polarizer (THORLABS) were set in line. Photographs of the luminescent sample after passing through the filters were taken by a commercially available smartphone.

2.3 Results and discussion

2.3.1 Coordination structure of Eu(III) complex

Figures 2-5 and 2-6 show the grinding synthesis of a chiral Eu(III) complex with

tdmpo or tppo molecules, respectively. After grinding the mixture of less-luminescent

Eu(+tfc)$_3$(H$_2$O)$_2$ and n equivalents of tdmpo molecules (Eu(+)-L(n); n = 1, 2, 3) or tppo

molecules (Eu(+)_tppo(n); n = 1, 2, 3), red luminescent compounds were obtained. XRD

patterns of Eu(+)-L(n) and the tdmpo molecule after 15 minutes grinding were shown in

Figure 2-7. The XRD patterns of Eu(+tfc)$_3$(H$_2$O)$_2$ (Eu(+)-L(0)) were observed even after

grinding (Figure 2-7, grey). In contrast, XRD patterns of Eu(+)-L(1), Eu(+)-L(2), and

Eu(+)-L(3) showed broad peaks, which was similar phenomenon to the XRD for Eu(III)

coordination glass.[16] No peaks of tdmpo molecule were observed for Eu(+)-L(1) and

Eu(+)-L(2), and little peaks of tdmpo were observed for Eu(+)-L(3). For comparison, XRD

patterns of Eu(+)_tppo(n) after 15 minutes grinding were shown in Figure 2-8. The XRD

peaks of Eu(+tfc)$_3$(H$_2$O)$_2$ and tppo molecules remained for Eu(+)_tppo(n) (n = 1, 2, 3),

which was different phenomenon observed in Figure 2-7. The results reveal that the

crystallinity of camphor Eu(III) complexes depends on the achiral phosphine oxide

molecules. The increase of emission intensity and the broad XRD patterns of the Eu(III)

complex with tdmpo indicate that the non-crystalline Eu(III) complex was established by

the existence of tdmpo molecules around Eu(III) ion. Previously, the crystal structure of

the camphor Eu(III) complex with two inner tppo ligands was reported,[5] suggesting that

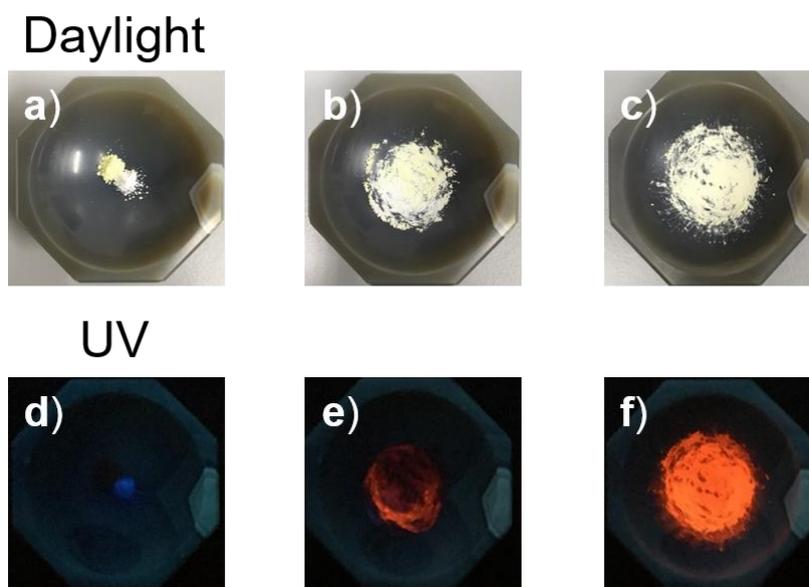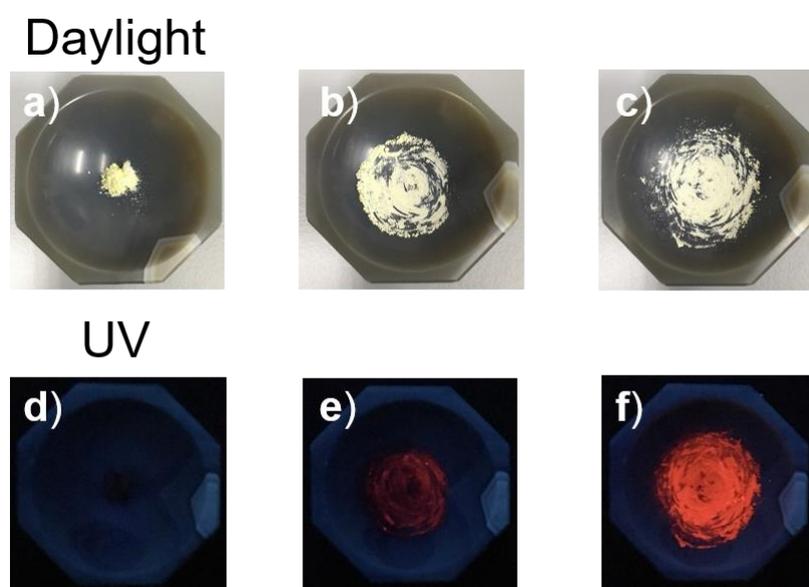the high crystalline Eu(III) complex is difficult to achieve by the grinding synthesis.

Figure 2-5. Photographs of grinding synthesis of red luminescent Eu(III) complex under daylight and UV radiation; (**a**, **d**) mixture of Eu(+tfc)$_3$(H$_2$O)$_2$ and two equivalents of tdmpo, (**b**, **e**) the ground mixture after 10 seconds, and (**c**, **f**) after 2 minutes.

Figure 2-6. Photographs of grinding synthesis of red luminescent Eu(III) complex under daylight and UV radiation; (**a**, **d**) mixture of Eu(+tfc)$_3$(H$_2$O)$_2$ and two equivalents of tppo, (**b**, **e**) the ground mixture after 10 seconds, and (**c**, **f**) after 2 minutes.
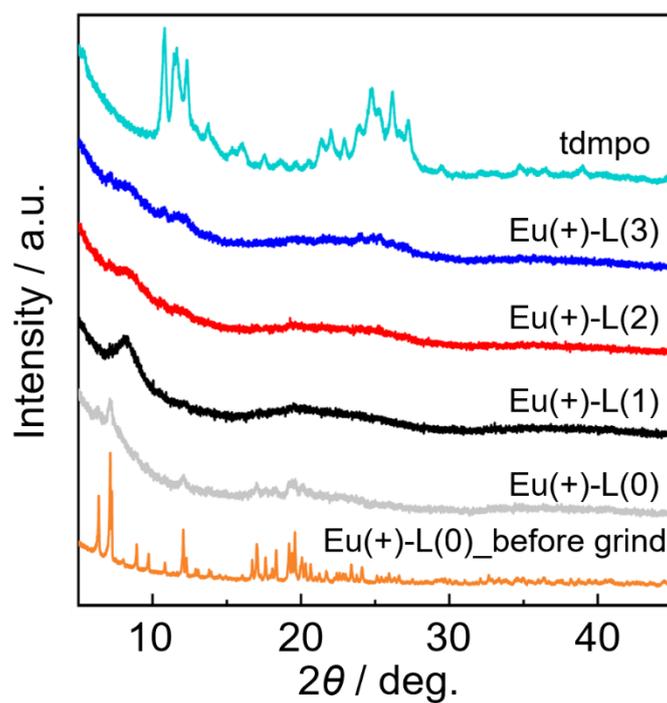
Figure 2-7. XRD spectra of Eu(+)-L(0) before grinding (orange), Eu(+)-L(0) after grinding (grey), Eu(+)-L(1) (black), Eu(+)-L(2) (red), Eu(+)-L(3) (blue), and tdmpo (sky blue). XRD patterns were measured after 15 minutes grinding of samples except for Eu(+)-L(0) before grinding.
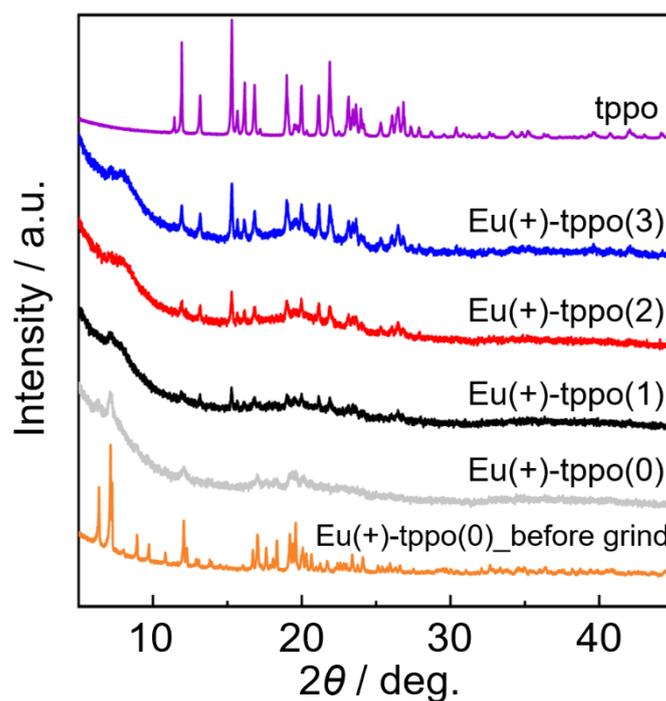
Figure 2-8. XRD spectra of Eu(+)-L(0) before grinding (orange), Eu(+)-L(0) after grinding (grey), Eu(+)_tppo(1) (black), Eu(+)_tppo(2) (red), Eu(+)_tppo(3) (blue), and tppo (purple). XRD patterns were measured after 15 minutes grinding of samples except for Eu(+)-L(0) before grinding.

To clarify the non-crystalline characteristics of the Eu(III) complex, Eu(+)-L(n) (n = 1, 2, 3) were also prepared in dichloromethane. By casting the solution to glass substrate and slowly evaporation, transparent films of Eu(+)-L(n) (n = 1, 2, 3) were obtained. The transparent films were collected as solid-like powders by scratching the films. XRD of these powders exhibited similar broad peaks (**Figure 2-9**) to those of the non-crystalline Eu(III) complexes prepared by grinding synthesis. Some sharp peaks observed for Eu(+)-L(3) (**Figure 2-9**, blue) are attributed to non-coordinated excess tdmpo molecules. DSC spectrum of Eu(+)-L2 powder is shown in **Figure 2-10**. The DSC
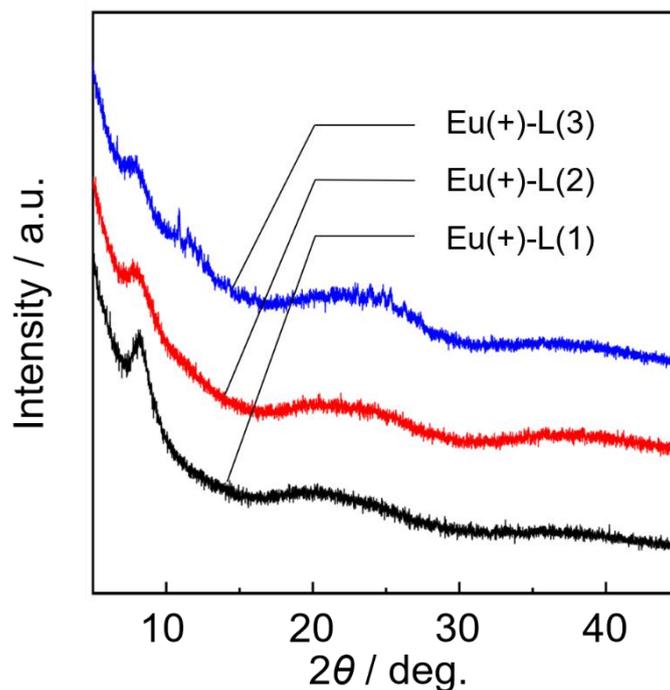
Figure 2-9. XRD spectra of Eu(+)-L(1) (black), Eu(+)-L(2) (red), and Eu(+)-L(3) (blue). The powders were collected by scratching these films.

spectrum represents the result of the second heating scan after the first treatment of heating to 180°C and cooling to r.t. An endothermic peak was observed at around 50°C, and the line after 55°C started at lower position compared with the point at 25°C. This phenomenon indicates that the Eu(III) complex has glass transition and/or melting point at around 50°C, leading to an amorphous state. In general, existence of nonplanar molecular structures, bulky substituent, and/or different conformers lowers the molecular crystallinity, leading to amorphous state.[22] The steric hindrance of camphor ligands and phosphine oxide molecules attached with methoxy groups may prevent the crystallization.
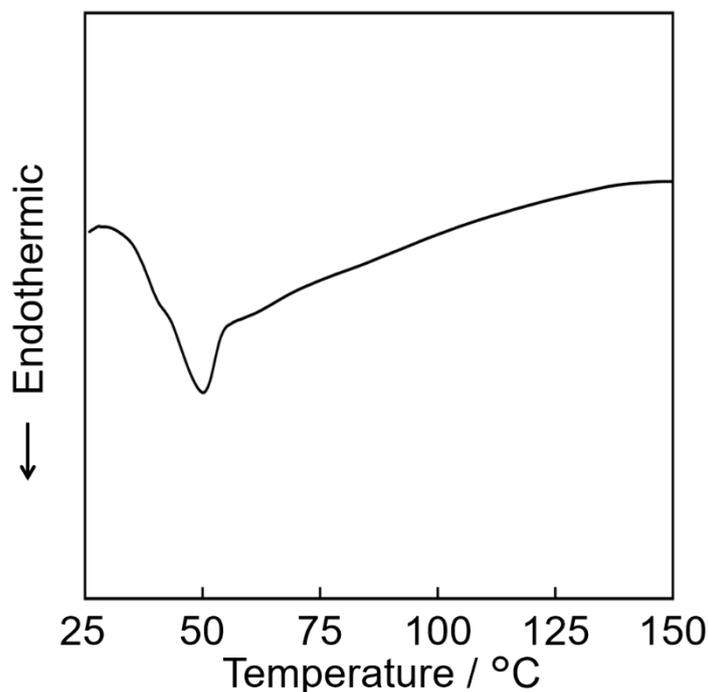
Figure 2-10. DSC spectrum of Eu(+)-L(2) after the first heating to 180°C and cooling to r.t. The powder was collected by scratching the film.

Photographs of melting experiment of Eu(+)-L(2) in the powder state, Eu(+tfc)$_3$(H$_2$O)$_2$, and tdmpo molecule on a hot plate are shown in **Figure 2-11**. The melting of Eu(+)-L(2) started below 100°C (**Figure 2-11a**), the value of which was lower than the melting points of Eu(+tfc)$_3$(H$_2$O)$_2$ (~ 200°C, **Figure 2-11b**) and tdmpo molecule (~ 230°C, **Figure 2-11c**). A non-transparent state of Eu(+)-L(2) was confirmed from 120°C to 170°C. The result implies that Eu(+)-L(2) is crystalline at the temperature, which is similar phenomenon for amorphous compounds.[23] The non-crystalline transparent film was successfully established by the combination of Eu(+tfc)$_3$(H$_2$O)$_2$ and the tdmpo molecule.

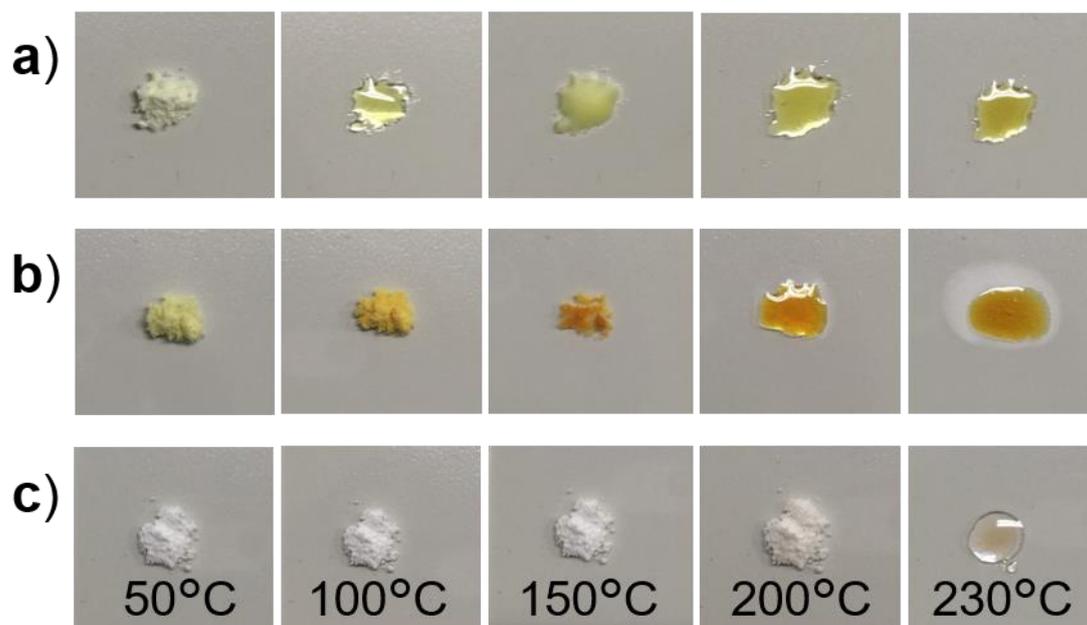**Figure 2-11.** The photographs of melting experiment of (**a**) Eu(+)-L(2) in the powder state, (**b**) Eu(+tfc)$_3$(H$_2$O)$_2$, and (**c**) tdmpo molecule on a hot plate. The temperature represents the value at the surface of the hot plate.

2.3.2 Photophysical properties of Eu(III) complexes in film state

The electronic state and the coordination geometry of Eu(III) complex are reflected by the photophysical properties of the Eu(III) complex.[24] The emission spectra of Eu(+)-L(n) (n = 1, 2, 3) in film state were shown in **Figure 2-12**. The spectra were normalized by the integrated intensities of the magnetic dipole transition ($^5D_0 \rightarrow {}^7F_1$). For these films, two peaks at 584 and 593.5 nm were observed in the $^5D_0 \rightarrow {}^7F_1$ transition. The emission bands around 612 nm are attributed to $^5D_0 \rightarrow {}^7F_2$ transition. The emission spectrum of Eu(+)-L(1) was different from that of Eu(+)-L(2) and Eu(+)-L(3), suggesting that the tdmpo molecules affect the photophysical property by existing around the Eu(III) ion in the film. The coordination geometry of Eu(III) complex with tdmpo in film state is different from that of camphor Eu(III) complex with inner two tppo in solid (Eu(+tfc)$_3$(tppo)$_2$, **Figure 2-13**). The large steric hindrance of methoxy groups may cause several conformers with weak interaction between the tdmpo molecules and the camphor Eu(III) complex, instead of their direct and tight coordination. The results imply that the weak interaction between the Eu(III) complex and tdmpo is useful for making the luminescent non-crystalline film.

For more information about the coordination structure, time-resolved emission profiles were measured. The emission lifetimes were estimated using triple exponential functions (**Table 2-1**), which supported the existence of several metastable formations in the film due to the low crystallinity. The ratio of longer lifetime τ_1 component was increased by adding the amount of tdmpo molecules. The emission decay phenomenon of Eu(+)-L(2) was similar to that of Eu(+)-L(3). The emission quantum efficiencies (Φ_L) of the films were shown in **Table 2-1**. The Φ_L of the film was gradually enhanced by increasing the amount of tdmpo molecules. The Φ_L of Eu(+)-L(3) was more than ten

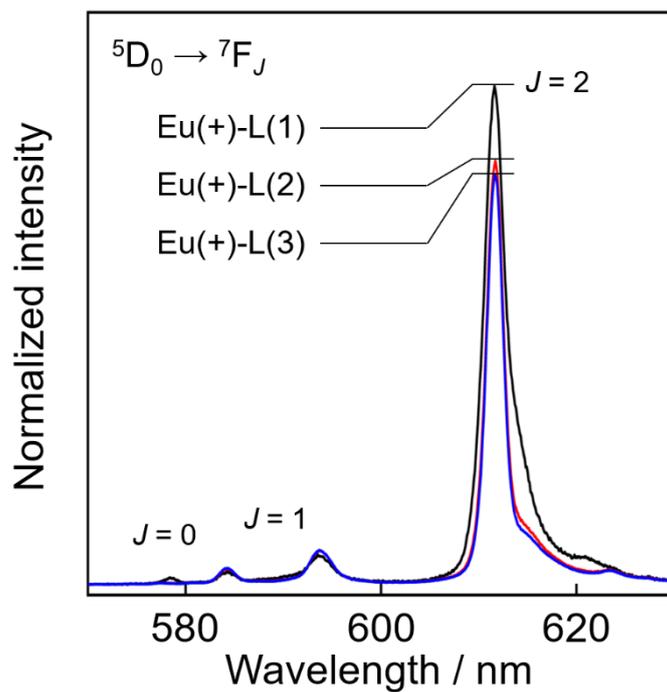**Figure 2-12.** The emission spectra of Eu(+)-L(1) (black), Eu(+)-L(2) (red), and Eu(+)-L(3) (blue) in film state, excited at 350 nm.
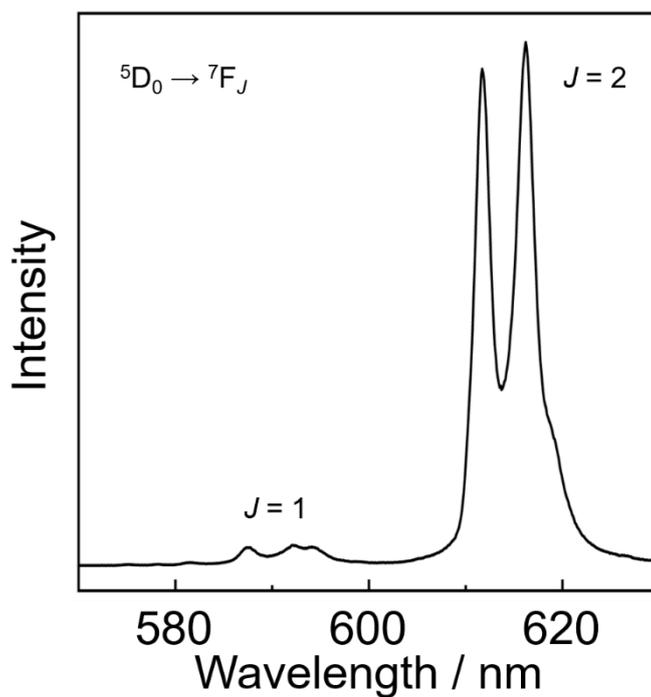

Figure 2-13. The emission spectrum of $Eu(+tfc)_3(tppo)_2$ excited at 350 nm in powder.

Table 2-1. Photophysical properties of Eu(+)-L(*n*) (*n* = 1, 2, 3) in film state.[a]

	τ_1 [ms]	τ_2 [ms]	τ_3 [ms]	Φ_{total} [%]	g_{CPL}
Eu(+)-L(1)	0.71	0.25	0.10	1	-1.2
	(35%)	(49%)	(16%)		
Eu(+)-L(2)	0.74	0.37	0.14	8	-1.5
	(60%)	(34%)	(6%)		
Eu(+)-L(3)	0.76	0.41	0.16	11	-1.5
	(61%)	(34%)	(5%)		

[a] Emission decay curves were analyzed by multi-exponential curve fittings [$I(t) = \sum A_i \exp(-t/\tau_i)$]. The percent of each component denotes $100 \times A_i\tau_i / \sum A_i\tau_i$.

times as large as that of the previously reported Cs(I)-Eu(III) complex (Φ_{total} ~ 1%) with the large g_{CPL} value (-1.45) in solution.[3]

The CPL spectra and calculated g_{CPL} values of Eu(+)-L(*n*) (*n* = 1, 2, 3) in film state were shown in **Figure 2-14** and **Table 2-1**, respectively. The large CPL signals were observed in the $^5D_0 \rightarrow {}^7F_1$ transition. The CPL spectrum of Eu(+)-L(2) at 594 nm (g_{CPL} ~ -1.5) was larger than that of Eu(+)-L(1) (g_{CPL} ~ -1.2). The CPL spectrum of Eu(+)-L(3) (g_{CPL} ~ -1.5) was similar to that of Eu(+)-L(2), the value of which was different from the small g_{CPL} value (g_{CPL} = +0.09) of Eu(+tfc)$_3$(tppo)$_2$ in solid.[8] The film did not change the CPL spectra by 90 degrees rotation of the film, indicating the films are isotropic. Although the exact g_{CPL} value could not be estimated in the experimental condition due to the experimental errors, the observed g_{CPL} value was as large as the previously reported maximum g_{CPL} value (g_{CPL} = -1.45) for Cs(I)-Eu(III) complex.[3] The result implies

that the weak interaction between the camphor Eu(III) complex and phosphine oxide molecule triggers the formation of film state with high CPL performance and large emission quantum efficiency.
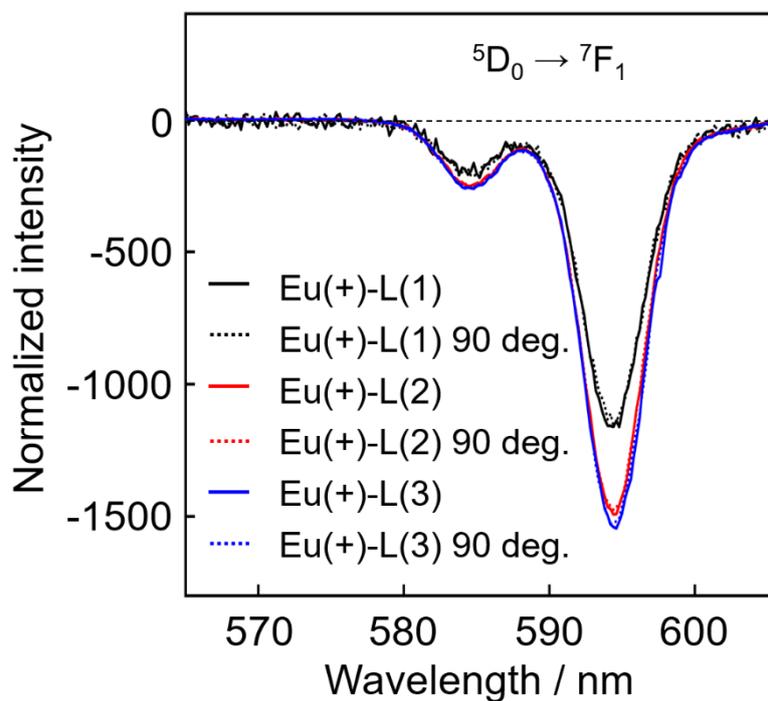

Figure 2-14. The CPL spectra of Eu(+)-L(1) (black), Eu(+)-L(2) (red), and Eu(+)-L(3) (blue) in film state, excited at 350 nm.

3.3.3   Application to CPL materials

Transparent films of Eu(+)-L(2) and the enantiomer (Eu(-)-L(2)) were prepared for the application to a simple model of CPL security ink. The experimental setup of CPL determination is shown in **Figure 2-15a**. In the setup, the emission of the film is detected through a bandpass filter (594 nm), a rotatable $\lambda/4$ plate with an angle controller, and a linear polarizer. The left- or right-handed circularly polarized light can be observed separately by controlling the angle of $\lambda/4$ plate in a 90-degree interval. Two pairs of Eu(+)-L(2) and Eu(-)-L(2) samples were prepared (**Figure 2-15b**), and the emission of these samples were detected through the filters. Photographs of the emission related to (i) left and right, (ii) left, and (iii) right circularly polarized light from the samples were shown in **Figure 2-15c**. The emission of these samples just through bandpass filter were observed brightly (photograph (i)). In contrast, the emission intensities of Eu(+)-L(2) and Eu(-)-L(2) were explicitly different after passing through the $\lambda/4$ plate and the linear polarizer depending on the rotational angle of $\lambda/4$ plate (photographs (ii) and (iii)). The difference in emission intensity is easily visible to the naked eye, which is potentially applicable to security ink. This is the first report that the CPL intensity of the luminescent film of Eu(III) complex is detectable notably and easily with simple setup of CPL determination.
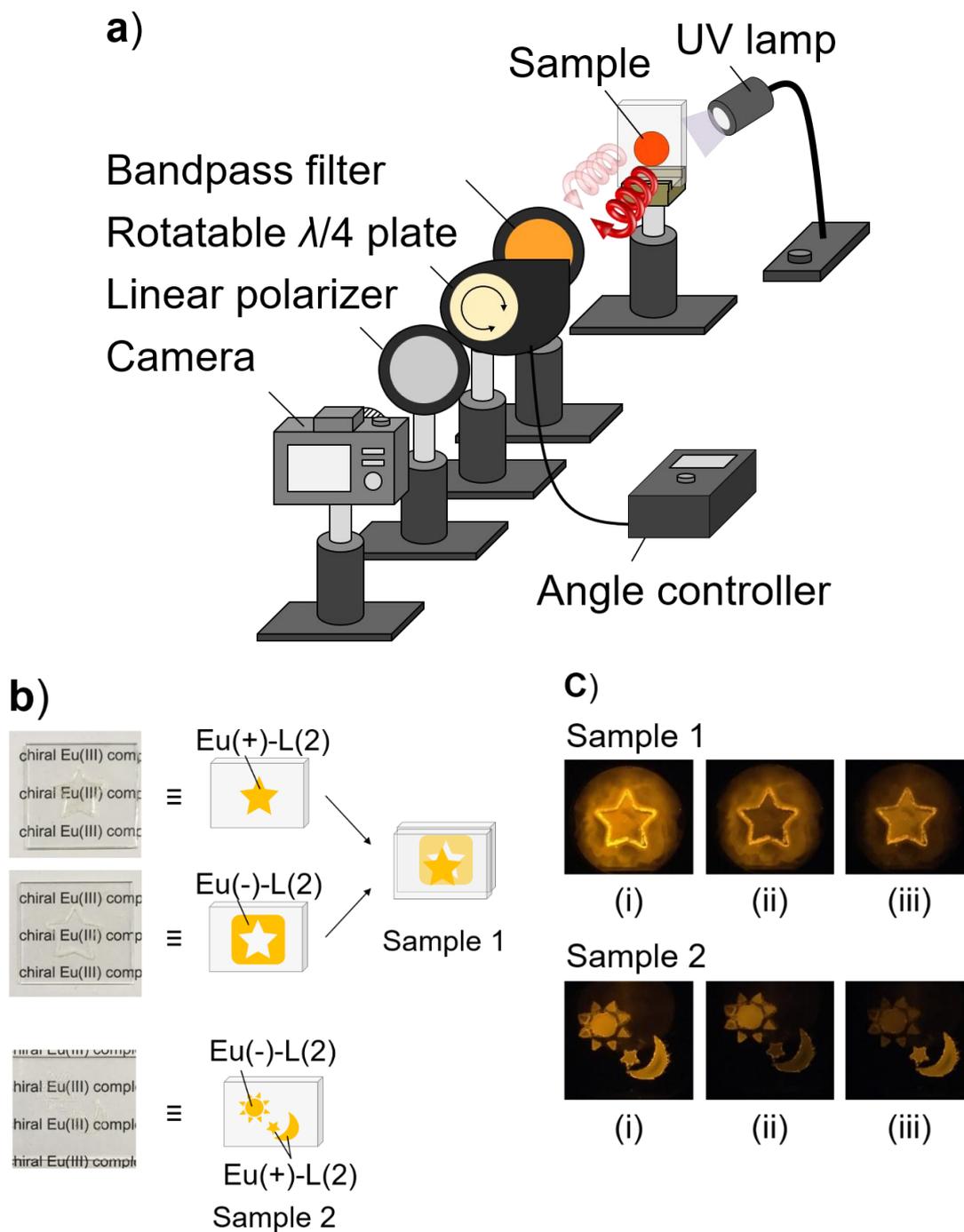
a)

UV lamp

Sample

Bandpass filter

Rotatable λ/4 plate

Linear polarizer

Camera

Angle controller

b)

chiral Eu(III) comp
chiral Eu(III) comp
chiral Eu(III) comp

≡ Eu(+)-L(2)

chiral Eu(III) comp
chiral Eu(III) comp
chiral Eu(III) comp

≡ Eu(-)-L(2)

Sample 1

chiral Eu(III) compl
hiral Eu(III) compl
hiral Eu(III) compl
hiral Eu(III) compl

≡ Eu(-)-L(2)
Eu(+)-L(2)
Sample 2

c)

Sample 1

(i)   (ii)   (iii)

Sample 2

(i)   (ii)   (iii)

Figure 2-15. (**a**) The simple setup for CPL detection. (**b**) Photographs and images of the films of Eu(+)-L(2) and Eu(-)-L(2) prepared on glasses. (**c**) Photographs of the emission related to (i) left and right, (ii) left, or (iii) right circularly polarized light from the samples.

2.4   Conclusions

Red luminescent non-crystalline chiral Eu(III) complex was successfully prepared by co-grinding of camphor Eu(III) complex and achiral phosphine oxide molecule without any solvents. The camphor Eu(III) complex was also obtained by general solution synthesis as a transparent film. The Eu(III) complex in film state exhibited extra-large CPL performance (g_{CPL} = -1.5) and high emission efficiency (Φ_L = 11%) by tuning the amount of phosphine oxide molecules. The g_{CPL} value is as large as previously reported maximum g_{CPL} value of chiral Eu(III) complex. Furthermore, the Φ_L was more than ten times as large as that of the Eu(III) complex with the maximum g_{CPL} value. The high performances were attributed to the weak interaction between the camphor Eu(III) complex and bulky phosphine oxide molecule. The film was applied to a simple model of CPL security ink. The difference in CPL intensity of the film was easily detected to the naked eye with simple setup of CPL determination, which is potentially applicable to security ink. The results provide a novel strategy for designing the Eu(III) complex with large CPL performance and high emission intensity, leading to a new application for CPL materials such as security ink, bioimaging, and 3D display.

2.5   References

[1]   F. Zinna, L. Di Bari, *Chirality* **2015**, *27*, 1–13.

[2]   J. L. Lunkley, D. Shirotani, K. Yamanari, S. Kaizaki, G. Muller, *Inorg. Chem.* **2011**, *50*, 12724–12732.

[3]   J. Kumar, B. Marydasan, T. Nakashima, T. Kawai, J. Yuasa, *Chem. Commun.* **2016**, *52*, 9885–9888.

[4]   J. Yuasa, H. Ueno, T. Kawai, *Chem. Eur. J.* **2014**, *20*, 8621–8627.

[5]   T. Harada, Y. Nakano, M. Fujiki, M. Naito, T. Kawai, Y. Hasegawa, *Inorg. Chem.* **2009**, *48*, 11242–11250.

[6]   T. Harada, H. Tsumatori, K. Nishiyama, J. Yuasa, Y. Hasegawa, T. Kawai, *Inorg. Chem.* **2012**, *51*, 6476–6485.

[7]   F. Zinna, U. Giovanella, L. Di Bari, *Adv. Mater.* **2015**, *27*, 1791–1795.

[8]   Y. Hasegawa, Y. Miura, Y. Kitagawa, S. Wada, T. Nakanishi, K. Fushimi, T. Seki, H. Ito, T. Iwasa, T. Taketsugu, M. Gon, K. Tanaka, Y. Chujo, S. Hattori, M. Karasawa, K. Ishii, *Chem. Commun.* **2018**, *54*, 10695–10697.

[9]   S. J. Dengale, H. Grohganz, T. Rades, K. Löbmann, *Adv. Drug Deliv. Rev.* **2016**, *100*, 116–125.

[10]   R. Laitinen, K. Löbmann, C. J. Strachan, H. Grohganz, T. Rades, *Int. J. Pharm.* **2013**, *453*, 65–79.

[11]   B. C. Hancock, G. Zografi, *J. Pharm. Sci.* **1997**, *86*, 1–12.

[12]   Y. Hu, K. Gniado, A. Erxleben, P. McArdle, *Cryst. Growth Des.* **2014**, *14*, 803–813.

[13]   S. Yamamura, H. Gotoh, Y. Sakamoto, Y. Momose, *Int. J. Pharm.* **2002**, *241*, 213–221.

[14]   K. Löbmann, C. Strachan, H. Grohganz, T. Rades, O. Korhonen, R. Laitinen, *Eur. J. Pharm. Biopharm.* **2012**, *81*, 159–169.

[15]   M. R. Robinson, M. B. O'Regan, G. C. Bazan, *Chem. Commun.* **2000**, *3*, 1645–1646.

[16]   Y. Hirai, T. Nakanishi, Y. Kitagawa, K. Fushimi, T. Seki, H. Ito, H. Fueno, K. Tanaka, T. Satoh, Y. Hasegawa, *Inorg. Chem.* **2015**, *54*, 4364–4370.

[17]   Y. Hirai, P. P. F. Da Rosa, T. Nakanishi, Y. Kitagawa, K. Fushimi, Y. Hasegawa, *Bull. Chem. Soc. Jpn.* **2017**, *90*, 322–326.

[18]   H. Ohara, A. Kobayashi, M. Kato, *Chem. Lett.* **2014**, *43*, 1324–1326.

[19]   H. Ohara, A. Kobayashi, M. Kato, *Dalton Trans.* **2014**, *43*, 17317–17323.

[20]   P. Liang, A. Kobayashi, W. M. C. Sameera, M. Yoshida, M. Kato, *Inorg. Chem.* **2018**, *57*, 5929–5938.

[21]   D. Yang, Z. Li, L. He, Y. Deng, Y. Wang, *RSC Adv.* **2017**, *7*, 14314–14320.

[22]   Y. Shirota, *J. Mater. Chem.* **2005**, *15*, 75–93.

[23]   M. Allesø, N. Chieng, S. Rehder, J. Rantanen, T. Rades, J. Aaltonen, *J. Control. Release* **2009**, *136*, 45–53.

[24]   K. Binnemans, *Coord. Chem. Rev.* **2015**, *295*, 1–45.

Chapter 3

Large optical activity mechanism of chiral lanthanide complexes induced by electronic state mixing

3.1 Introduction

In Chapter 2, the author revealed that the extra-large g_{CPL} value of the non-crystalline Eu(III) complex with (+)-3-(trifluoroacetyl)camphor (+tfc) and tris(2,6-dimethoxyphenyl)phosphine oxide (tdmpo) in film state. The negative and large g_{CPL} value (-1.5) was explicitly different from positive and small one (+0.09) of the camphor Eu(III) complex with triphenylphosphine oxide (tppo). Revealing a detail mechanism of the CPL phenomenon depending on the external achiral molecules should be a key to develop a chiral Eu(III) complex with high CPL performance.

The dissymmetry factor g_{CPL} is described in Equation (1.8) in Chapter 1, which is composed of electric and magnetic field components related to the electronic transition.[1] Among chiral molecules, chiral Ln(III) complexes are hopeful candidates to clarify the influence of electric and magnetic field components on optical activities for their sharp luminescence bands comprised of electric and magnetic field components of 4f-4f transitions.[2] Their components in the electronic transitions are dominated by external organic molecules around the Ln(III) ion. In particular, the magnetic dipole transition of chiral Eu(III) complex exhibits the large g_{CPL}; this is established by the effective contribution of the magnetic field component.[3–6] The optical activity signal of the lanthanide complex with chiral ligands has been evaluated by Λ- or Δ-type coordination structures.[7,8] Yuasa and Parker reported the chiroptical activity inversion of chiral Eu(III) complexes influenced by the different steric structures of achiral molecules (**Figure 3-1**),[9,10] which implied steric inversion between Λ- and Δ-type structures. Note that chiroptical activity is related to the electronic transition of the Eu(III) complex; therefore, the magnitude and sign could be also affected by the chiral electronic structure of the Eu(III) ion surrounded by external ligands.
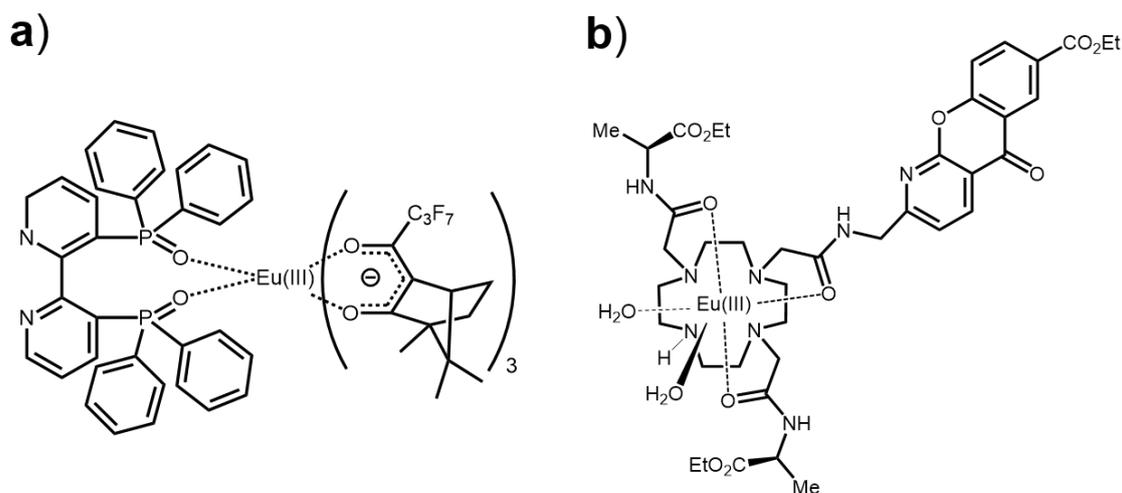
Figure 3-1. Chiral Eu(III) complexes reported by (**a**) Yuasa[9] and (**b**) Parker.[10]

In this chapter, CPL spectra of a chiral Eu(III) complex in various conditions are measured to clarify the optical activity based on the chiral electronic structure in external environments. The chiral Eu(III) complex with chiral bidentate +tfc and achiral monodentate tppo was synthesized. The Eu(III) complex [Eu(+tfc)$_3$(tppo)$_2$] (Δ-type structure as determined by X-ray single-crystal analysis) shows a large g_{CPL} (-0.47) in acetone-d$_6$.[11] The chiral electronic structure of the Eu(III) complex in solution was adjusted by additional achiral tppo and acetone molecules (**Figure 3-2**). The coordination and electronic structures in liquid media were characterized using ^{1}H NMR, photoluminescence, and emission lifetime measurements. The chiroptical activities of the Eu(III) complex under external environments were evaluated using CPL measurements. A mechanism for the optical activity inversion based on the chiral electronic structure of the Eu(III) complex without Λ- or Δ-type structure change is described spectroscopically and theoretically, for the first time.
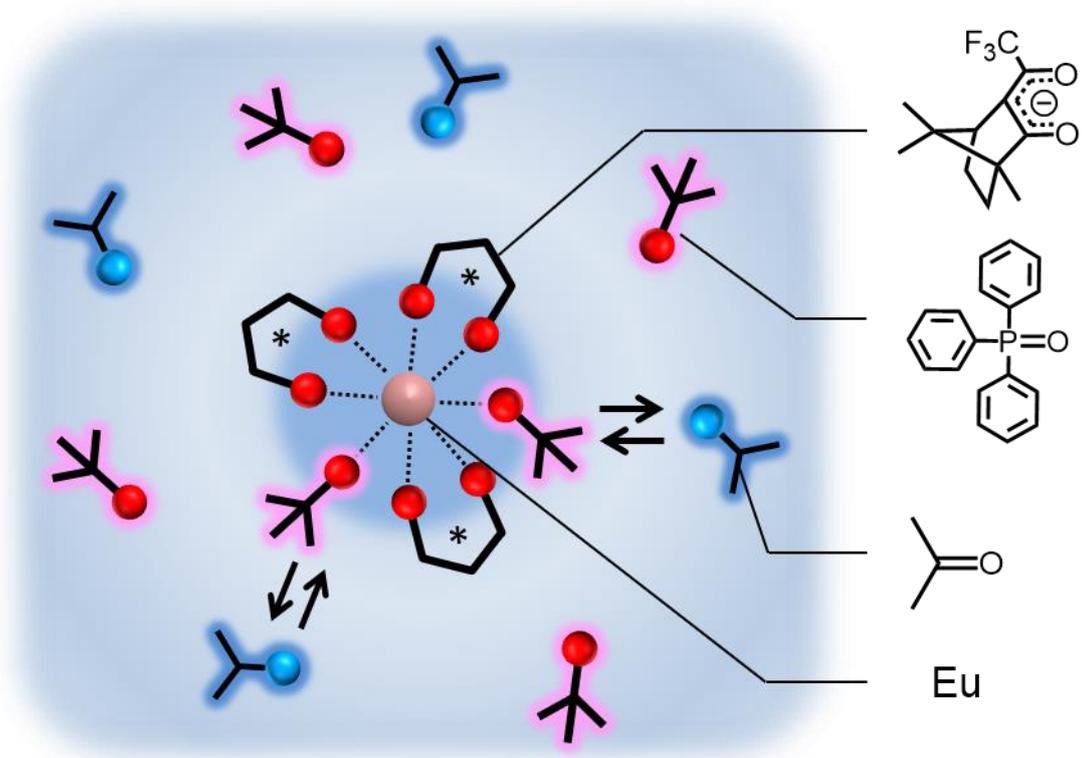
Figure 3-2. Schematic images of the coordination structures of the Eu(III) complex depending on external achiral molecules around the Eu(III) ion in solution.

3.2   Methods

Materials

Europium(III) acetate *n*-hydrate, acetone-d$_6$ (99.9%), acetone (spectroscopic grade), toluene (spectroscopic grade), dimethyl sulfoxide (spectroscopic grade), and 28% ammonia solution were purchased from Wako Pure Chemical Industries Ltd. (+)-3-(trifluoroacetyl)camphor and (-)-3-(trifluoroacetyl)camphor were purchased from Sigma-Aldrich Co. Triphenylphosphine oxide was purchased from Tokyo Chemical Industry Co., Ltd. All other chemicals and solvents were of reagent grade and were used without further purification.

Apparatus

Elemental analyses were performed on an Exeter Analytical CE440. Proton nuclear magnetic resonance (^{1}H NMR) spectra were recorded in acetone-d$_6$ on an auto-NMR JEOL ECS 400 MHz; Acetone (δ_H = 2.05 ppm) was used as an internal reference. Emission spectra and emission lifetimes were measured using a Horiba/Jobin-Yvon FluoroLog-3 spectrofluorometer. CPL spectra were measured using a JASCO CPL-200 spectrofluoropolarimeter.

Synthesis of Tris(3-trifluoroacetyl-(+)-camphorato)europium(III) bis(triphenylphosphine oxide) ([Eu(+tfc)$_3$(tppo)$_2$])[11]

Europium(III) acetate *n*-hydrate (0.36 g) was dissolved in distilled water (150 mL), and a few drops of 28 wt% ammonia solution were added. (+)-3-triflouroacetyl camphor (+tfc, 0.50 g, 2.0 mmol) in methanol (20 mL) was added to the solution, and the mixture was stirred for 3 h at room temperature. The obtained powder was washed with

distilled water, and the powder was dried in vacuo (0.42 g). The powder (0.19 g) and triphenylphosphine oxide (tppo, 0.11 g, 0.40 mmol) were dissolved in methanol (20 mL) and refluxed for 3 h. The reaction solution was evaporated using a rotary evaporator. The obtained powder was recrystallized from a hot acetonitrile solution and gave yellow crystals. Yield: 47%. Elemental analysis: Calculated for $C_{72}H_{72}EuF_9O_8P_2$: C, 59.63%, H, 5.00%. Found: C, 59.54%, H, 4.92%.
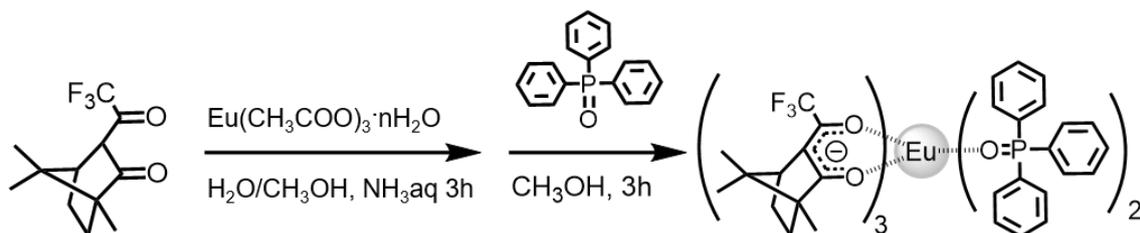
Scheme 3-1. Synthesis of Eu(+tfc)$_3$(tppo)$_2$.

Synthesis of Tris(3-trifluoroacetyl-(-)-camphorato)europium(III) bis(triphenylphosphine oxide) ([Eu(-tfc)$_3$(tppo)$_2$])

[Eu(-tfc)$_3$(tppo)$_2$] was prepared using the same method for [Eu(+tfc)$_3$(tppo)$_2$], starting from (-)-3-triflouroacetyl camphor, yielding yellow powder. Yield: 64%. Elemental analysis: Calculated for $C_{72}H_{72}EuF_9O_8P_2$: C, 59.63%, H, 5.00%. Found: C, 59.49%, H, 4.94%.

3.3　Results and discussion

3.3.1　Coordination structures of Eu(III) complexes in solution

X-ray crystallography measurements indicated that the coordination structure of the Eu(III) complex in the solid is an eight-coordinated Δ-type structure composed of three chiral +tfc and two tppo ligands.[11] To evaluate the conformation of [Eu(+tfc)$_3$(tppo)$_2$] (**Eu(+)**) in acetone, ^{1}H NMR spectra with additional n equivalents ($n =$ 0, 8, 28, 48, and 98 relative to **Eu(+)**) of tppo molecules, namely **Eu(+)**-Exn, were acquired (**Figure 3-3** and **Table 3-1**). In the low-magnetic-field side, protons of tppo molecules in **Eu(+)**-Ex0 show broad peaks in **Figure 3-3** (black; A). The line-broadening and chemical shifts originate from the exchange reaction and paramagnetic effect on the metal complex.[12,13] The paramagnetic effect of the Eu(III) ion generally induces little broadening (bandwidth; nearly 10 Hz).[13] Therefore, the large broadening of tppo signals in the experiment (**Figure 3-3**, black; A, bandwidth; nearly 300 Hz) is mainly caused by their exchange reaction in acetone-d$_6$. The lower-magnetic-field shift in **Eu(+)**-Ex0

Table 3-1. ^{1}H NMR peaks of **Eu(+)**-Exn in acetone-d$_6$ (**Eu(+)**; 1 × 10^{-3} M).

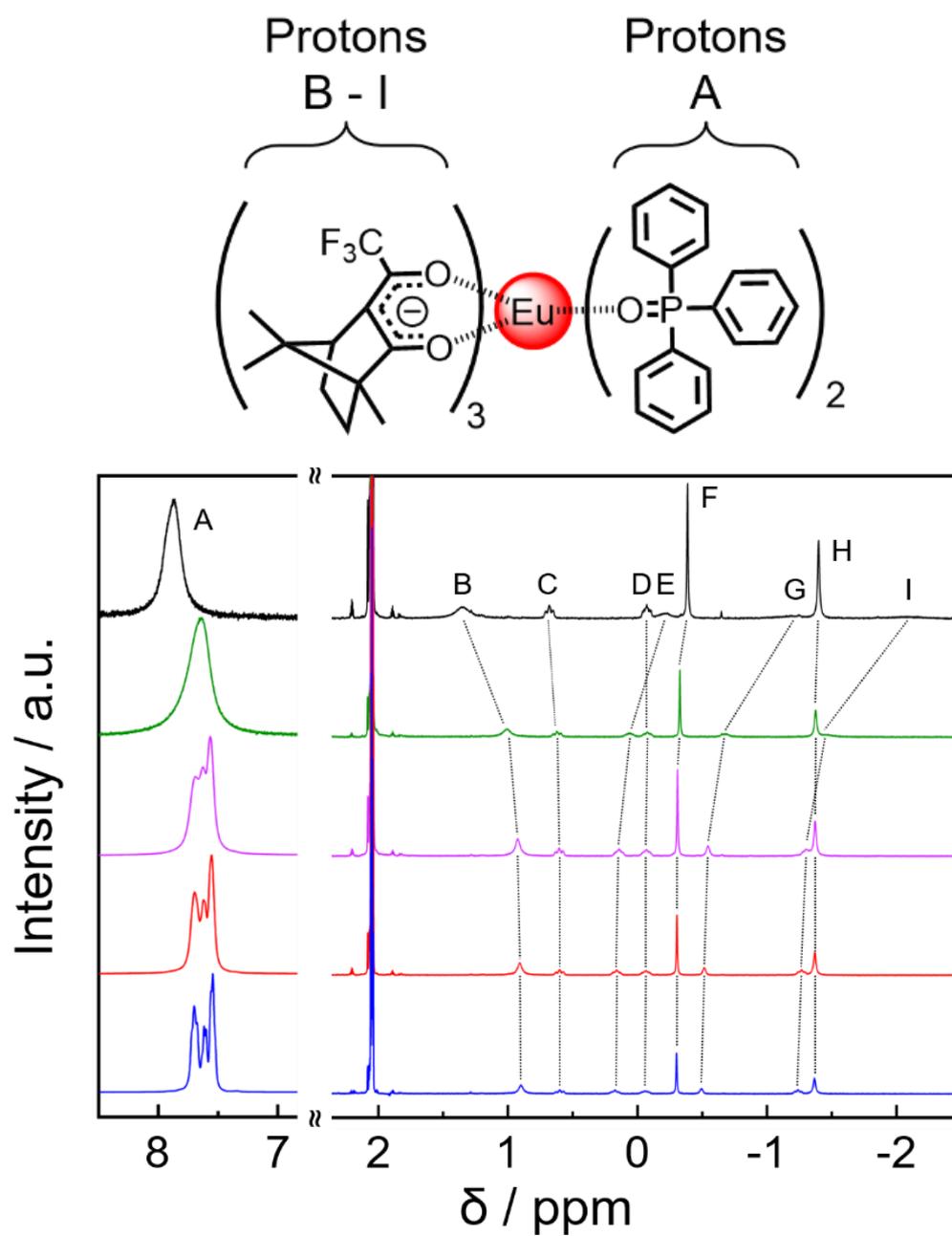|	A [ppm]	B [ppm]	C [ppm]	D [ppm]	E [ppm]	F [ppm]	G [ppm]	H [ppm]	I [ppm]
Eu(+)-Ex0	7.87	1.35	0.68	-0.07	-0.21	-0.39	-1.19	-1.40	-2.09
Eu(+)-Ex8	7.64	1.01	0.62	-0.08	0.06	-0.33	-0.68	-1.38	-1.45
Eu(+)-Ex28	7.63	0.92	0.60	-0.07	0.14	-0.31	-0.54	-1.37	-1.30
Eu(+)-Ex48	7.62	0.91	0.60	-0.07	0.16	-0.30	-0.52	-1.37	-1.27
Eu(+)-Ex98	7.62	0.90	0.60	-0.06	0.17	-0.30	-0.49	-1.37	-1.24

Figure 3-3. ^{1}H NMR spectra of **Eu(+)**-Ex0 (black), **Eu(+)**-Ex8 (green), **Eu(+)**-Ex28 (purple), **Eu(+)**-Ex48 (red), and **Eu(+)**-Ex98 (blue) in acetone-d_6 (**Eu(+)**; 1 × 10^{-3} M).

(**Figure 3-3**, black; A) is influenced by the direct coordination of tppo ligands with the Eu(III) ion.

NMR peaks of the chiral +tfc ligands in the Eu(III) complex were observed in the high-magnetic-field side (**Figure 3-3**, signals B - I). **Eu(+)**-Ex8 (green) provided effective chemical shifts of +tfc ligands compared with those of **Eu(+)**-Ex0 (black). Gradual shifts were also observed at the B, E, G, and I peaks of **Eu(+)**-Ex28 (purple), -Ex48 (red), and -Ex98 (blue). The effective shifts of the tppo and +tfc signals indicate that the Eu(III) complex with tppo molecules is rearranged by additional tppo molecules, resulting in the formation of several equilibrium states in acetone-d_6.

3.3.2 Luminescence properties of Eu(III) complexes

Photophysical properties of Eu(III) complexes are affected by the coordination geometry[14]. The emission spectra of **Eu(+)**-Ex0 and -Ex498 in acetone (1×10^{-3} M) are shown in **Figure 3-4** (black; **a**, and red; **b**). The Eu(III) complexes show sharp emission peaks in the region of 570-630 nm, which are attributed to the $^5D_0 \rightarrow {^7F_J}$ (J = 0, 1, and 2) transitions of Eu(III) ions. The spectra were normalized with respect to the integrated intensities of the magnetic dipole transition ($^5D_0 \rightarrow {^7F_1}$). Their spectral shapes in liquid media were different from that of [Eu(+tfc)$_3$(tppo)$_2$] in the solid state as described in chapter 2 (**Figure 2-13**). The emission spectra for the $^5D_0 \rightarrow {^7F_1}$ and $^5D_0 \rightarrow {^7F_2}$ transitions were also changed in response to the concentration of the tppo molecules in solution. In particular, the $^5D_0 \rightarrow {^7F_1}$ transition band is composed of three Stark sublevels under the electric field (crystal field). **Eu(+)**-Ex0 showed three peaks at 584.5, 587.8, and 593.5 nm in the $^5D_0 \rightarrow {^7F_1}$ transition (**Figure 3-4** inset, black; **a**), whereas **Eu(+)**-Ex498 showed two peaks at around 587.8 and 592.8 nm (**Figure 3-4** inset, red; **b**). The $^5D_0 \rightarrow {^7F_1}$ transition of **Eu(+)**-Ex0 at a lower concentration (1×10^{-5} M, **Figure 3-4**, blue; **c**) also showed three peaks at 584.2, 587.5, and 593.5 nm, which are similar to that of Eu(+)-Ex0 at a higher concentration. The small peak at 587.5 nm can be attributed to the $^5D_1 \rightarrow {^7F_3}$ transition, which is sometimes observed in the same energy region as the $^5D_0 \rightarrow {^7F_1}$ transition[14]. The emission bands at around 612 nm are attributed to hypersensitive electric dipole transitions ($^5D_0 \rightarrow {^7F_2}$), which are strongly dependent on the local symmetry of the Eu(III) ion. The change of spectral shape is influenced by the rearrangement of coordination geometries of the Eu(III) complex depending on additional tppo molecules. In case of the non-coordinating toluene solution, the emission spectra of **Eu(+)**-Ex0 and -Ex48 were similar in shape to that of **Eu(+)**-Ex498 in acetone,
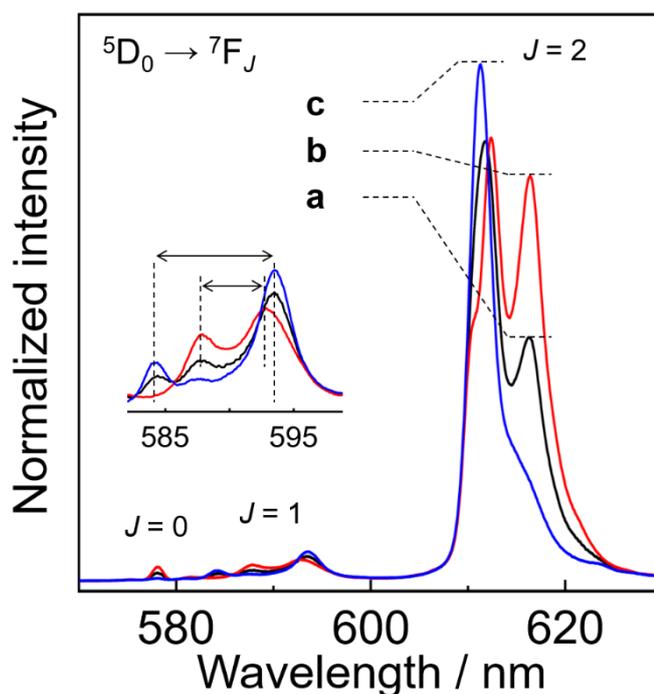
Figure 3-4. Photoluminescence spectra of (**a**) **Eu(+)**-Ex0 (1×10^{-3} M, black), (**b**) **Eu(+)**-Ex498 (1×10^{-3} M, red), and (**c**) **Eu(+)**-Ex0 (1×10^{-5} M, blue) excited at 350 nm in acetone.

irrespective of the amount of additional tppo molecules (**Figure 3-5**). It is proposed that the inner coordination structure of **Eu(+)**-Ex498 in acetone is composed of one Eu(III) ion, three +tfc ligands, and two tppo ligands.

The time-resolved emission profiles of **Eu(+)**-Ex0 and -Ex498 in acetone (1×10^{-3} M) were measured to clarify their coordination structures. The emission lifetimes were estimated using triple (for **Eu(+)**-Ex0) or double (for **Eu(+)**-Ex498) exponential functions to analyze several conformations in solution (**Figures 3-6a** and **3-6b**). The estimated emission lifetimes are summarized in **Table 3-2**. For **Eu(+)**-Ex0, the emission lifetimes (τ_1, τ_2, and τ_3) and their ratios were calculated to be 0.27 ms (50%), 0.09 ms
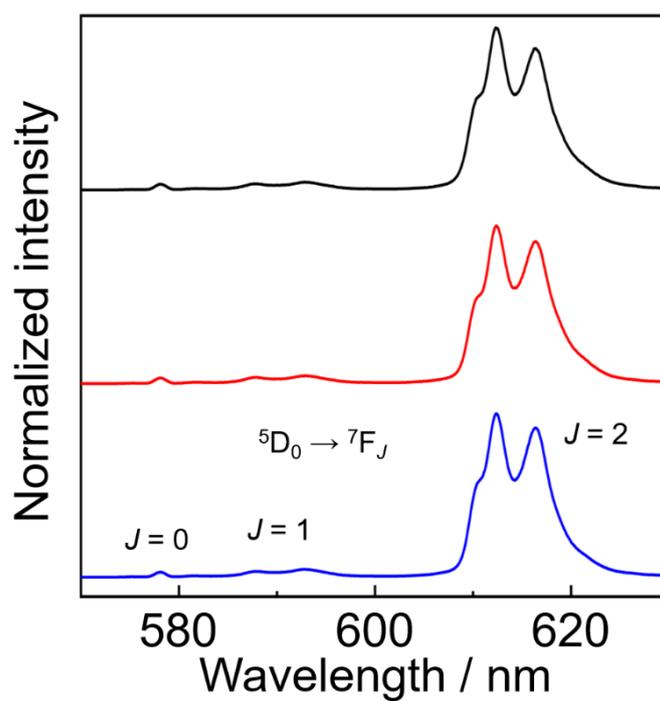
Figure 3-5. Photoluminescence spectra of **Eu(+)**-Ex0 (1×10^{-3} M, black) in toluene, **Eu(+)**-Ex48 (1×10^{-3} M, red) in toluene, and **Eu(+)**-Ex498 (1×10^{-3} M, blue) in acetone, excited at 350 nm.
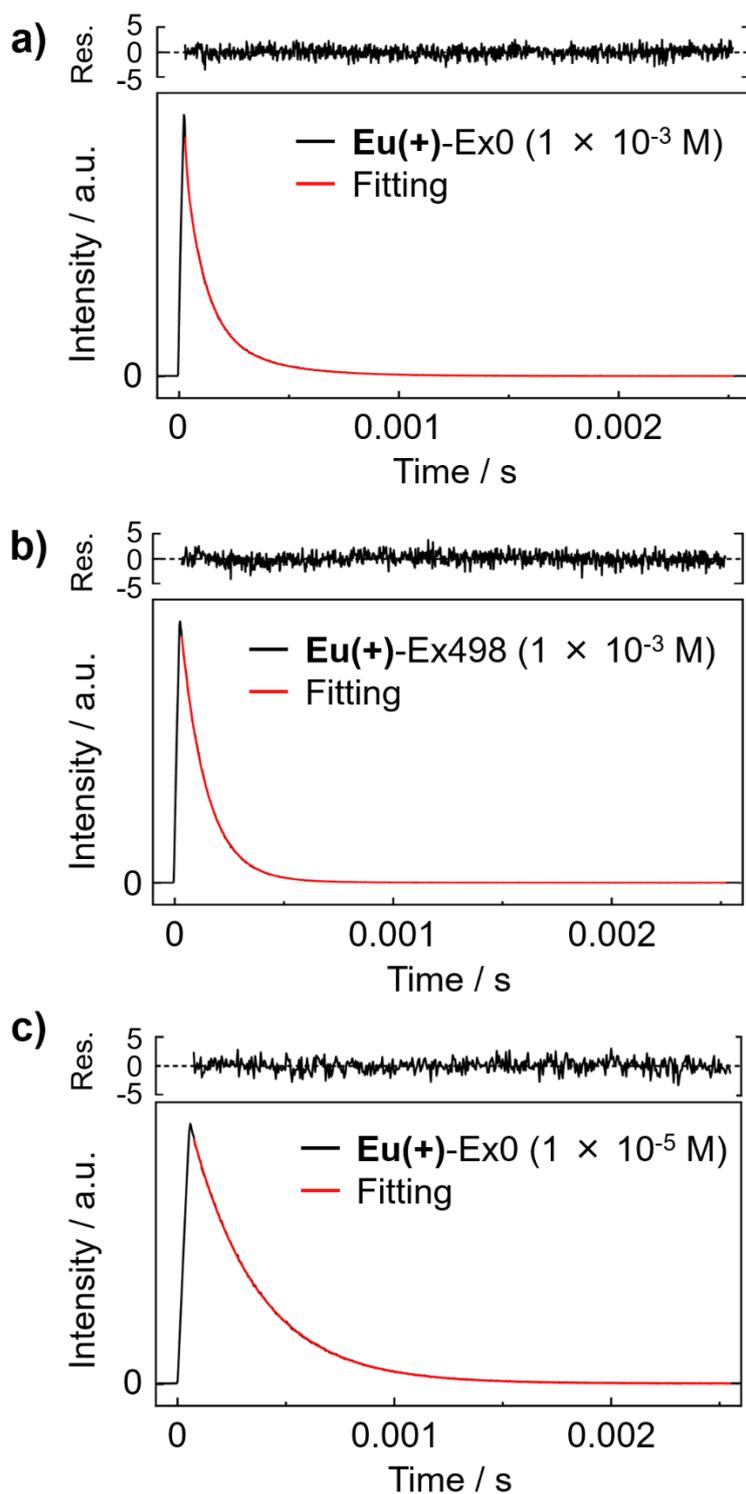
Figure 3-6. Emission decay profiles, fittings, and residuals (Res.) of (**a**) **Eu(+)**-Ex0 (1 ×

10^{-3} M), (**b**) **Eu(+)**-Ex498 (1 × 10^{-3} M), and (**c**) **Eu(+)**-Ex0 (1 × 10^{-5} M) at 612 nm excited

at 356 nm in acetone.

Table 3-2. Luminescence properties of **Eu(+)**-Ex*n* excited at 356 nm in acetone.[a]

	Concentration [M]	τ_1 [ms]	τ_2 [ms]	τ_3 [ms]	g_{CPL}
Eu(+)-Ex0	1×10^{-3}	0.27 (50%)	0.09 (49%)	0.01 (1%)	-0.44
Eu(+)-Ex498	1×10^{-3}	0.37 (3%)	0.12 (97%)	-	+0.013
Eu(+)-Ex0	1×10^{-5}	0.31 (100%)	-	-	-1.0

[a] Emission decay curves were analyzed by multi-exponential curve fittings [$I(t) = \sum A_i \exp(-t/\tau_i)$]. The percent of each component denotes $100 \times A_i\tau_i / \sum A_i\tau_i$.

(49%), and 0.01 ms (1%), respectively. The longer component τ_1 in higher concentration (1 × 10⁻³ M, 0.27 ms) was similar to the single component τ_1 in lower concentration (1 × 10⁻⁵ M, 0.31 ms, **Figure 3-6c**). The τ_1 component is considered to be the Eu(III) complex with coordinating acetone molecules (**Figure 3-7**, A). The τ_1 and τ_2 component ratios decreased and increased, respectively, with increasing amount of tppo molecules. The main τ_2 value of **Eu(+)**-Ex498 was found to be 0.12 ms (97%). The lifetime τ_2 in acetone was similar to the single-lifetime component in toluene (**Table 3-3**), indicating that the Eu(III) ion is attached with three +tfc and two tppo ligands (**Figure 3-7**, B). The results revealed that the two types of steric structures with τ_1 and τ_2 components were reorganized in response to the external tppo and acetone molecules.
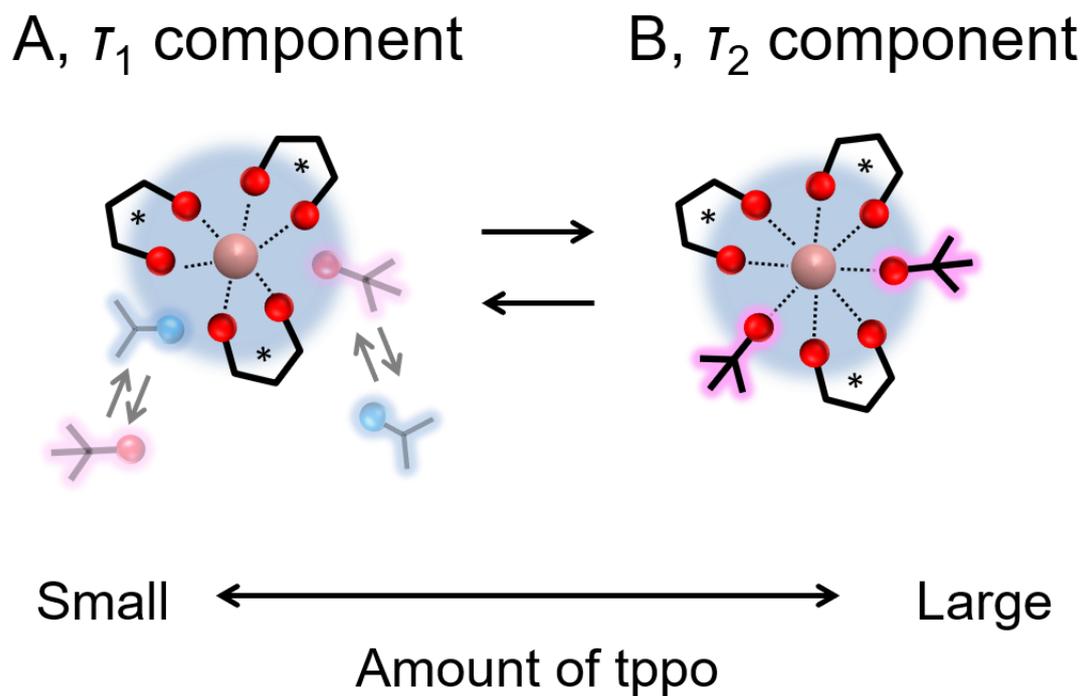
A, τ_1 component   B, τ_2 component

Small ⟷ Large

Amount of tppo

Figure 3-7. The coordination image of the τ_1 and τ_2 components of the Eu(III) complex in acetone.

Table 3-3. Luminescence properties of **Eu(+)**-Ex*n* excited at 356 nm in toluene.

	Concentration [M]	τ [ms]
Eu(+)-Ex0	1×10^{-3}	0.09 (100%)
Eu(+)-Ex48	1×10^{-3}	0.13 (100%)

3.3.3 Chiroptical properties of Eu(III) complexes

The CPL spectra and the dissymmetry factors of **Eu(+)**-Ex0 and -Ex498 are shown in **Figure 3-8** and **Table 3-2**, respectively. The CPL signals for the $^5D_0 \rightarrow {}^7F_1$ transition were composed of two peaks at 583 and 594 nm. The CPL signal at 594 nm was inverted by the addition of tppo molecules. The CPL spectrum of **Eu(+)**-Ex0 (1×10^{-3} M) shows a large negative peak at 594 nm, the g_{CPL} value of which (-0.44) is similar to a previously reported g_{CPL} value (g_{CPL} = -0.47)[11] in acetone-d_6 (1×10^{-3} M). The CPL spectrum of **Eu(+)**-Ex498 (1×10^{-3} M, excess amount of tppo) exhibits a small positive peak (g_{CPL} = +0.013). The enantiomer [Eu(-tfc)$_3$(tppo)$_2$] also exhibits CPL sign inversion at the transition (**Figure 3-9**). The CPL intensity of **Eu(+)**-Ex0 in lower concentration (1×10^{-5} M, g_{CPL} = -1.0) is much larger than that in higher concentration (1×10^{-3} M, g_{CPL} =
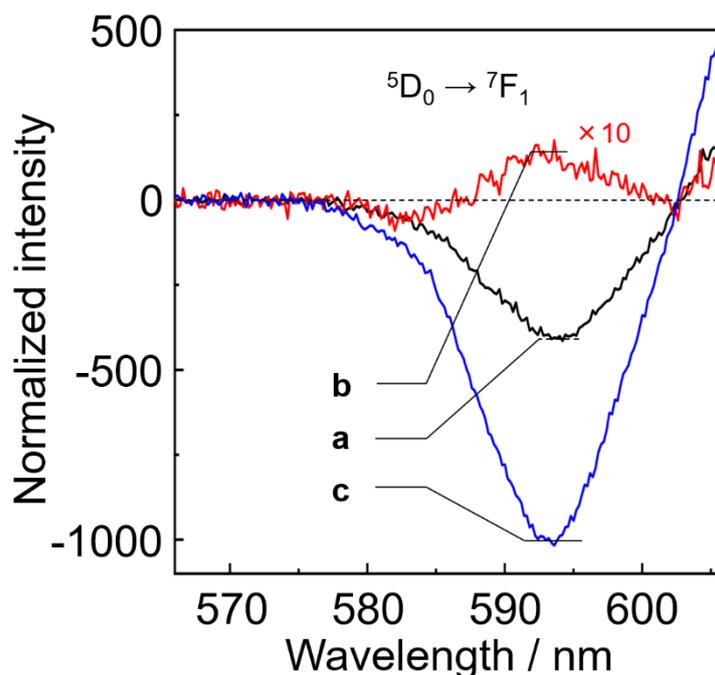
Figure 3-8. CPL spectra of (**a**) **Eu(+)**-Ex0 (1×10^{-3} M, black), (**b**) **Eu(+)**-Ex498 (1×10^{-3} M, red), and (**c**) **Eu(+)**-Ex0 (1×10^{-5} M, blue) excited at 350 nm in acetone.

74

-0.44). In contrast, the CPL signals of **Eu(+)**-Ex0 and -Ex498 at around 583 nm in the

$^5D_0 \rightarrow {}^7F_1$ transition exhibit negative CPL signals in these conditions. The CPL sign

inversion behaviors depending on the external environments are summarized in **Figure**

3-10. Law and Dai reported similar CPL sign inversion phenomena of chiral Eu(III)

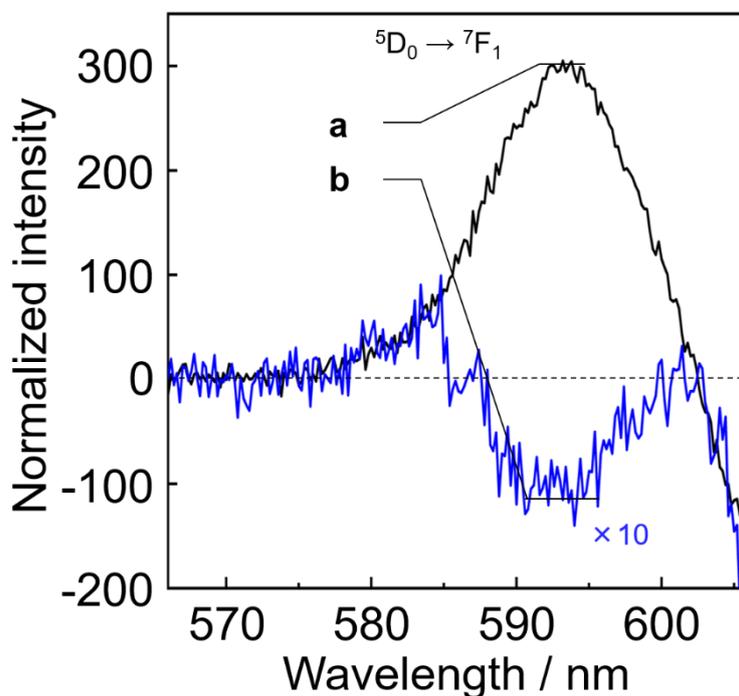complexes in the $^5D_0 \rightarrow {}^7F_1$ transition depending on solvents (**Figure 3-10b**).[15]

Figure 3-9. CPL spectra of [Eu(-tfc)$_3$(tppo)$_2$] (**a**) without tppo addition (1 × 10^{-3} M, black)

and (**b**) with additional 498 equivalents of tppo (1 × 10^{-3} M, blue) in acetone, excited at

350 nm.
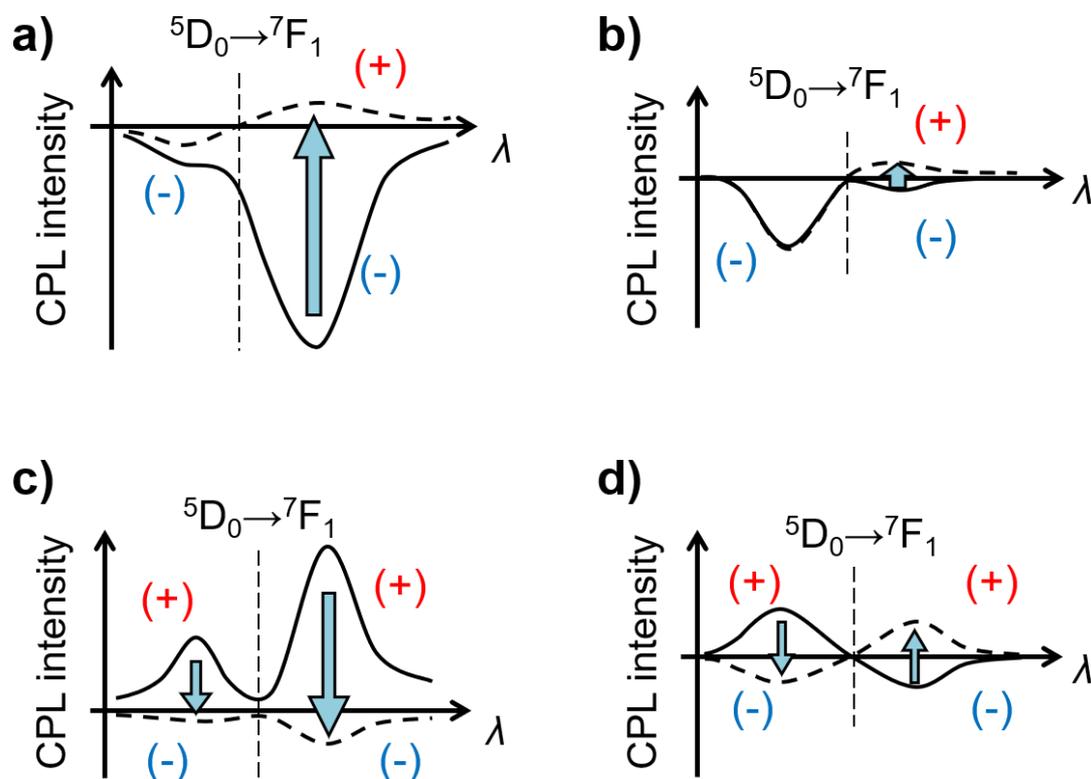
Figure 3-10. Graphical images of CPL sign inversion in the $^5D_0 \rightarrow {}^7F_1$ transition reported by (**a**) this experiment, (**b**) Law,[15] (**c**) Yuasa,[9] and (**d**) Parker.[10]

Considering the presence of τ_1 and τ_2 components in the emission lifetime measurements, the observed CPL spectra of **Eu(+)**-Ex0 and -Ex498 in acetone (1×10^{-3} M) were attributed to several equilibrium states of the Eu(III) complex in acetone. As a Eu(III) complex without tppo molecules, $Eu(+tfc)_3(H_2O)_2$ in acetone (1×10^{-3} M) were prepared. The emission and CPL spectra of $Eu(+tfc)_3(H_2O)_2$ in acetone (1×10^{-3} M) are shown in **Figures 3-11a** and **3-11b**, respectively. The emission spectral shape agreed with that of **Eu(+)**-Ex0 in lower concentration (1×10^{-5} M, **Figure 3-4**, blue; **c**), indicating their coordination structures are similar to the τ_1 component. The time-resolved emission

profile exhibited single exponential decay for the Eu(+tfc)$_3$(H$_2$O)$_2$ in acetone (1 × 10^{-3} M).

The Eu(+tfc)$_3$(H$_2$O)$_2$ exhibited negatively large CPL signal (g_{CPL} = -0.97) in the ^{5}D$_0$ → ^{7}F$_1$ transition as well as that of **Eu(+)**-Ex0 in lower concentration (1 × 10^{-5} M, g_{CPL} = -1.0, **Figure 3-4**, blue; **c**). These results support that the large g_{CPL} value of τ_1 component is related to acetone molecules around the Eu(III) ion. The small positive g_{CPL} of **Eu(+)**-Ex498 is related to the τ_2 component of the eight-coordinated Eu(III) complex with two inner tppo ligands. This was supported by the similar positive g_{CPL} (+0.036) in toluene **Figure 3-12**).
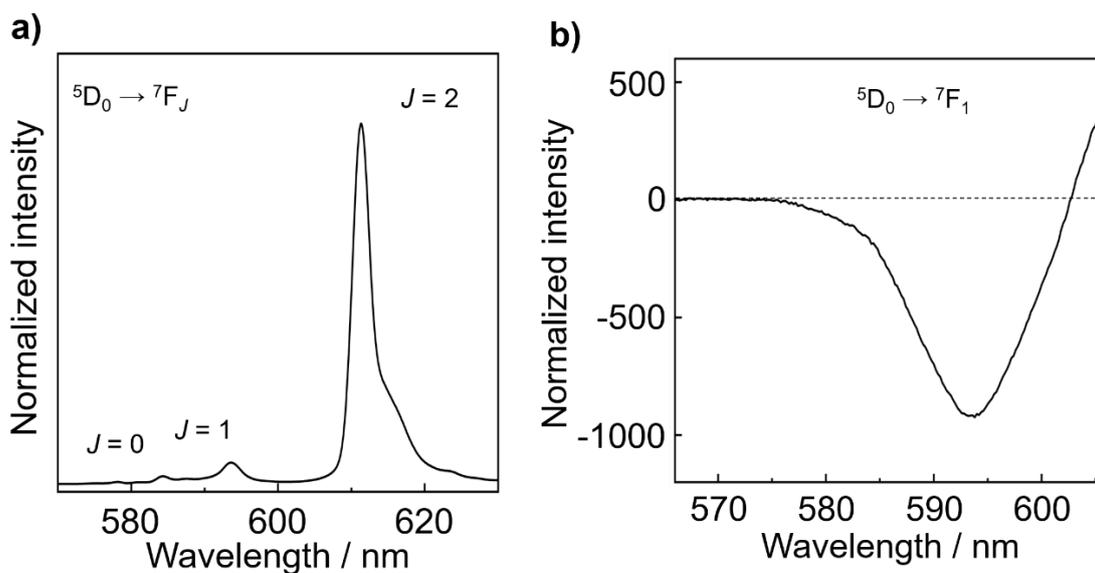
Figure 3-11. (**a**) Photoluminescence and (**b**) CPL spectra of Eu(+tfc)$_3$(H$_2$O)$_2$ in acetone (1 × 10^{-3} M), excited at 350 nm.
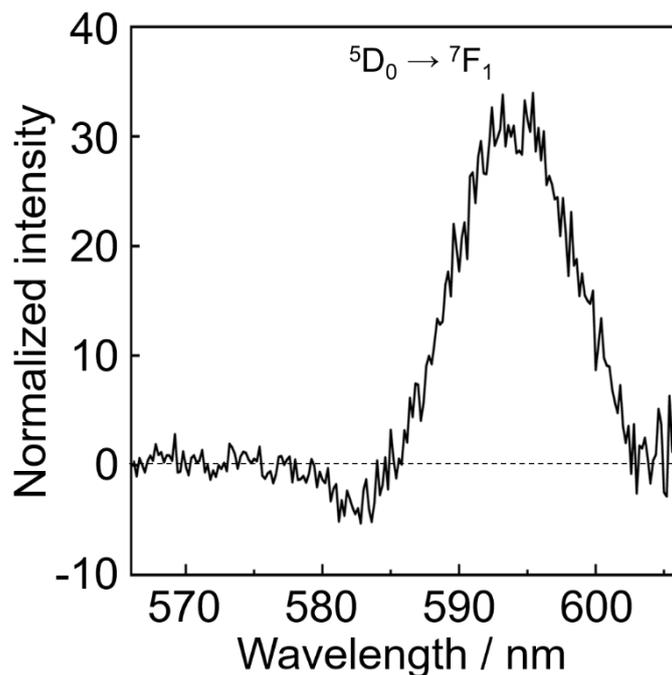
Figure 3-12. CPL spectrum of **Eu(+)**-Ex48 (1×10^{-3} M) in toluene, excited at 350 nm.

The dissymmetry factor g_{CPL} in Equation (1.8) is deformed as follows,[4]

$$
g_{\mathrm{CPL}} = 4 \cdot \frac{|\vec{\mu}||\vec{m}| \cos \theta}{|\vec{\mu}|^2 + |\vec{m}|^2} = 4 \cdot \frac{\left(\frac{|\vec{\mu}|}{|\vec{m}|}\right) \cos \theta}{\left(\frac{|\vec{\mu}|}{|\vec{m}|}\right)^2 + 1}, \tag{3.1}
$$

where θ is the angle between $\vec{\mu}$ and $\vec{m}$. When $\vec{\mu} = \vec{m}$ ($\theta = 0°$), Equation (3.1) provides the largest g_{CPL} value (**Figure 3-13a**). In the region $|\vec{\mu}|/|\vec{m}| < 1$ (**Figures 3-13a** and **3-13b**, orange regions), the Eu(III) complex with a large $|\vec{\mu}|$ provides a large g_{CPL} value. In general, the $|\vec{m}|$ value in the $^5D_0 \rightarrow {}^7F_1$ transition is larger than the $|\vec{\mu}|$ value ($|\vec{\mu}|/|\vec{m}| < 1$).[16] The intensity of $|\vec{\mu}|$ in the $^5D_0 \rightarrow {}^7F_1$ transition depends on the crystal field around the Eu(III) ion.[17,18] The $^7F_1$ energy level of the Eu(III) ion in a typical eight-coordinate structure (C_{4v} or D_{2d}) splits into two Stark sublevels (**Figure 3-13b**).[14]
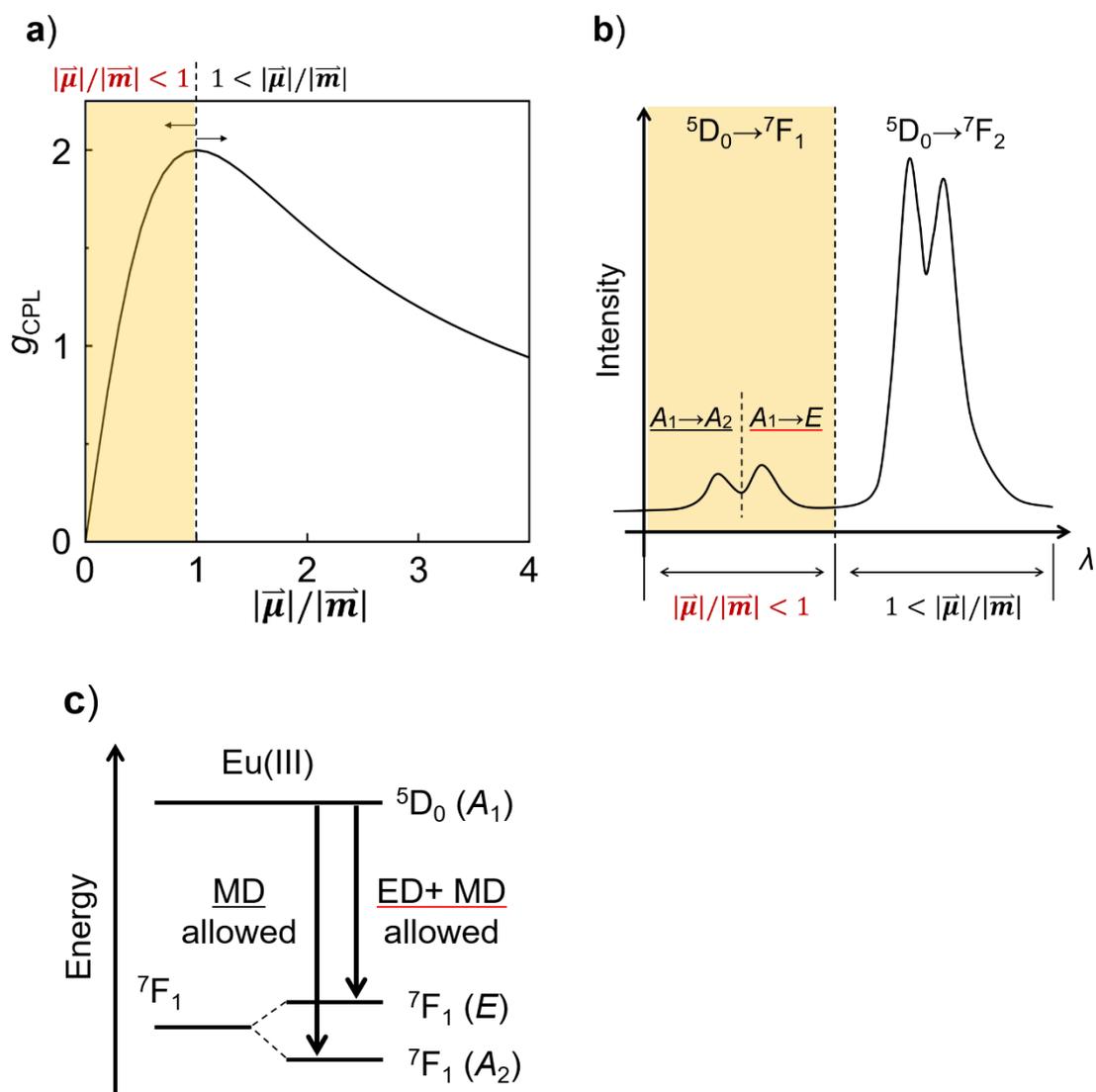
a)

b)

c)

Figure 3-13. (**a**) A simulated g_{CPL} curve against $|\vec{\mu}|/|\vec{m}|$ ratio in Equation (2.1) with $\theta = 0°$. (**b**) An attribution of photoluminescence spectrum and (**c**) an energy diagram in the $^5D_0 \rightarrow {}^7F_1$ transition of Eu(III) complex (C_{4v} or D_{2d}) based on the electronic structure and group theory.

The two bands at 583 and 594 nm in the CPL spectra are assigned to the $A_1 \rightarrow A_2$ and $A_1 \rightarrow E$ transitions,[18] respectively, in **Figures 3-13b** and **3-13c**. The observed CPL signal in the $A_1 \rightarrow E$ transition was inverted from minus to plus, while that in the $A_1 \rightarrow A_2$ transition retained the minus sign. In C_{4v} or D_{2d} symmetry, the direct product A_2 (= $A_1 \times A_2$) is expressed in terms of the electric dipole (ED) forbidden and magnetic dipole (MD) allowed transitions (R_z) on the character table in group theory (**Figure 3-13c**, **Tables 3-4** and **3-5**). On the other hand, the direct product E (= $A_1 \times E$) produces ED and MD allowed transitions ((x, y) ; (R_x, R_y), **Figure 3-13c**, **Tables 3-4** and **3-5**). The CPL sign at 583 nm (ED forbidden $A_1 \rightarrow A_2$ transition) reflects the intrinsic Λ- or Δ-type structure, because of insensitive electronic state mixing. Considering the same CPL sign at 583 nm of the r_1 and r_2 components, the structure-type (Λ or Δ) with the r_1 component is the same as that with the r_2 component in our experiments. In contrast, the CPL sign in the ED and MD allowed $A_1 \rightarrow E$ transition is sensitive to electronic state mixing even for the same chiral structure-type (Λ or Δ). The effective sign inversion and drastic intensity change of the CPL signal in the $A_1 \rightarrow E$ transition should be caused by the change of $\vec{\mu}$ based on electronic state mixing.

In the $^5D_0 \rightarrow {}^7F_1$ transition, $\vec{\mu}$ is mainly altered by the J-mixing of $^7F_2$ or $^7F_3$ sublevels into $^7F_1$.[14,19] In the photoluminescence spectra, the Stark splitting energy of the r_1 component (270 cm^{-1}, **Figure 3-4** inset, blue; **c**) was larger than that of the r_2 component (160 cm^{-1}, **Figure 3-4** inset, red; **b**). The large Stark splitting energy suggests the large J-mixing in the $A_1 \rightarrow E$ transition of the r_1 component.[19] The J-mixing increases the $|\vec{\mu}|$ value at the ED allowed $A_1 \rightarrow E$ transition relative to that at the ED forbidden $A_1 \rightarrow A_2$ transition, which is consistent with relatively large emission intensity at the $A_1 \rightarrow E$ transition (593.5 nm) of the r_1 component (**Figure 3-4** inset, blue; **c**). The $|\vec{\mu}|$ increase

leads to the large g_{CPL} value in Equation (3.1).

In Chapter 2, the large g_{CPL} value (-1.5) was observed for Eu(+tfc)$_3$(H$_2$O)$_2$ with tdmpo molecules (Eu(+)-L(n), n = 2, 3) in film state (**Figure 2-14**). The emission spectral shapes of Eu(+)-L(n) (n = 2, 3) in film state were similar to the splitting of Eu(+tfc)$_3$(tppo)$_2$ in acetone (1 × 10^{-5} M), indicating that the effective J-mixing is induced for Eu(+)-L(n) (n = 2, 3).

Table 3-4. The character table for point group C_{4v}.

C_{4v}	E	$2C_4$	C_2	$2\sigma_v$	$2\sigma_d$		
A_1	1	1	1	1	1	z	$x^2 + y^2, z^2$
A_2	1	1	1	-1	-1	R_z	
B_1	1	-1	1	1	-1		$x^2 - y^2$
B_2	1	-1	1	-1	1		xy
E	2	0	-2	0	0	(x, y) ; (R_x, R_y)	(xz, yz)

Table 3-5. The character table for point group D_{2d}.

D_{2d}	E	$2S_4$	C_2	$2C_2'$	$2\sigma_d$		
A_1	1	1	1	1	1	z	$x^2 + y^2, z^2$
A_2	1	1	1	-1	-1	R_z	
B_1	1	-1	1	1	-1		$x^2 - y^2$
B_2	1	-1	1	-1	1		xy
E	2	0	-2	0	0	(x, y) ; (R_x, R_y)	(xz, yz)

An extra-large g_{CPL} (-1.3) of the Eu(III) complex was also observed in DMSO (**Figure 3-14**). The emission spectrum of **Eu(+)**-Ex0 in DMSO (1×10^{-3} M, purple) provides the same splitting shape to that of **Eu(+)**-Ex0 in acetone (1×10^{-5} M, blue), as shown in **Figure 3-15**. The result indicates that the coordination structure of **Eu(+)**-Ex0 in DMSO is similar to that of **Eu(+)**-Ex0 in acetone (1×10^{-5} M). The hypersensitive $^5D_0 \rightarrow {}^7F_2$ transition of **Eu(+)**-Ex0 in DMSO is smaller than that of **Eu(+)**-Ex0 in acetone, indicating the small contribution of 4f-5d mixing in DMSO. The CPL of **Eu(+)**-Ex0 in DMSO (g_{CPL} = -1.3, **Figure 3-14**, purple; **b**) is negatively larger in the $^5D_0 \rightarrow {}^7F_1$ transition than that in acetone (1×10^{-5} M, **Figure 3-14**, blue; **a**). These results imply that the extra-large g_{CPL} in DMSO may be attributed to the large J-mixing with small 4f-5d mixing character.

The angle θ between $\vec{\mu}$ and $\overrightarrow{m}$ of the r_1 component is larger than 90°, whereas that of the r_2 component is smaller than 90°, suggesting that the angle is established by $\vec{\mu}$ vector change due to J-mixing. The extra-large enhancement of g_{CPL} from +0.013 to -1.0 also indicates that J-mixing promotes the direction of $\vec{\mu}$ and $\overrightarrow{m}$ to antiparallel, leading to the large g_{CPL}. It was demonstrated that the CPL sign and intensity are strongly influenced by the chiral electronic structure depending on the $\vec{\mu}$ under J-mixing in the same chiral structure-type.
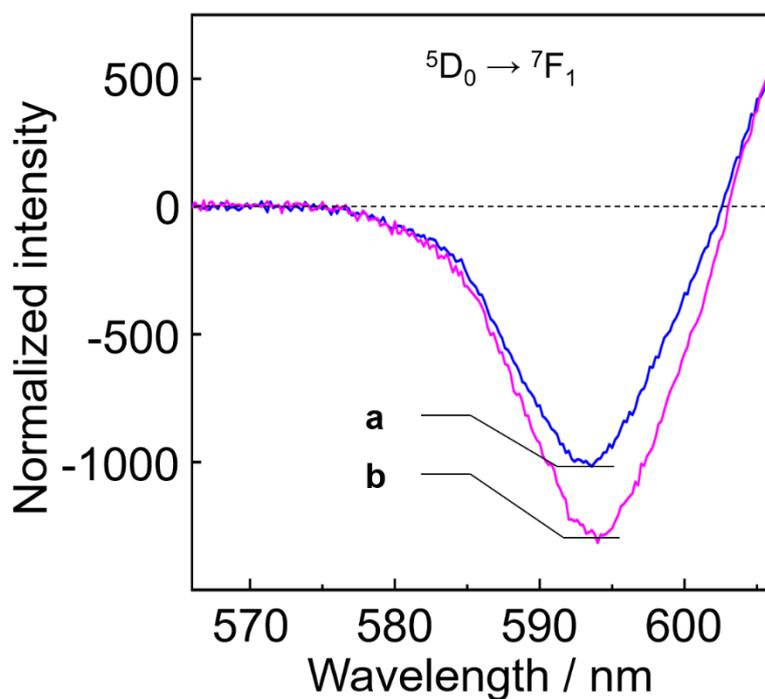
82

Figure 3-14. CPL spectra of **Eu(+)**-Ex0 (**a**) in acetone (1 × 10^{-5} M, blue) and (**b**) in DMSO (1 × 10^{-3} M, purple), excited at 350 nm.
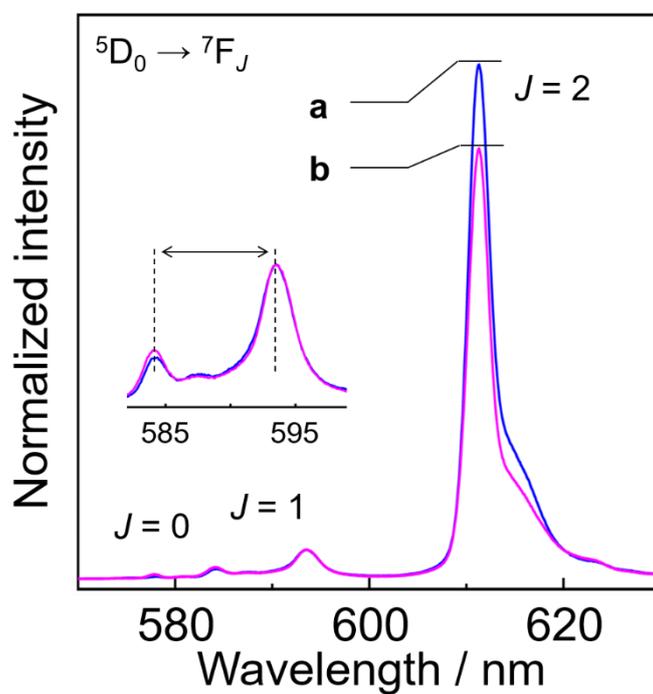

Figure 3-15. Photoluminescence spectra of (**a**) **Eu(+)**-Ex0 in acetone (1 × 10^{-5} M, blue) and (**b**) in DMSO (1 × 10^{-3} M, purple), excited at 350 nm.

3.4   Conclusions

A novel mechanism for chiroptical activity inversion based on the electronic structure of metal complexes without Λ- or Δ-type structure change was demonstrated spectroscopically and theoretically. The steric and electronic structures of the Eu(III) complex were adjusted by additional achiral tppo and coordinating acetone molecules. CPL sign inversion, which was independent of Λ- or Δ-type structure changes from the spectroscopic viewpoint, and a drastic g_{CPL} change from +0.013 to -1.0 were observed depending on the external achiral molecules around Eu(III) ion. These phenomena provide the first clarification of optical activity change associated with electronic structure rather than chiral coordination structure-type (Λ or Δ) under external environments. The CPL phenomena were attributed to the chiral electronic structure depending on the $\vec{\mu}$ under J-mixing. The results provide a novel aspect for the optical activity of metal complexes and for molecular design of chiral lanthanide complex for maximizing the g_{CPL} value.
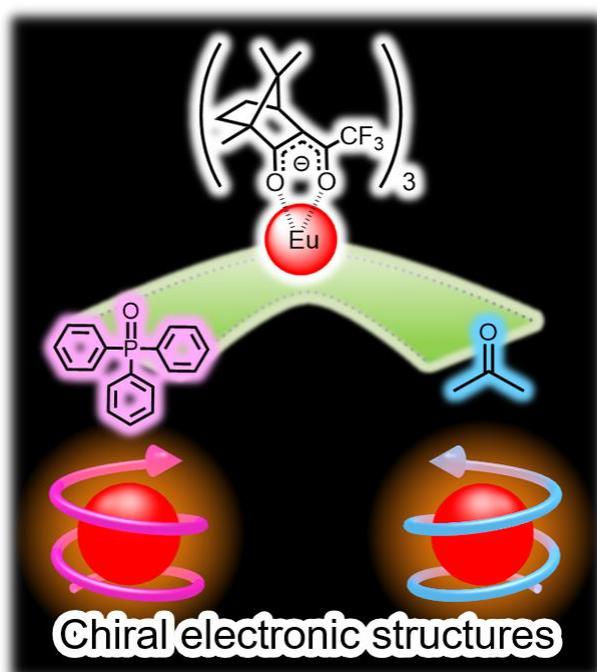
3.5 References

[1]   S. F. Mason, *Molecular Optical Activity and the Chiral Discriminations*,

        Cambridge University Press, **1982**.

[2]   J.-C. G. Bünzli, *Coord. Chem. Rev.* **2015**, *293–294*, 19–47.

[3]   F. Richardson, *Inorg. Chem.* **1980**, *19*, 2806–2812.

[4]   F. Zinna, L. Di Bari, *Chirality* **2015**, *27*, 1–13.

[5]   J. L. Lunkley, D. Shirotani, K. Yamanari, S. Kaizaki, G. Muller, *Inorg. Chem.*

        2011, *50*, 12724–12732.

[6]   J. Kumar, B. Marydasan, T. Nakashima, T. Kawai, J. Yuasa, *Chem. Commun.*

        2016, *52*, 9885–9888.

[7]   R. Carr, N. H. Evans, D. Parker, *Chem. Soc. Rev.* **2012**, *41*, 7673–7686.

[8]   Y. Kono, N. Hara, M. Shizuma, M. Fujiki, Y. Imai, *Dalton Trans.* **2017**, *46*, 5170–

        5174.

[9]   J. Yuasa, H. Ueno, T. Kawai, *Chem. Eur. J.* **2014**, *20*, 8621–8627.

[10]   D. G. Smith, R. Pal, D. Parker, *Chem. Eur. J.* **2012**, *18*, 11604–11613.

[11]   T. Harada, Y. Nakano, M. Fujiki, M. Naito, T. Kawai, Y. Hasegawa, *Inorg. Chem.*

        2009, *48*, 11242–11250.

[12]   I. R. Kleckner, M. P. Foster, *Biochim. Biophys. Acta* **2011**, *1814*, 942–968.

[13]   A. F. Cockerill, G. L. O. Davies, R. C. Harden, D. M. Rackham, *Chem. Rev.*

        1976, *73*, 553–588.

[14]   K. Binnemans, *Coord. Chem. Rev.* **2015**, *295*, 1–45.

[15]   L. Dai, W. S. Lo, I. D. Coates, R. Pal, G. L. Law, *Inorg. Chem.* **2016**, *55*, 9065–

        9070.

[16]   F. S. Richardson, M. T. Berry, M. F. Reid, *Mol. Phys.* **1986**, *58*, 929–945.

[17]   C. Görller-Walrand, L. Fluyt, A. Ceulemans, W. T. Carnall, *J. Chem. Phys.* **1991**, *95*, 3099–3106.

[18]   J. H. Forsberg, *Coord. Chem. Rev.* **1973**, *10*, 195–226.

[19]   C. G. Ma, M. G. Brik, V. Kiisk, T. Kangur, I. Sildos, *J. Alloys Compd.* **2011**, *509*, 3441–3451.

Chapter 4

Optical- and magneto-optical activities of chiral Tb(III) clusters functionalized by mixing of electronic wavefunctions

4.1 Introduction

In Chapter 3, the importance of the electronic structure of Ln(III) complex induced by the external environment was described to evaluate the chirality of Ln(III) complexes. In the system, the polarized light response based on the chirality was discussed by the contribution of the electronic state mixing. The chirality in electronic transition originates from the transition magnetic dipole moment, indicating the other photophysical properties of chiral Ln(III) complexes are influenced by the contribution of transition magnetic dipole moment. This chapter focuses on the polarized light response under the external magnetic field, that is magneto-optical activity, of chiral Tb(III) complexes.

Inorganic lanthanide compounds such as Tb(III)-doped borosilicate glasses and Tb(III) garnet ceramics exhibit large Faraday effects in the 4f-5d transition due to the large angular momentum of the 4f electron, and such materials have been used to construct optical isolators employed in optical communication systems.[1–4] In contrast to 4f-4f transitions, 4f-5d transitions are suitable for applying to these systems owing to the larger absorption coefficient and the broader bandwidth.

Recently, nonanuclear Tb(III) clusters coordinated with salicylate ligands were described for a new type of lanthanide material exhibiting a large Faraday effect (**Figure 4-1**).[5] These clusters are composed of nine Tb(III) ions bridged by ten μ-OHs and sixteen salicylic acid esters as organic ligands. The Faraday rotation angles of the clusters in the visible region are much larger than those of Tb glasses, which is expected to be useful for next-generation optical communication systems. A further unique property of these clusters was also identified, where the rotation angles were different depending on the organic ligands.
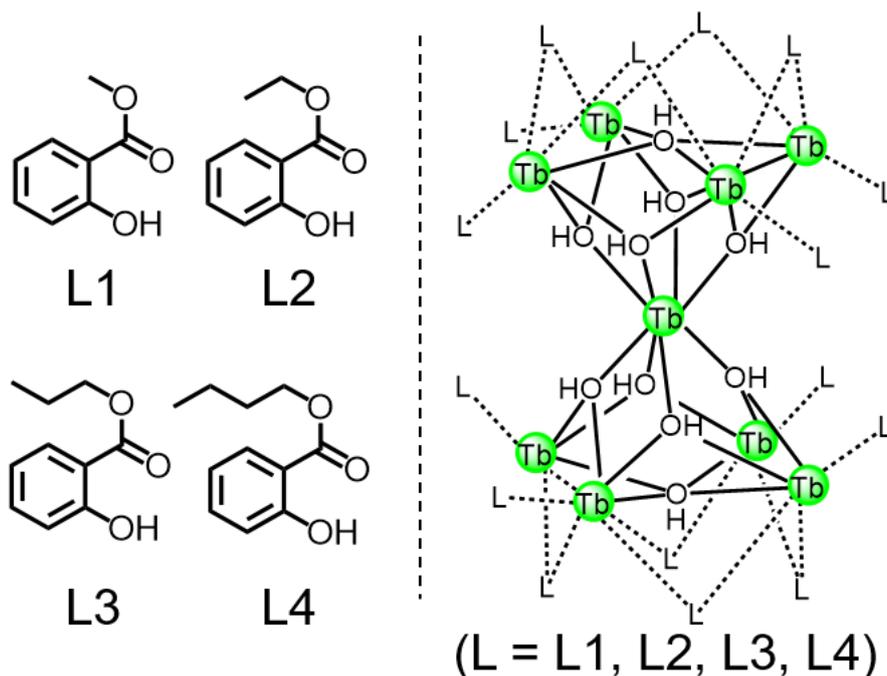
Figure 4-1. Nonanuclear Tb(III) clusters with alkyl salicylate ligands.[5]

This finding has the possibility to lead to new molecular designs for Faraday effect materials based on the type of the organic ligands.

In this chapter, chiral ligands are introduced to the Tb(III) cluster to maximize the unique characteristics of these inorganic–organic hybrid complexes. The optical activities such as CD and CPL are derived from the chirality of the complexes. Thus, their origin is markedly different from that of the Faraday effect.[6,7] As a general trend, Tb(III) complexes are classified into a group having a large g_{CPL} among the lanthanide complexes,[8] expecting the large transition magnetic dipole moments of several transitions in the Tb(III) clusters. The author introduces chiral ligands into Tb(III) clusters to investigate the effect of large transition magnetic dipole moments on the Faraday rotation. The four types of chiral Tb(III) clusters [Tb$_9$(Sal-(+)-Bor)$_{16}$(μ-OH)$_{10}$]$^+$[NO$_3$]$^-$ (Tb-

(+)-Bor: Sal-(+)-Bor = (+)-bornyl salicylate), [Tb$_9$(Sal-(-)-Bor)$_{16}$(μ-OH)$_{10}$]$^+$[NO$_3$]$^-$ (Tb-(-)-Bor: Sal-(-)-Bor = (-)-bornyl salicylate), [Tb$_9$(Sal-(R)-Bt)$_{16}$(μ-OH)$_{10}$]$^+$[NO$_3$]$^-$ (Tb-(R)-Bt: Sal-(R)-Bt = (R)-2-butyl salicylate) and [Tb$_9$(Sal-(S)-Bt)$_{16}$(μ-OH)$_{10}$]$^+$[NO$_3$]$^-$ (Tb-(S)-Bt: Sal-(S)-Bt = (S)-2-butyl salicylate) were synthesized by the complexation of Tb(NO$_3$)·6H$_2$O with chiral organic ligands in solution (**Figure 4-2**). The ligands were chosen as chiral molecules with camphor derivative part (sal-(+/-)-Bor) or with simple chiral center (sal-(R/S)-Bt). The structures and optical activities of these clusters were characterized using CD and CPL measurements. The Faraday effect measurements were also performed for Tb-(R)-Bt and Tb-(S)-Bt in methyl methacrylate polymer (PMMA) films.
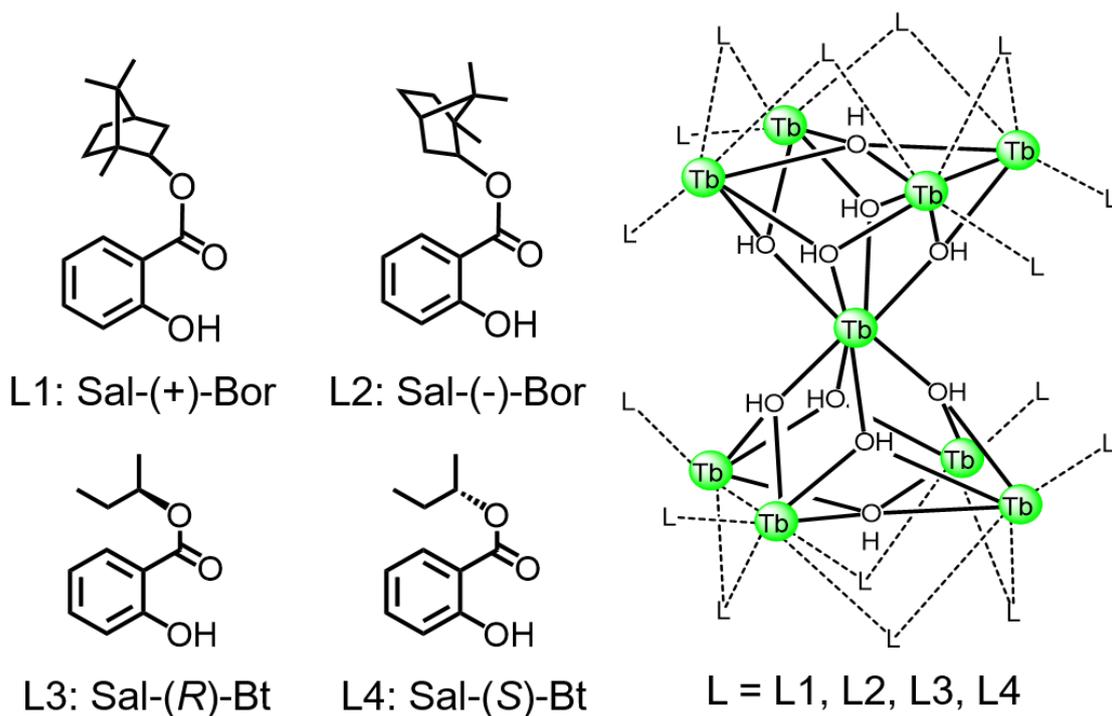
Figure 4-2. Structures of nonanuclear Tb(III) clusters with chiral ligands.

4.2 Methods

Materials

Salicylic acid ($C_6H_4(OH)COOH$), *N,N*-dimethyl-4-aminopyridine (DMAP, $C_7H_{10}N_2$), PMMA (($C_5H_8O_2)_n$, Lot PDF4279), 1,4-dioxane ($C_4H_8O_2$), CH_3OH, and chloroform ($CHCl_3$) were purchased from Wako Pure Chemical Industries, Ltd. (+)-borneol ($C_{10}H_{18}O$, 97%) and (-)-borneol ($C_{10}H_{18}O$, 97%) were purchased from Aldrich. (*R*)-(-)-2-butanol (C_4H_9OH, >99.0%), (*S*)-(+)-2-butanol (C_4H_9OH, >98.0%), Thionyl chloride ($SOCl_2$), 1-ethyl-3-(3-dimethylaminopropyl) carbodiimide hydrochloride (EDC·HCl, $C_8H_{17}N_3$·HCl) were purchased from Tokyo Chemical Industry Co., Ltd. Terbium(III) nitrate hexahydrate ($Tb(NO_3)_3$·$6H_2O$) and triethylamine (Et_3N, $(C_2H_5)_3N$) were purchased from Kanto Chemical Co., Inc.

Apparatus

^{1}H-NMR spectra were recorded in $CDCl_3$ on an auto-NMR JEOL ECS 400 MHz spectrometer; $CHCl_3$ (δ_H = 7.26 ppm) was used as an internal reference. Fast atom bombardment mass spectrometry (FAB-MS) was performed using a JEOL JMS-700TZ spectrometer. Elemental analyses were performed using a MICRO CORDER JM10 system. Infrared (IR) spectra were recorded on a JASCO FT/IR-350 spectrometer. Photoluminescence (PL) spectra were measured using a Horiba FluoroLog®3 spectrofluorometer (excitation wavelength = 380 nm). Luminescence quantum yields were measured using an FP-6300 spectrofluorometer with an integration sphere. The luminescence lifetimes were measured using the third harmonic (355 nm) of a Qswitched Nd:YAG laser. The electronic absorption, CD, and CPL spectra were measured using a JASCO V-670 spectrophotometer, Jasco J-720 (or J-1500) spectropolarimeter, and

Jasco CPL-200 spectrofluoropolarimeter (excitation wavelength = 380 nm), respectively. The quantitative elemental analyses were performed using an inductively coupled plasma-atomic emission spectrometer (ICP-AES, ICPE-9000) to determine the concentration of the Tb(III) ion in PMMA films for the Faraday rotation measurements. The Faraday effect measurements were performed using a JASCO, Model K-250 spectrophotometer.

Synthesis of (+/-)-bornyl salicylate (Sal-(+/-)-Bor)

A solution of salicylic acid (1.0 g, 7.2 mmol) and (+/-)-borneol (1.12 g, 7.2 mmol) in 30 mL of dioxane were refluxed with thionyl chloride (0.82 g, 6.9 mmol) for 1 h at 100°C. The mixture was extracted with $NaHCO_3$ aq. (2 × 20 mL) and ethyl acetate (2 × 20 mL). The organic layer was separated and dried with magnesium sulfate, and the solvent was evaporated. The residue was chromatographed on silica gel eluting with ethyl acetate/hexane (10/90).

[Sal-(+)-Bor]. Yield: 0.29 g (17 %). ^{1}H-NMR (400 MHz, $CDCl_3$): δ/ppm = 10.9 (s, 1H, -OH), 7.87-7.89 (d, 1H, Ar),   7.44-7.48 (t, 1H, Ar), 6.97-6.99 (d, 1H, Ar), 6.88-6.92 (t, 1H, Ar), 5.10-5.14 (m, 1H, -CH), 2.07-2.51 (m, 2H), 1.75-1.77 (m, 1H), 1.12-1.47 (m, 4H), 0.97 (s, 3H, $-CH_3$), 0.92 (s, 6H, $-CH_3$).

[Sal-(-)-Bor]. Yield: 0.63 g (32 %). ^{1}H-NMR (400 MHz, $CDCl_3$) : δ/ppm = 10.9 (s, 1H, -OH), 7.87-7.89 (d, 1H, Ar), 7.44-7.48 (t, 1H, Ar), 6.97-6.99 (d, 1H, Ar), 6.88-6.92 (t, 1H, Ar), 5.10-5.14 (m, 1H, -CH), 2.07-2.51 (m, 2H), 1.75-1.77 (m, 1H), 1.12-1.47 (m, 4H), 0.97 (s, 3H, $-CH_3$), 0.92 (s, 6H, $-CH_3$).
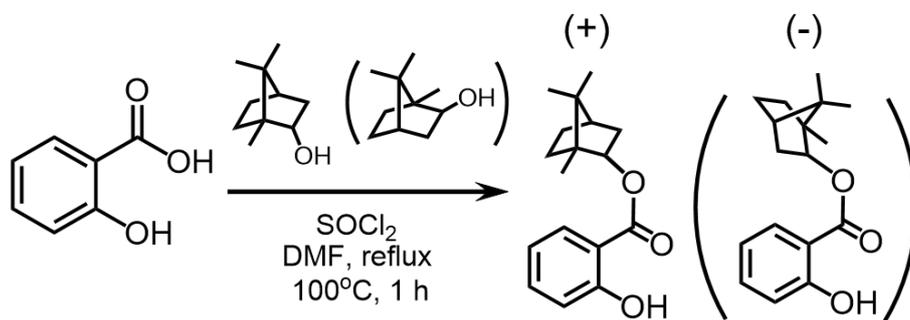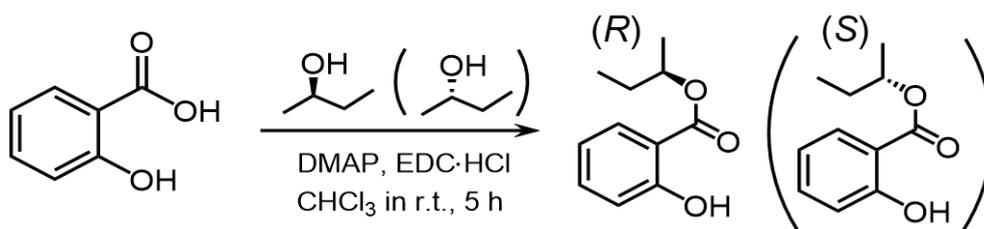
Scheme 2-1. Synthesis of (+/-)-bornyl salicylate.

Synthesis of (*R/S*)-2-Butyl Salicylate (Sal-(*R/S*)-Bt)

Salicylic acid (2.0 g, 14.5 mmol), (*R/S*)-(-/+)-2-butanol (1.08 g, 14.5 mmol), EDC·HCl (2.78 g, 14.5 mmol) and DMAP (0.177 g, 1.45 mmol) were added to CHCl$_3$ (40 mL). The mixture was stirred at room temperature for 5 h under Ar, washed with HCl aq. (2 × 30 mL), NaHCO$_3$ aq. (2 × 30 mL), and distilled H$_2$O (2 × 30 mL). The organic layer was separated and dried with MgSO$_4$, and the solvent was evaporated. The residue was chromatographed on silica gel eluting with ethyl acetate/hexane (10/90).

[Sal-(*R*)-Bt]. Yield: 10.0%. ^{1}H-NMR (400 MHz, CDCl$_3$): δ/ppm = 10.9 (s, 1H, -OH), 7.85 (d, 1H, *J* = 8 Hz, Ar), 7.45 (t, 1H, *J* = 8 Hz, Ar), 6.97 (d, 1H, *J* = 8 Hz, Ar), 6.88 (t, 1H, *J* = 8 Hz, Ar), 5.08-5.18 (m, 1H, -^{2}CH), 1.64-1.84 (m, 2H, -^{3}CH$_2$), 1.36 (d, 3H, *J* = 6 Hz, -^{1}CH$_3$), 0.98 (t, 3H, *J* = 8 Hz, -^{4}CH$_3$). Elemental analysis: Calculated for C$_{11}$H$_{14}$O$_3$: C, 68.02%, H, 7.27%. Found: C, 68.13%, H, 7.52%.

[Sal-(*S*)-Bt]. Yield: 9.7%. ^{1}H-NMR (400 MHz, CDCl$_3$): δ/ppm = 10.9 (s, 1H, -OH), 7.85 (d, 1H, *J* = 8 Hz, Ar), 7.45 (t, 1H, *J* = 8 Hz, Ar), 6.97 (d, 1H, *J* = 8 Hz, Ar), 6.88 (t, 1H, *J* = 8 Hz, Ar), 5.08-5.18 (m, 1H, -^{2}CH), 1.64-1.84 (m, 2H, -^{3}CH$_2$), 1.36 (d, 3H, *J* = 6 Hz, -^{1}CH$_3$), 0.98 (t, 3H, *J* = 8 Hz, -^{4}CH$_3$). Elemental analysis: Calculated for C$_{11}$H$_{14}$O$_3$: C, 68.02%, H, 7.27%. Found: C, 68.15%, H, 7.49%.

Scheme 2-2. Synthesis of (*R/S*)-2-butyl Salicylate.

Synthesis of [Tb₉(sal-(+/-)-Bor)₁₆(*μ*-OH)₁₀]⁺[NO₃]⁻ (Tb-(+/-)-Bor)

(+/-)-bornyl salicylate (0.10 g, 0.36 mmol) was dissolved in methanol, and triethylamine (0.036 g, 0.36 mmol) was added to this solution with stirring at 40°C. Then Tb(NO₃)₃·6H₂O (0.095 g, 0.21 mmol) in methanol was added dropwise to this solution with further stirring for 20 min. White powder, Tb-(+/-)-bor, was obtained.

[Tb-(+)-Bor]. Yield: 0.079 g (56 %). FAB-MS: *m/z* calculated for $C_{272}H_{346}O_{58}Tb_{9}$: [M-NO₃]⁺, 5973.75; Found, 5973.54.

[Tb-(-)-Bor]. Yield: 0.11 g (76 %). FAB-MS: *m/z* calculated for $C_{272}H_{346}O_{58}Tb_{9}$: [M-NO₃]⁺, 5973.75; Found, 5973.88.

L1: Sal-(+)-Bor   L2: Sal-(-)-Bor

L3: Sal-(*R*)-Bt   L4: Sal-(*S*)-Bt

L = L1, L2, L3, L4
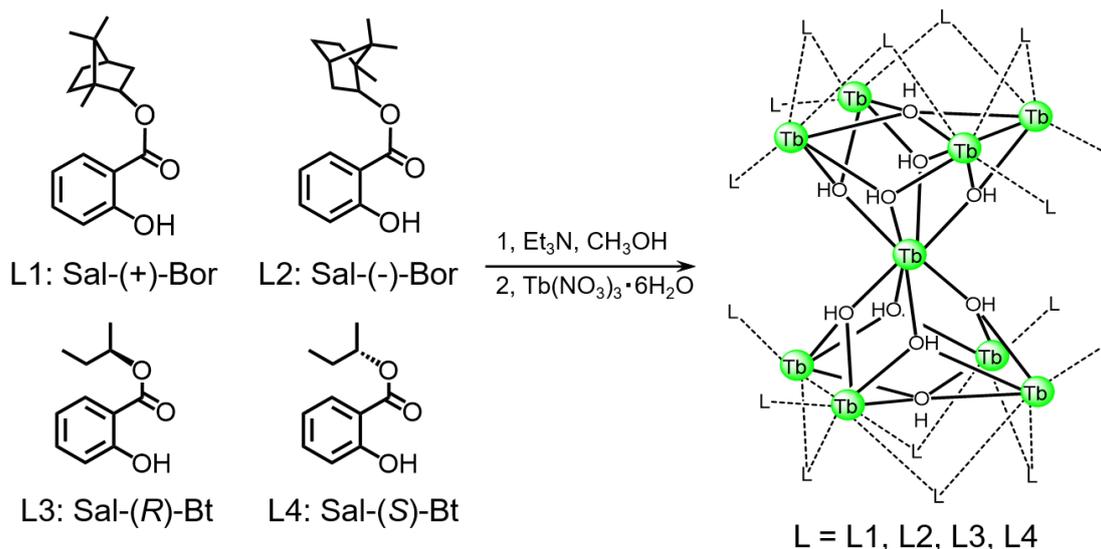
Scheme 2-3. Synthesis of [Tb₉(sal-(+/-)-Bor)₁₆(*μ*-OH)₁₀]⁺[NO₃]⁻ and [Tb₉(sal-(*R/S*)-Bt)₁₆(*μ*-OH)₁₀]⁺[NO₃]⁻.

94

Synthesis of [Tb$_9$(sal-(*R/S*)-Bt)$_{16}$(*µ*-OH)$_{10}$]$^+$[NO$_3$]$^-$ ([Tb-(*R/S*)-Bt])

(*R/S*)-2-butyl salicylate (0.20 g, 1.0 mmol) was dissolved in CH$_3$OH, and Et$_3$N (0.174 g, 1.72 mmol) was added to this solution with stirring at 40ºC. Tb(NO$_3$)$_3$·6H$_2$O (0.26 g, 0.58 mmol) in CH$_3$OH was added dropwise to this solution with further stirring for 20 min. A white powder, Tb-(*R/S*)-Bt, was obtained.

[Tb-(*R*)-Bt]. Selected IR (KBr, cm^{-1}): 1680 (-C=O), 2930 (-CH$_3$-), 2960 (-CH$_3$). Elemental analysis: Calculated for C$_{176}$H$_{218}$NO$_{61}$Tb$_9$: C, 44.47%, H, 4.62%, N, 0.29%. Found: C, 44.12%, H, 4.55%, N, <0.30%. FAB-MS: m/z Calculated for C$_{176}$H$_{218}$O$_{58}$Tb$_9$: [M-NO$_3$]$^+$, 4691.75; Found, 4691.79.

[Tb-(*S*)-Bt]. Selected IR (KBr, cm^{-1}): 1680 (-C=O), 2930 (-CH$_3$-), 2960 (-CH$_3$). Elemental analysis: Calculated for C$_{176}$H$_{218}$NO$_{61}$Tb$_9$: C, 44.47%, H, 4.62%, N, 0.29%. Found: C, 44.50%, H, 4.78%, N, 0.31%. FAB-MS: m/z Calculated for C$_{176}$H$_{218}$O$_{58}$Tb$_9$: [M-NO$_3$]$^+$, 4691.75; Found, 4691.76.

Computational details

Density function theory (DFT) calculations were carried out with the Gaussian R09W B.01 employing the three-parameter hybrid functional of Becke based on the correlation functional of Lee, Yang, and Parr (B3LYP).[9] The 6-31G(d) basis set was used for all atoms.

Spectral measurements

The electronic absorption and CD spectra of Tb-(+/-)-Bor (2.0 × 10^{-5} M) and Tb-(*R/S*)-Bt (2.0 × 10^{-5} M) were measured in DMF and CH$_3$OH, respectively. The PL, CPL spectra of Tb-(+/-)-Bor (1.0 × 10^{-4} M) and Tb-(*R/S*)-Bt (1.0 × 10^{-4} M) were measured in

DMF and CH$_3$OH, respectively. The luminescence quantum yields, and emission lifetimes of Tb-(R/S)-Bt (1.0 × 10^{-4} M) were measured in CHCl$_3$.

Faraday rotation measurements

The Tb(III) clusters Tb-(R/S)-Bt (95 mg) were added to CHCl$_3$ (1 mL). Then, the solution (0.2 mL) was added to PMMA (2.8 g) dissolved in CHCl$_3$ (10 mL). PMMA films were prepared on glass substrates using a casting method. The thickness of the PMMA film was approximately 1.2 mm, and the transmittance was >90% in the 400-800 nm region. The external magnetic field was 15 kOe.

4.3　Results and discussion

4.3.1　Electronic states and optical activities of the Tb(III) clusters

The Tb(III) clusters Tb-(+)-Bor, Tb-(-)-Bor, Tb-(R)-Bt and Tb-(S)-Bt were composed of nine Tb(III) ions bridged by ten μ-OHs and sixteen chiral salicylate ligands, which was confirmed by FAB-MS. These structures of Tb-(R)-Bt and Tb-(S)-Bt were also identified by IR spectroscopy, and elemental analysis. Previously, Nakanishi reported the X-ray single crystal structures of Tb(III) clusters with kinds of alkyl salicylates.[5] The structures of the Tb(III) clusters were dominated by their alkyl salicylate ligands with intramolecular CH-π and π-π interactions. The synthesized Tb(III) clusters, Tb-(+/-)-Bor and Tb-(R/S)-Bt, should form nonanuclear structures depending on the ester groups.

The UV-vis absorption spectra of Sal-(+)-Bor, Tb-(+)-Bor, Sal-(R)-Bt, and Tb-(R)-Bt are shown in **Figures 4-3a** and **4-4a**. Intense absorption bands were observed in both Tb-(+)-Bor and Tb-(R)-Bt at approximately 350 and 340 nm ($\varepsilon_{max} \approx 60,000$ cm^{-1} M^{-1}), respectively, due to the π-π* transition of the coordinating sixteen salicylate ligands (**Figures 4-3a** and **4-4a**, red). The spectrum of the Tb (III) clusters was red-shifted and broadened compared to that of the ligands (**Figures 4-3a** and **4-4a**, black). The 4f-4f transition of the Tb(III) ions (expected at 488 nm) was not observed because this transition is essentially forbidden by the Laporte rule ($\varepsilon_{max} < 1$ cm^{-1} M^{-1}).[10]

To clarify the π-electronic properties of the ligands and Tb(III) clusters, the energy level and oscillator strength of S_1 were calculated for Sal-(+)-Bor using the TD-DFT (B3LYP/6-31G(d)) method (**Figure 4-5a**). For the Tb(III) clusters, the simplified complex model, Li-(+)-Bor, was carried out (**Figure 4-5b**). The oscillator strengths of Sal-(+)-Bor and Li-(+)-Bor were calculated to be 0.116 ($\lambda = 291.5$ nm) and 0.145 ($\lambda = 334.5$ nm), respectively. These transitions are mainly dominant to HOMO → LUMO
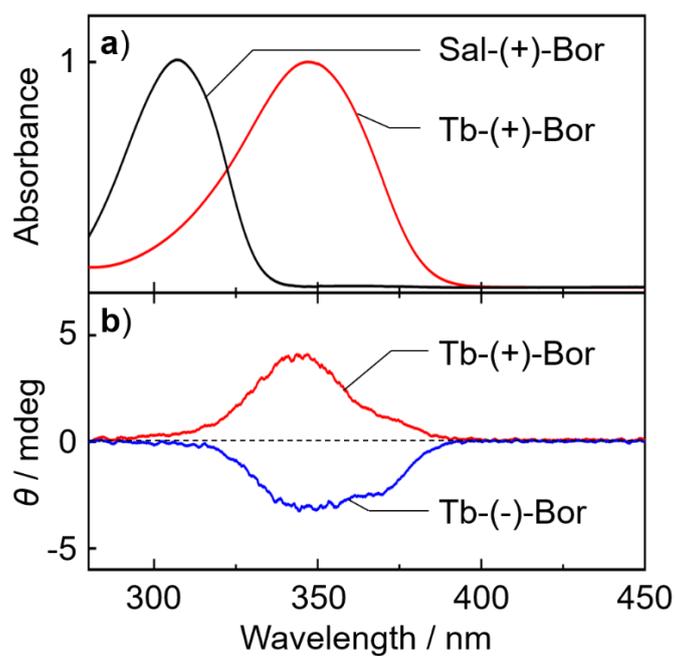
97

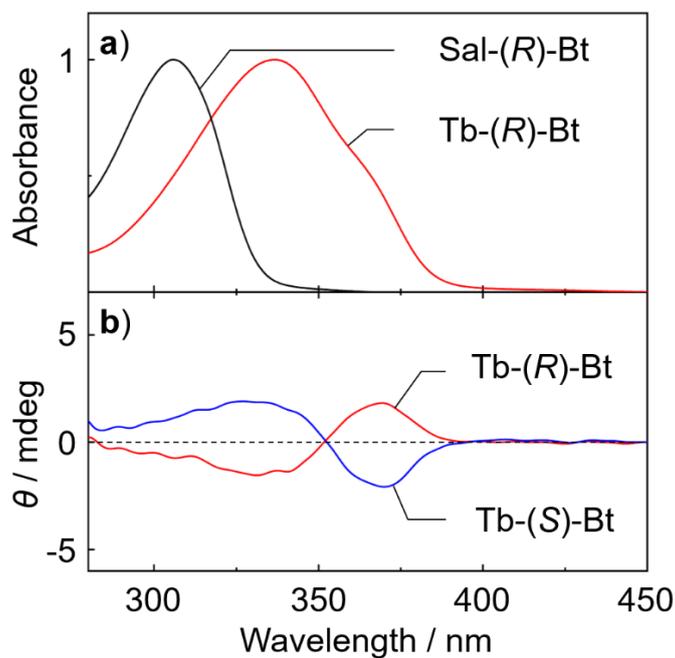**Figure 4-3.** (**a**) Absorption and (**b**) CD spectra of Sal-(+)-Bor (black), Tb-(+)-Bor (red), and Tb-(-)-Bor (blue) in DMF (2.0×10^{-5} M).

Figure 4-4. (**a**) Absorption and (**b**) CD spectra of Sal-(*R*)-Bt (black), Tb-(*R*)-Bt (red), and Tb-(*S*)-Bt (blue) in CH_3OH (2.0×10^{-5} M).
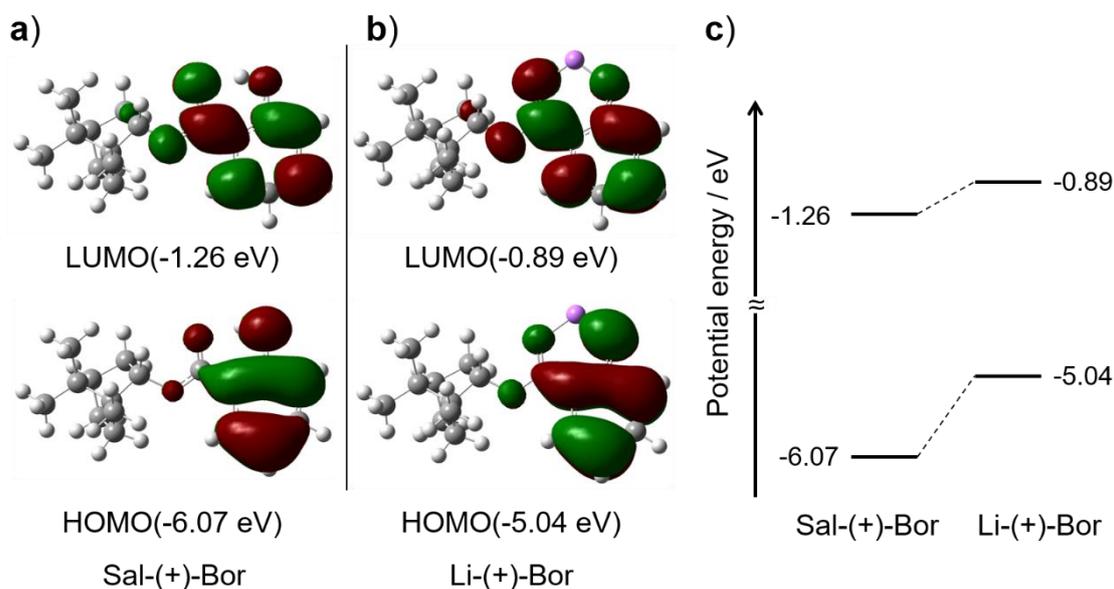
Figure 4-5. (**a**) Molecular orbitals of Sal-(+)-Bor and (**b**) Li-(+)-Bor, and (**c**) their potential energies.

transition (transition probability; TP$_{HOMO \rightarrow LUMO, Sal-(+)-Bor}$ = 94%, TP$_{HOMO \rightarrow LUMO, Li-(+)-Bor}$ = 95%). The energy gap between HOMO and LUMO is directly linked to the absorption wavelength. The energy gaps of Sal-(+)-Bor and Li-(+)-Bor are found to be 4.81 eV and 4.15 eV, respectively (**Figure 4-5c**). The magnitude of the destabilization of HOMO in Li-(+)-bor is larger than that of LUMO. The destabilization of HOMO caused the red-shifted absorption for the Tb(III) clusters.

At the red-shifted intense absorption band, positive (or negative) CD signal was observed for Tb-(+)-Bor (or Tb-(-)-Bor) clusters (**Figure 4-3b**), the signs of which were dependent on the asymmetric centers of the organic ligands. On the other hand, Tb-(*R*)-Bt and Tb-(*S*)-Bt exhibited bisignate CD bands due to the π-π* transitions of the salicylate ligands (**Figure 4-4b**). These bisignate spectra were consistent with the

absorption maximum peak (335 nm) and shoulder peak (365 nm), respectively, which was attributed to an exciton coupling.[6,11–14] These results indicate that intramolecular interactions might occur between neighboring chiral ligands in Tb-(R)-Bt and Tb-(S)-Bt. The broadened band of Tb(III) clusters is not related to CT transition because the Tb(III) ion shows high reduction potential, and its LMCT transition state is located at higher energy (>60,000 cm^{-1}). Because the electronic state of the Tb(III) ion depends on the coordination geometry formed by the ligands,[10] the absence or existence of intramolecular interactions in the Tb(III) clusters affect the photophysical properties based on the transitions of the Tb(III) ions.

　　　To assess the electronic states of Tb-(+/-)-Bor and Tb-(R/S)-Bt, high-resolution PL measurements were carried out. The PL spectra of Tb-(+/-)-Bor and Tb-(R/S)-Bt showed four sharp emission bands in the region of 450-650 nm, which were attributed to the $^5D_4 \rightarrow {^7}F_J$ (J = 6, 5, 4, 3) transitions of the Tb(III) ions (**Figures 4-6** and **4-7**).[10] In contrast to the absorption spectra, emission bands resulting from the π-π* transitions of the ligands were not observed. This effect was attributed to the intersystem crossing of the ligand from the excited singlet state to the excited triplet state promoted by the spin-orbit coupling of the Tb(III) ions. The Stark splitting and the spectral shape of Tb-(+)-Bor were slightly different from those of Tb-(-)-Bor (**Figure 4-6**, inset), indicating that the clusters were not stable in solution. The instability of the clusters may be caused by the weak intramolecular interaction due to the steric hindrance of bornyl group. The single sign of CD spectra supports the weak intramolecular interaction between ligands in Tb-(+/-)-Bor (**Figure 4-3**). In contrast, the splitting of Tb-(R)-Bt was consistent with that of Tb-(S)-Bt (**Figure 4-7**, inset). In time-resolved spectroscopy, the emission decays ($^5D_4 \rightarrow {^7}F_5$ transition) of Tb-(R/S)-Bt were fitted by single exponential curves. The emission
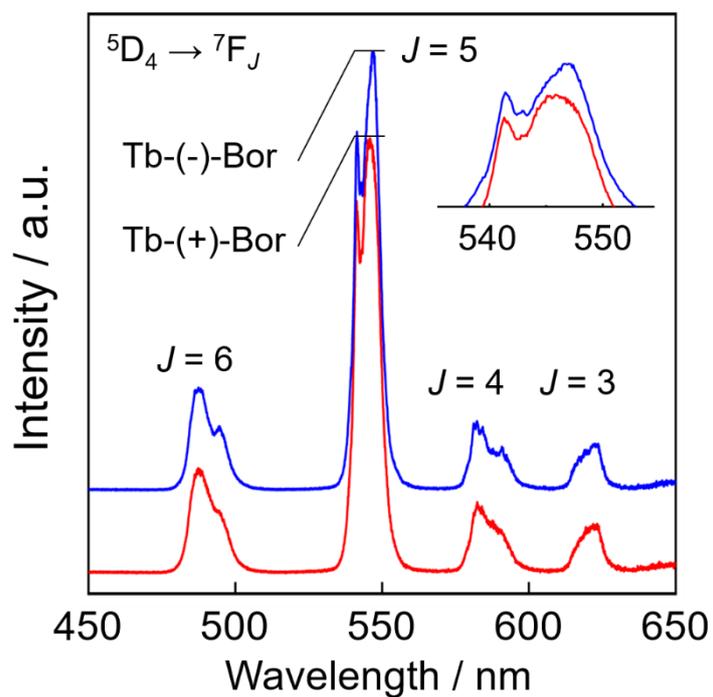
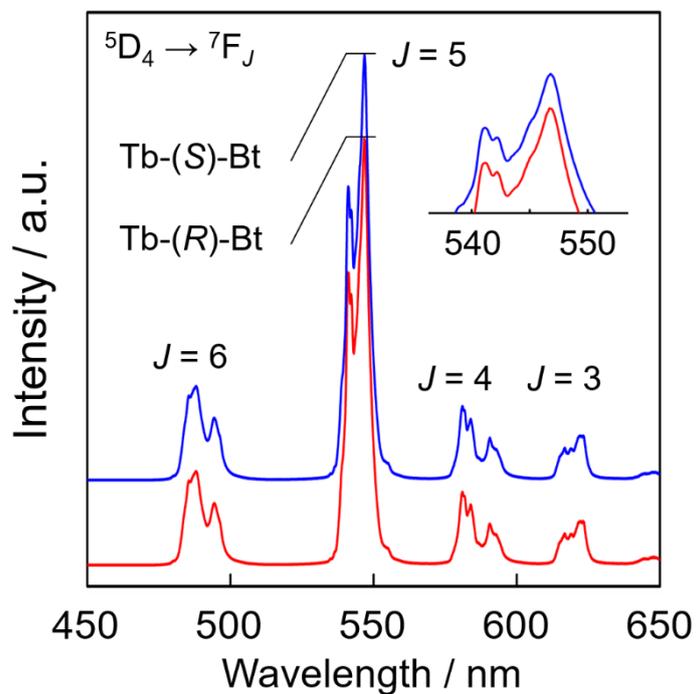**Figure 4-6.** High-resolution PL spectra of Tb-(+)-Bor (red) and Tb-(-)-Bor (blue) in DMF $(1.0 \times 10^{-4}$ M).

Figure 4-7. High-resolution PL spectra of Tb-(R)-Bt (red line) and Tb-(S)-Bt (blue line) in CHCl$_3$ $(1.0 \times 10^{-4}$ M).

lifetime (τ = 1.3 ms) and the emission quantum yields (Φ_{total} = 14%) of Tb-(R)-Bt were the same as τ = 1.3 ms and Φ_{total} = 15% of Tb-(S)-Bt within the experimental error. These results demonstrate that Tb-(R)-Bt and Tb-(S)-Bt form mirror image stereoisomers in solution, and these clusters are thus expected to show identical photophysical properties, with the exception of their chiroptical characteristics.

CPL measurements were also performed for these clusters (**Figures 4-8** and **4-9**), and the observed signals were corresponded to the transitions of the Tb(III) ions. The g_{CPL} values are summarized in **Table 4-1**. The largest g_{CPL} values were observed at the $^5D_4 \rightarrow {}^7F_5$ transitions (g_{CPL} = ±0.02 for Tb-(+/-)-Bor, and g_{CPL} = ±0.04 for Tb-(R/S)-Bt), which were on the same order of magnitude as previously reported for Tb(III) complexes.[8,15,16] The large g_{CPL} consequently leads to a large g_{CD},[17] which is expected to give large transition magnetic dipole moments around the Faraday-active wavelength based on the 4f-4f absorption.

Table 4-1. The dissymmetry factor g_{CPL} of the Tb(III) clusters.

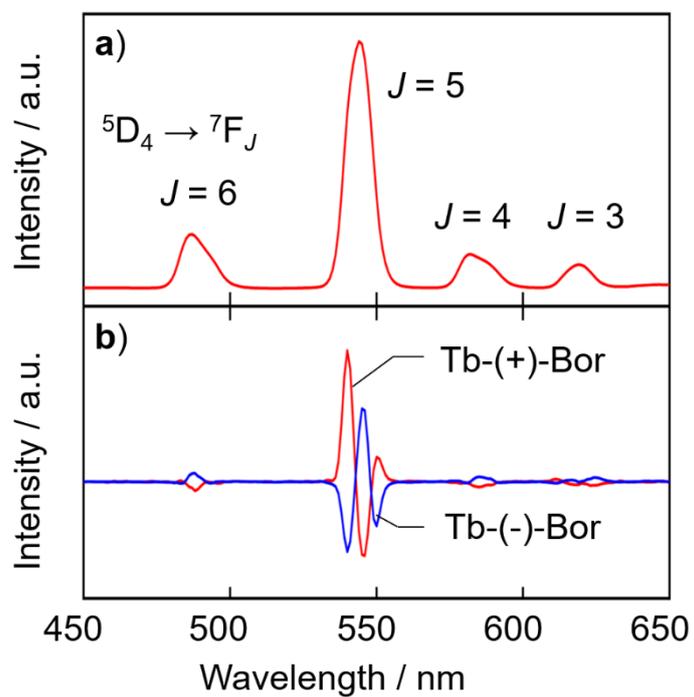| Complex	g_{CPL}			
	$^5D_4 \rightarrow {}^7F_6$	$^5D_4 \rightarrow {}^7F_5$	$^5D_4 \rightarrow {}^7F_4$	$^5D_4 \rightarrow {}^7F_3$
Tb-(+)-Bor	-0.006	+0.02	-0.006	-0.02
Tb-(-)-Bor	+0.005	-0.02	+0.005	+0.02
Tb-(R)-Bt	+0.008	+0.04	+0.005	-0.02
Tb-(S)-Bt	-0.01	-0.04	-0.004	+0.03

Figure 4-8. (**a**) PL and (**b**) CPL spectra of Tb-(+)-Bor (red) and Tb-(-)-Bor (blue) in DMF (1.0×10^{-4} M).
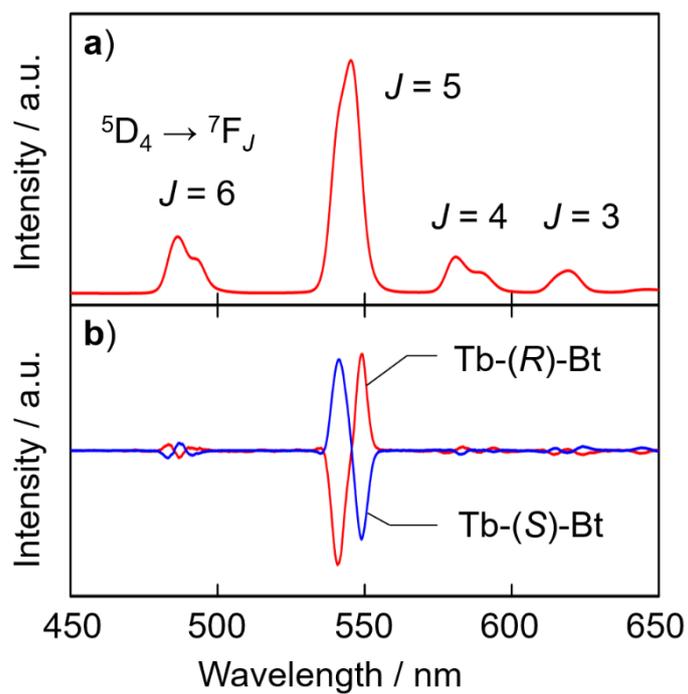

Figure 4-9. (**a**) PL and (**b**) CPL spectra of Tb-(*R*)-Bt (red) and Tb-(*S*)-Bt (blue) in CHCl$_3$ (1.0×10^{-4} M).

4.3.2 The Faraday effect of the chiral Tb(III) clusters

In the high-resolution PL and CPL measurements, the magnitude of optical activities for Tb-(*R/S*)-Bt clusters was the same as Tb-(+/-)-Bor, while the stability of Tb-(*R/S*)-Bt was higher than that of Tb-(+/-)-Bor. Hence, the Faraday effect of Tb-(*R/S*)-Bt was investigated to clarify the relationship between magneto-optical activities and molecular chirality.

The wavelength dependence of the Faraday rotation was measured using PMMA films containing Tb-(*R*)-Bt or Tb-(*S*)-Bt. The Faraday rotation was determined based on the Verdet constant, *V*, as defined in Equation (4.1),[7]

$$V = \frac{\theta}{Hl}. \tag{4.1}$$

Here, *θ*, *H*, and *l* represent the Faraday rotation angle, the external magnetic field, and the thickness of the film, respectively. In these experimental trials, the concentration *C* of the Tb(III) ions in the film was determined using ICP-AES. Based on previous work,[5] the Verdet constant, *Vc*, normalized by the concentration of Tb(III) ions in the film was subsequently calculated as Equation (4.2),

$$V_C = \frac{\theta}{HlC}. \tag{4.2}$$

The measured rotation angle consists of a magnetic rotation, θ_F, due to the Faraday effect and a natural rotation, θ_{CD}, due to chirality. To extract θ_{CD} from the total rotational angle, two rotational angles, θ_+ and θ_-, were measured by applying an external magnetic field parallel (+) and antiparallel (-) to the direction of light propagation, respectively (**Figure 4-10**). These parameters are represented as Equations (4.3a) and (4.3b),
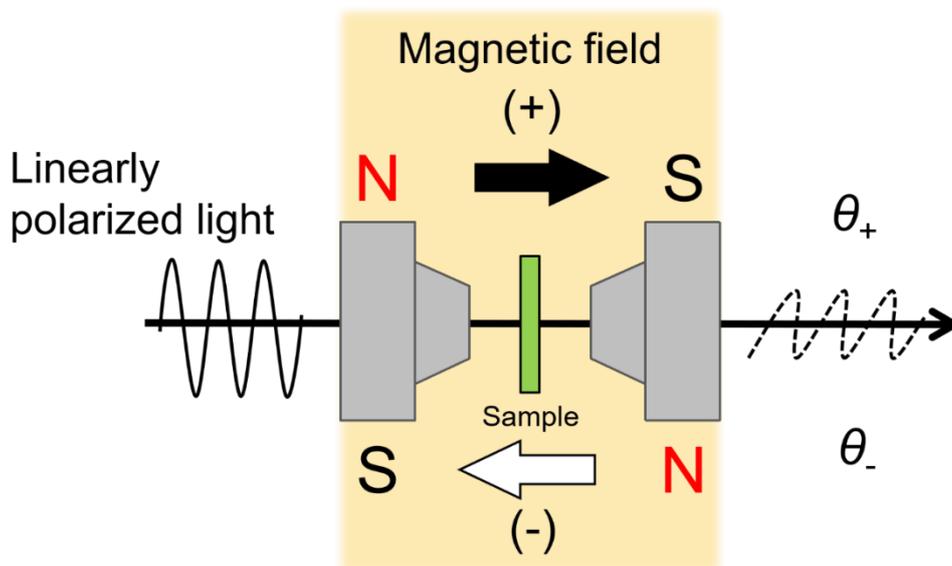
$$\theta_+ = \theta_F + \theta_{CD}, \tag{4.3a}$$

Figure 4-10. The Faraday effect measurement applying an external magnetic field parallel (+) and antiparallel (-) to the direction of light propagation. The obtained rotation angles are described as θ_+ and θ_-, respectively.

$$\theta_- = -\theta_F + \theta_{CD} . \qquad (4.3b)$$

The Faraday rotation angle was obtained from Equations (4.3a) and (4.3b),

$$\theta = \theta_F = \frac{1}{2}(\theta_+ - \theta_-) . \qquad (4.4)$$

The Faraday rotation spectra of the Tb-(R/S)-Bt are shown in **Figure 4-11a**. The difference spectrum, ΔV_C, obtained by subtracting the spectrum of Tb-(R)-Bt to that of Tb-(S)-Bt is shown in **Figure 4-11b**. In **Figure 4-11a**, negative Faraday rotation angles are observed at approximately 450 nm. The Verdet constant of the Tb-(R)-Bt ($V_{C,max(446 \text{ nm})}$ = -5.2 × 10^{-4} deg Oe^{-1} cm^{-1} M^{-1}) was larger than that of the Tb-(S)-Bt ($V_{C,max(446 \text{ nm})}$ = -3.4 × 10^{-4} deg Oe^{-1} cm^{-1} M^{-1}). This result represents the first observation of a Faraday effect that is dependent on the chirality of the clusters.

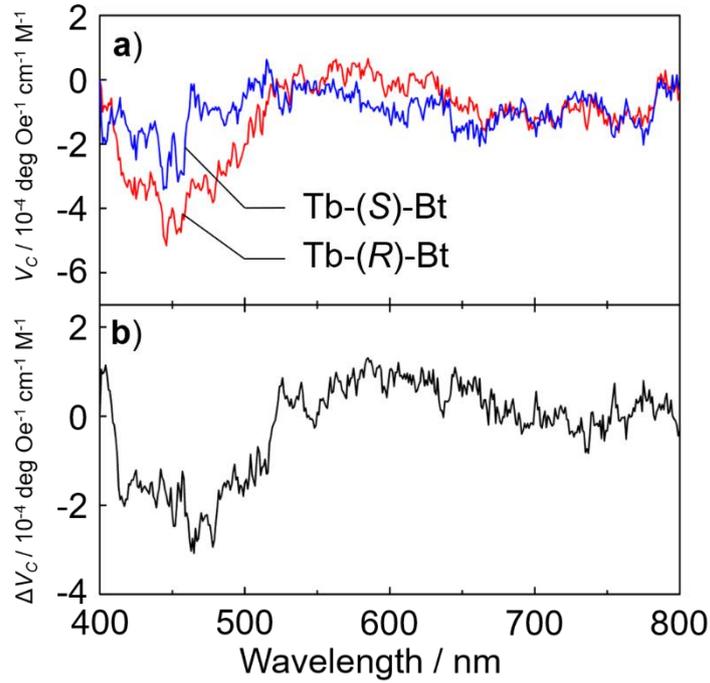**Figure 4-11.** (**a**) The Faraday rotation spectra of Tb-(*R*)-Bt (red) and Tb-(*S*)-Bt (blue), and (**b**) the differential spectrum between Tb-(*R*)-Bt and Tb-(*S*)-Bt in PMMA films.

The Faraday rotation angle can be expressed by using the sum of three terms resulting from three electronic conditions in Equation (1.10) in chapter 1,[7,18,19]

$$\theta_F \propto f_1 A + f_2 \left(B + \frac{C}{k_B T} \right). \tag{1.9}$$

Here, f_1 and f_2 are functions that provide explicit descriptions of the shape of the Faraday effect. The Faraday A and C terms primarily reflect the degeneracy of the excited and the ground states, respectively, whereas the Faraday B term is related to the mixing of the ground and two or more excited states by the magnetic field. The wavelengths observed in the Faraday effect measurements are associated with several 4f-4f transitions such as $^7F_6 \rightarrow {}^5D_4$ (488 nm), $^7F_6 \rightarrow {}^5D_3$ (380 nm),[20] and the broad 4f-5d (below 300 nm)[21] transitions of the Tb(III) ions and the $S_0 \rightarrow T_1$ transitions (470 nm) of

106

the ligands.[22] The degenerate ground state is not formed by diamagnetic organic molecules such as the ligands, but rather by the paramagnetic Tb(III) ions depending on the total angular momentum, J. In this case, the $^7F_6$ ($J = 6$) state of the Tb(III) ions can degenerate into thirteen states ($2J + 1$). For this reason, the observed signals were primarily due to the transitions of the Tb(III) ions.

The photophysical properties of the Tb(III) ions depend on their coordination geometry. Previously, Nakanishi reported that the Faraday rotation angles of nonanuclear Tb(III) cluster derivatives were changed by altering a substituent in the ligands.[5] This effect results not from changing the electronic state of the ligands, but rather from varying the geometry around the Tb(III) ions of the cluster by using different ester substituents in the ligands.[23] As observed in **Figure 4-7**, the shape of the Stark splitting of Tb-(R)-Bt was consistent with that of Tb-(S)-Bt based on their geometries, suggesting that difference in the Faraday rotation angle is not derived from configuration interactions between the 4f-4f and 4f-5d transitions by their crystal fields. These aspects of the photophysical behavior indicate that the difference between the Faraday rotation angles observed in this experimental work might be attributable to the large transition magnetic dipole moments of Tb-(R)-Bt and Tb-(S)-Bt. The sign of the transition magnetic dipole moments in the Faraday B term inverts depending on the chirality,[7] indicating that this term might be affected by interactions between the 4f-4f ($^7F_6 \rightarrow {}^5D_4$) transition and the other 4f-4f transitions such as $^7F_6 \rightarrow {}^5D_3$ or the 4f-5d transition. The chirality-induced magneto-optical effect observed in this study is a different phenomenon from magneto-chiral dichroism (i.e., the absorption dependence of a chiral molecule on the direction of a magnetic field).[24–26] Although it is difficult to determine the exact origin of the phenomenon at this stage, this is the first report that Faraday rotation is affected by

chiroptical properties. This result could be a key factor in the design of new materials exhibiting the Faraday effect and may also broaden the field of chiral science.

4.4   Conclusions

The chiroptical and magneto-optical properties of novel four types of chiral nonanuclear Tb(III) clusters, which are composed of nine Tb(III) ions and sixteen chiral salicylate ligands, were assessed. The CD signals in the ππ* transition of the Tb(III) clusters were dependent on the coordination structures induced by the ester groups of the salicylate ligands. The chiral Tb(III) clusters exhibited CPL signals corresponding to the 4f-4f transitions, which indicated that the chirality of ligands was reflected to the Tb(III) core in the clusters. Furthermore, the Faraday rotation angle of Tb-(*R*)-Bt was greater than that of Tb-(*S*)-Bt, indicating that the Faraday effect was affected by the chirality of the Tb(III) clusters. These results provide significant new insight regarding the interrelation between chirality and the Faraday effect.
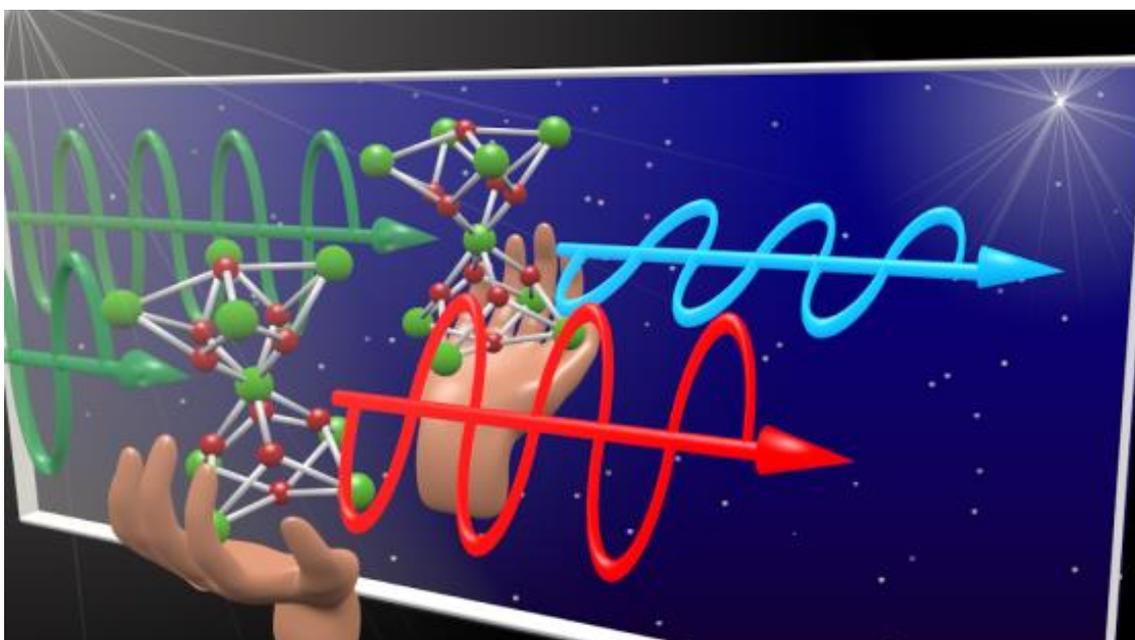
4.5   References

[1]   E. G. Villora, P. Molina, M. Nakamura, K. Shimamura, T. Hatanaka, A. Funaki, K. Naoe, *Appl. Phys. Lett.* **2011**, *99*, 1–4.

[2]   H. Lin, S. Zhou, H. Teng, *Opt. Mater.* **2011**, *33*, 1833–1836.

[3]   W. Li, K. Zou, M. Lu, B. Peng, W. Zhao, *Int. J. Appl. Ceram. Technol.* **2010**, *7*, 369–374.

[4]   H. Yoshida, K. Tsubakimoto, Y. Fujimoto, K. Mikami, H. Fujita, N. Miyanaga, H. Nozawa, H. Yagi, T. Yanagitani, Y. Nagata, H. Kinoshita, *Opt. Express* **2011**, *19*, 15181.

[5]   T. Nakanishi, Y. Suzuki, Y. Doi, T. Seki, H. Koizumi, K. Fushimi, K. Fujita, Y. Hinatsu, H. Ito, K. Tanaka, Y. Hasegawa, *Inorg. Chem.* **2014**, *53*, 7635–41.

[6]   J. A. Schellman, *Acc. Chem. Res.* **1968**, *1*, 144–151.

[7]   P. N. Schatz, A. J. McCaffery, *J. Quart. Rev.* **1969**, *23*, 552–584.

[8]   S. Petoud, G. Muller, E. G. Moore, J. Xu, J. Sokolnicki, J. P. Riehl, U. N. Le, S. M. Cohen, K. N. Raymond, *J. Am. Chem. Soc.* **2007**, *129*, 77–83.

[9]   A. D. Becke, *J. Chem. Phys.* **1993**, *98*, 5648–5652.

[10]   S. V Eliseeva, J.-C. G. Bünzli, *Chem. Soc. Rev.* **2010**, *39*, 189–227.

[11]   G. Bobba, Y. Bretonnière, J.-C. Frias, D. Parker, *Org. Biomol. Chem.* **2003**, *1*, 1870–1872.

[12]   R. S. Dickins, J. A. K. Howard, J. M. Moloney, D. Parker, R. D. Peacock, G. Siligardi, *Chem. Commun.* **1997**, 1747–1748.

[13]   O. Kotova, S. Blasco, B. Twamley, J. O'Brien, R. D. Peacock, J. A. Kitchen, M. Martínez-Calvo, T. Gunnlaugsson, *Chem. Sci.* **2015**, *6*, 457–471.

[14]   R. S. Dickens, J. a. K. Howard, C. L. Maupin, J. M. Moloney, D. Parker, R. D.

Peacock, J. P. Riehl, G. Siligardi, *New J. Chem.* **1998**, *22*, 891–899.

[15] J. Yuasa, T. Ohno, K. Miyata, H. Tsumatori, Y. Hasegawa, T. Kawai, *J. Am. Chem. Soc.* **2011**, *133*, 9892–9902.

[16] M. Seitz, E. G. Moore, A. J. Ingram, G. Muller, K. N. Raymond, *J. Am. Chem. Soc.* **2007**, *129*, 15468–15470.

[17] F. Richardson, *Inorg. Chem.* **1980**, *19*, 2806–2812.

[18] C. Djerassi, C. Djerassi, E. Bunnenberg, E. Bunnenberg, D. L. Elder, D. L. Elder, *Pure Appl. Chem.* **1971**, *25*, 57–90.

[19] A. J. McCaffery, *Nat. Phys. Sci.* **1971**, *232*, 137–140.

[20] W. T. Carnall, J. P. Hessler, F. W. Wagner, *J. Phys. Chem.* **1978**, *82*, 2152–2158.

[21] K. Miyamoto, K. Isai, M. Suwa, H. Watarai, *J. Am. Chem. Soc.* **2009**, *131*, 6328–6329.

[22] S. Omagari, T. Nakanishi, T. Seki, Y. Kitagawa, Y. Takahata, K. Fushimi, H. Ito, Y. Hasegawa, *J. Phys. Chem. A* **2015**, *119*, 1943–1947.

[23] L. V. Fluyt, *J. Alloys Compd.* **1994**, *208*, 51–54.

[24] Y. Kitagawa, H. Segawa, K. Ishii, *Angew. Chem. Int. Ed.* **2011**, *50*, 9133–9136.

[25] G. L. J. A. Rikken, E. Raupach, **1997**, *390*, 493–494.

[26] G. L. Rikken, E. Raupach, *Nature* **2000**, *405*, 932–935.

Chapter 5

Summary

5.1   Summary and outlook

The photophysical properties of chiral Ln(III) complexes are affected by the surrounding environment around Ln(III) ions. The purpose of this study is to develop chiral Ln(III) complexes for applying to CPL materials and to clarify the chirality of Ln(III) complex from the viewpoint of electronic state mixing under surrounding environment. The photophysical properties related to optical- and magneto-optical activities of chiral Ln(III) complexes depending on the surrounding environment are described in the section.

In Chapter 1, photophysical properties and polarized light response of Ln(III) complexes depending on the electronic state induced by surrounding environment were introduced. The theoretical background of optical- and magneto-optical activities were also described.

In Chapter 2, the non-crystalline Eu(III) complex was obtained by co-grinding of Eu(III) complex with chiral camphor derivative ligands, +tfc, and achiral phosphine oxide, tdmpo, molecules. The weak interaction between the Eu(III) complex and tdmpo molecules suppressed the crystallinity and the large g_{CPL} with large emission intensity were achieved in film state. The result indicated the photophysical and CPL properties of camphor Eu(III) complex can be controlled by external achiral ligands. The CPL intensity was easily detected to the naked eye with simple setup of CPL determination in film state. The author demonstrated the possibility of the chiral Eu(III) complex for CPL security ink.

In Chapter 3, CPL properties of the Eu(III) complex with +tfc and triphenylphosphine oxide (tppo) ligands in various conditions were investigated to demonstrate the optical activity based on the chiral electronic structure. The g_{CPL} values

of the chiral Eu(III) complex were drastically changed depending on the surrounding achiral molecules. The CPL signal inversion was observed for the Eu(III) complex with the same chiral coordination structure-type (Λ or Δ) from the spectroscopic viewpoint. The CPL phenomena was attributed to the chiral electronic structure related to the transition electric dipole moment ($\vec{\mu}$), where the large $|\vec{\mu}|$ value by electronic state J-mixing lead to the large g_{CPL} value and the signal inversion.

In Chapter 4, four types of novel Tb(III) clusters with chiral salicylate ligands were synthesized to clarify the relationship between magneto-optical activity and molecular chirality. CPL of the Tb(III) clusters were observed in the 4f-4f transition, which indicated that the chirality of ligands was reflected to the Tb(III) core in the cluster. For the Tb(III) clusters with chiral butyl salicylate ligands, the Faraday rotation angles were dependent on the chirality of the Tb(III) clusters. The author demonstrated that the molecular chirality of Tb(III) cluster affected the magneto-optical activity by electronic state mixing under external magnetic field.

Optical activities of chiral compounds potentially include numerous information on the light. Ln(III) complexes under chiral environment are hopeful candidate for next generation photo-functional materials with polarized light response that cannot be achieved by chiral organic molecules or other metal complexes. In this study, the chirality of Ln(III) complex was clarified from the viewpoint of the electronic state depending on the external field. The results lead to the possibility of generating novel CPL materials and new magneto-optical phenomenon of chiral Ln(III) complex controlled by external environment. The author hopes that chiral Ln(III) complex optimized by external environment will open up a new field of chiral science and develop next generation photo-functional materials with polarized light response.

List of publications

[1]   Satoshi Wada, Yuichi Kitagawa, Takayuki Nakanishi, Koji Fushimi, Yasuchika Hasegawa, **Chiroptical Properties of Nonanuclear Tb(III) Clusters with Chiral Champhor Derivative Ligands**, *e-Journal of Surface Science and Nanotechnology*, **2015**, *13*, 31-34.

[2]   Satoshi Wada, Yuichi Kitagawa, Takayuki Nakanishi, Koji Fushimi, Yasuhiro Morisaki, Koji Fujita, Katsuaki Konishi, Katsuhisa Tanaka, Yoshiki Chujo, Yasuchika Hasegawa, **The relationship between magneto-optical properties and molecular chirality**, *NPG Asia Materials*, **2016**, *8*, e251.

[3]   Satoshi Wada, Yuichi Kitagawa, Takayuki Nakanishi, Masayuki Gon, Kazuo Tanaka, Koji Fushimi, Yoshiki Chujo, Yasuchika Hasegawa, **Electronic chirality inversion of lanthanide complex induced by achiral molecules**, *Scientific Reports*, **2018**, *8*, 16395-16402.

Other publications

[1]   Mari Miyano, Satoshi Wada, Takayuki Nakanishi, Yasuchika Hasegawa, **Luminescent silicon nanoparticles covered with ionic liquid**, *Materials Letters*, **2015**, *141*, 359-361.

[2]   Mari Miyano, Takayuki Nakanishi, <u>Satoshi Wada</u>, Yuichi Kitagawa, Akira Kawashima, Koji Fushimi, Yasuchika Hasegawa, **Luminescent silicon nanoparticles surface-modified with chiral molecules**, *Journal of Photopolymer Science and Technology*, **2015**, *28*, 225-260.

[3]   Mari Miyano, Yuichi Kitagawa, <u>Satoshi Wada</u>, Akira Kawashima, Ayako Nakajima, Takayuki Nakanishi, Junya Ishioka, Tamaki Shibayama, Seiichi Watanabe, Yasuchika Hasegawa, **Photophysical properties of luminescent silicon nanoparticles surface-modified with organic molecules via hydrosilylation**, *Photochemical and Photobiological Sciences*, **2015**, *15*, 99-104.

[4]   Yuichi Kitagawa, <u>Satoshi Wada</u>, Kei Yanagisawa, Takayuki Nakanishi, Koji Fushimi, Yasuchika Hasegawa, **Molecular design guidelines for large magnetic circular dichroism intensities in lanthanide complexes**, *ChemPhysChem*, **2016**, *17*, 845-849.

[5]   Yasuchika Hasegawa, Yui Miura, Yuichi Kitagawa, Satoshi Wada, Takayuki Nakanishi, Koji Fushimi, Tomohiro Seki, Hajime Ito, Takeshi Iwasa, Tetsuya Taketsugu, Masayuki Gon, Kazuo Tanaka, Yoshiki Chujo, Shingo Hattori, Masanobu Karasawa, Kazuyuki Ishii, **Spiral Eu(III) coordination polymers with circularly polarized luminescence**, *Chemical Communications*, **2018**, *54*, 10695-10697.

Awards

[1]   Best presentation award, The First International Workshop in a Hokkaido Branch of Japan Society of Coordination Chemistry, "Magneto-optical properties of nonanuclear Tb(III) cluster with chiral ligands" July 2014

[2]   優秀ポスター発表賞、第 26 回配位化合物の光化学討論会、「キラル配位子を導入した九核 Tb(III)クラスターの光物性とファラデー効果特性」2014 年 8 月

[3]   優秀ポスター賞、2014 年光化学討論会、「キラル配位子を導入した九核 Tb(III)クラスターの CPL とファラデー回転特性」2014 年 10 月

[4]   Poster Award, 15th Chitose International Forum on Photonics Science & Technology, "Synthesis of nonanuclear Tb(III) clusters with chiral ligands" October 2014

[5]   優秀ポスター賞、第 4 回 CSJ 化学フェスタ 2014、「キラル配位子を導入した九核 Tb(III)クラスターのファラデー回転特性」2014 年 10 月

[6]   優秀講演賞、日本化学会北海道支部、「希土類クラスターのキラリティーに依存したファラデー回転特性」2015 年 7 月

[7]   学生講演賞、錯体化学会第 65 回討論会、「The relationship between magneto-optical properties and molecular chirality of lanthanide clusters」2015 年 9 月

[8]　　　優秀ポスター賞、第 5 回 CSJ 化学フェスタ 2015、「キラリティーに依存した

希土類クラスターのファラデー回転特性」2015 年 10 月

Acknowledgements

Finally, I am particularly grateful to my family Kazuhiko Wada, Mutsumi Wada, and Hiroki Wada for their continuous support and understanding.

March 2019

Satoshi Wada